JETP Letters, Vol. 71, No. 10, 2000, pp. 395–398. From Pis'ma v Zhurnal Éksperimental'noĭ i Teoreticheskoĭ Fiziki, Vol. 71, No. 10, 2000, pp. 577–582.

GRAVITY, ASTROPHYSICS

Supersonic Waves of Magnetization in Dark Interstellar Molecular Clouds[1]

J. Yang*, ** and S. I. Bastrukov*, **, ***

** Asia Pacific Center for Theoretical Physics, Seoul 130-012, Korea*

*** Center for High Energy Astrophysics and Isotope Studies and Department of Physics, Ewha Womans University, Seoul 120-750, Korea*

**** Joint Institute for Nuclear Research, Dubna, Moscow region, 141980 Russia*

Received March 20, 2000; in final form, April 14, 2000

We suggest that supersonic linewidths inferred from recent measurements of magnetic fields toward the core position in dark interstellar molecular clouds may be due to transverse waves of magnetization propagating in a poorly ionized, magnetically ordered gas–dust medium composed of tiny ferromagnetic dusty grains suspended in a cold gaseous cloud of molecular hydrogen. © *2000 MAIK "Nauka/Interperiodica".*

PACS numbers: 98.38.Dq

The physical nature of supersonic OH linewidths detected in recent Zeeman measurements from dark molecular clouds [1–3] is the objective of intense current debate [4–7] (see also references therein), primarily around the seminal suggestion of Arons and Max [8] to identify the supersonic velocity dispersion with the speed of transverse Alfvénic waves in gas–dust interstellar mediums (ISM). While the assumptions underlying the hydromagnetic mechanism of wave motions ((i) the presence of regular magnetic field and (ii) the perfect conductivity of gas–dust ISM) leave a little doubt at the conditions typical of the giant molecular clouds and peripheral regions of dark star-forming clouds well ionized by ultraviolet photons, this may be quite different in highly obscured inner regions of dark molecular clouds where the ionizing UV is totally excluded [9]. In this letter we point out that an alternative mechanism of large-scale wave motions of ISM may also be worthy of consideration, particularly in connection with new measurements of magnetic fields toward cores in magnetically supported dark interstellar clouds [1]. Specifically, we present arguments that the supersonic internal velocity dispersion inferred on the basis of recent data [1, 2] may be due to sub-Alfvénic transverse waves of magnetization traveling in poorly ionized gas–dust mediums capable of sustaining, in the presence of a regular magnetic field, the long-range magnetic ordering.

The physical motivation underlying our consideration is based on the well-known Jones and Spitzer arguments [10] regarding the existence of gas–dust interstellar mediums with a highly pronounced property of magnetic polarizability, which can be thought of as a superparamagnetic dispersion of fine ferromagnetic grains suspended in a gaseous cloud of molecular hydrogen. The regular galactic magnetic field threading such a medium introduces anisotropy in the orientation of permanently magnetized solid particles tending to align their magnetic moments. According to [10], the alignment of magnetic grains can be accompanied by filamentary agglomeration of dusty particles (presumably by means of dipole–dipole interaction between magnetic moments of ferrograins) in the form of long-range magnetic chains extending along the direction of the regular magnetic field. A similar mechanism of linear, chainlike magnetic ordering is known in the physics of superparamagnetic ferrocolloidal suspensions placed in a uniform magnetic field, which is due to De Gennes and Pincus [11]. From the standpoint of the condensed matter physics, the filamentary ordering of permanently magnetized dusty particles in the presence of a regular magnetic field can be regarded as an effect of soft magnetic solidification of gas–dust matter imparting to gas–dust ISM the magnetoelastic properties generic to soft materials like uniformly magnetized ferronematic liquid crystals [12, 13] and magnetically saturated elastic insulators [14]. Therefore, it is reasonable to expect that large-scale fluctuations of nonconducting magnetically polarized gas–dust ISM should manifest magnetomechanical behavior typical of the above magnetoelastic materials.

Following this line of argument, we consider a model of a magnetically supported cloud by identifying the two-component gas–dust intercloud medium with single-component superparamagnetic soft matter of equivalent density whose continuum mechanics is described in terms of the velocity of elastic displacements $\mathbf{u}(\mathbf{r}, t)$, the bulk density $\rho(\mathbf{r}, t)$, and the field of magnetization $\mathbf{m}(\mathbf{r}, t)$ (magnetic moment per unit volume). These three quantities are considered on equal

[1] This article was submitted by the authors in English.

footing as independent dynamical variables of dissipative-free motions governed by coupled equations

$$\frac{d\rho}{dt} + \rho\nabla\mathbf{u} = 0, \quad \rho\frac{d\mathbf{u}}{dt} = \frac{1}{2}\nabla\times[\mathbf{m}\times\mathbf{B}], \qquad \frac{d\mathbf{m}}{dt} = [\boldsymbol{\omega}\times\mathbf{m}], \tag{1}$$

which have been derived in [14] by means of systematic application of the conservation laws of the continuum physics. In Eq. (1), $d/dt = \partial/\partial t + \mathbf{u}\nabla$ is the convective derivative and $\boldsymbol{\omega}(\mathbf{r}, t) = (1/2)[\nabla\times\mathbf{u}(\mathbf{r}, t)]$ stands for the vorticity. Notice that for both paramagnets and superparamagnets the linear constitutive equation holds [15]: $\mathbf{M} = \chi\mathbf{B}$, where χ is the magnetic susceptibility, essentially a positive dimensionless constant. The difference is that for superparamagnets this parameter is 5–6 orders of magnitude greater than that for normal paramagnets; that is, for superparamagnets $\chi \sim 0.1$–1. The most important point to be stressed regarding the governing equations of magnetoelastodynamics (1) is that the bulk force originates from interaction between the magnetic field and the field of magnetization which is not direct but is mediated by rotational deformations of an elastic medium, resulting in precession motions of the magnetization under which the direction of $\mathbf{m}$ changes but the magnitude does not. To see that the magnetoelastic bulk force (inherently related to the body–torque density $\mathbf{m}\times\mathbf{B}$) provides stable oscillatory behavior of magnetically polarized gas–dust mediums, we consider long-wavelength, nonradial oscillations of a spherical uniformly magnetized cloud. From electrodynamics of continuous media [16] it is known that in a homogeneous spherical mass of paramagnetic matter with constant magnetization $\mathbf{M}$ inside, the internal magnetic field is uniform and is expressed by the equations $\mathbf{B} + 2\mathbf{H} = 0$ and $\mathbf{B} - \mathbf{H} = 4\pi\mathbf{M}$, from which follows

$$\mathbf{B} = \frac{8\pi}{3}\mathbf{M}. \tag{2}$$

With above reservations in mind, it would not be inconsistent to consider Eq. (2) as a constitutive equation of a superparamagnetic continuum with $\chi = 3/8\pi \approx 0.1$. The advantage of this model is that it allows one to avoid uncertainty in the magnitude of χ.

Making use of the standard procedure of linearization $\mathbf{u} \longrightarrow \mathbf{u}_0 + \delta\mathbf{u}(\mathbf{r}, t)$ and $\mathbf{m} \longrightarrow \mathbf{m}_0 + \delta\mathbf{m}(\mathbf{r}, t)$, where $\mathbf{u}_0 = 0$ and $\mathbf{m}_0 = \mathbf{M}$, we arrive at equations

$$\nabla\delta\mathbf{u}(\mathbf{r}, t) = 0, \quad \nabla\delta\mathbf{m}(\mathbf{r}, t) = 0, \tag{3}$$

$$\rho\frac{\partial\delta\mathbf{u}(\mathbf{r}, t)}{\partial t} = \frac{4\pi}{3}\nabla\times[\delta\mathbf{m}(\mathbf{r}, t)\times\mathbf{M}], \tag{4}$$

$$\frac{\partial\delta\mathbf{m}(\mathbf{r}, t)}{\partial t} = \frac{1}{2}[[\nabla\times\delta\mathbf{u}(\mathbf{r}, t)]\times\mathbf{M}], \tag{5}$$

describing small-amplitude fluctuations of a magnetically saturated, incompressible elastic continuum which are not accompanied by the appearance of density of magnetic poles [right of Eqs. (3)]. In Eq. (4) we have used Eq. (2). The period of magnetoelastic oscillations can be evaluated on the basis of the energy variational principle, which is particularly efficient in studies of long-wavelength nonradial vibrations of spherical masses of incompressible stellar material possessing elastic properties. In particular, this method has been utilized in [17, 18] to compute periods of Alfvén hydromagnetic vibrations of neutron stars and, in [19, 20], the periods of their nonradial gravitational pulsations. The procedure is the following. Scalar multiplication of Eq. (4) with $\delta\mathbf{u}$ and integration over the cloud volume lead to the equation of energy balance

$$\frac{\partial}{\partial t}\int\frac{\rho\delta\mathbf{u}^2}{2}dV = \frac{8\pi}{3}\int[\delta\mathbf{m}\times\mathbf{M}]\delta\boldsymbol{\omega}dV = -\frac{8\pi}{3}\int\delta\mathbf{m}^2dV. \tag{6}$$

The surface integral has been omitted, since in the outer region, the superparamagnetic state should be, most likely, disordered by ambient ionizing ultraviolet radiation. The next step is to represent the velocity of elastic displacements in the following separable form:

$$\delta\mathbf{u}(\mathbf{r}, t) = \boldsymbol{\xi}(\mathbf{r})\dot{\alpha}(t), \quad \delta\boldsymbol{\omega}(\mathbf{r}, t) = \frac{1}{2}[\nabla\times\boldsymbol{\xi}(\mathbf{r})]\dot{\alpha}(t), \tag{7}$$

where $\boldsymbol{\xi}(\mathbf{r})$ is the field of instantaneous elastic displacements and $\alpha(t)$ is the harmonic in time amplitude. The expression for fluctuating vorticity in Eq. (7) is a consequence of separable representation of the fluctuating field of velocity. Inserting Eq. (7) into Eq. (5) and eliminating the time derivative, we obtain

$$\delta\mathbf{m}(\mathbf{r}, t) = \frac{1}{2}[[\nabla\times\boldsymbol{\xi}(\mathbf{r})]\times\mathbf{M}]\alpha(t). \tag{8}$$

After substituting Eqs. (7) and (8) into Eq. (6), this latter is reduced to the equation of normal vibrations

$$\frac{dH}{dt} = 0, \quad H = \frac{M\dot{\alpha}^2}{2} + \frac{K\alpha^2}{2} \longrightarrow M\ddot{\alpha} + K\alpha = 0, \tag{9}$$

with the inertia M and the stiffness K given by

$$M = \int\rho\boldsymbol{\xi}^2dV, \quad K = \frac{2\pi}{3}\int[[\nabla\times\boldsymbol{\xi}]\times\mathbf{M}]^2dV. \tag{10}$$

Thus, to compute the frequency $\omega^2 = K/M$, it is necessary to specify the field of instantaneous displacements $\boldsymbol{\xi}$, which is, as follows from above, of an essentially rotational character. With this in mind, we consider torsional long-wavelength vibrations around the polar axis x of a spherical cloud with the constant magnetization inside pointing in the same direction: $M = [M_x = 0, M_y = 0, M_z = M]$. The kinematics of elastic torsional deformations of a spherical mass is described in detail in [19, 20], and we take advantage of the explicit form

for the velocity given in these papers

$$\delta\mathbf{u}(\mathbf{r}, t) = \frac{1}{2}[\delta\boldsymbol{\omega}(\mathbf{r}, t)\times\mathbf{r}],$$
$$\delta\boldsymbol{\omega}(\mathbf{r}, t) = N_t\nabla r^L P_L(\mu)\dot{\alpha}(t), \qquad (11)$$
$$N_t = \frac{1}{R^{L-1}}, \quad \mu = \cos\theta.$$

Hereafter, $P_L(\mu)$ stands for the Legendre polynomial of the multipole degree L. The corresponding field of instantaneous torsional displacements has the form of the toroidal vector field

$$\boldsymbol{\xi}(\mathbf{r}) = N_t\nabla\times[\mathbf{r}r^L P_L(\mu)]. \qquad (12)$$

Inserting Eq. (12) in Eq. (10), we obtain

$$M = 4\pi\rho R^5\frac{L(L+1)}{(2L+1)(2L+3)},$$
$$K = \frac{8\pi^2}{3}M^2R^3\frac{L(L-1)(L+1)^2}{(4L^2-1)}, \qquad (13)$$

and the eigenfrequency is given by

$$\omega^2 = \omega_M^2(L^2-1)\frac{(2L+3)}{(2L-1)},$$
$$\omega_M^2 = \frac{2\pi}{3}\frac{M^2}{\rho R^2} = \frac{3}{32\pi}\frac{B^2}{\rho R^2}, \qquad (14)$$

where ω_M is the natural unit of frequency of torsional magnetomechanical vibrations, so that the corresponding period is evaluated according to $t_M = 2\pi/\omega_M$.

Let us consider propagation of plane-wave magnetoelastic perturbations in the cloud bulk. Substitution into Eqs. (3)–(5) of the plane-wave form of fluctuating variables

$$\delta\mathbf{u} = \mathbf{u}'\exp(i\omega t - i\mathbf{kr}),$$
$$\delta\mathbf{m} = \mathbf{m}'\exp(i\omega t - i\mathbf{kr}), \qquad (15)$$

with $\mathbf{u}'$ and $\mathbf{m}'$ being some small constant vectors, after some algebra, leads to

$$\omega\rho\delta\mathbf{u} + \frac{4\pi}{3}(\mathbf{kM})\delta\mathbf{m} = 0,$$
$$\omega\delta\mathbf{m} + \frac{1}{2}(\mathbf{kM})\delta\mathbf{u} = 0. \qquad (16)$$

The method of obtaining of these equations is very similar to that utilized in [12] to derive the dispersion relationship of magnetotorsion waves in uniformly magnetized liquid crystals (see also [13]). By eliminating $(\mathbf{kM})$ from Eqs. (16), one finds that magnetoelastic oscillatory motions satisfy the principle of energy equipartition

$$\frac{\rho\delta\mathbf{u}^2}{2} = \frac{4\pi}{3}\delta\mathbf{m}^2, \qquad (17)$$

which states that in a magnetoelastic wave the kinetic energy of fluctuating elastic displacements equals the mean potential energy of fluctuating magnetization. From Eq. (16) it follows that

$$\omega^2 = \frac{(\mathbf{kM})^2}{4\chi\rho} = v_M^2k^2\cos^2\theta,$$
$$v_M^2 = \frac{2\pi}{3}\frac{M^2}{\rho} = \frac{MB}{4\rho} = \frac{3}{32\pi}\frac{B^2}{\rho}, \qquad (18)$$

where θ is the angle between $\mathbf{k}$ and $\mathbf{M}$. The wave is transmitted most efficiently when $\mathbf{k} \parallel \mathbf{M}$. The dispersion relation (18) describes a transverse wave of magnetization in which the vectors of magnetization and velocity undergo coupled oscillations in the plane perpendicular to the axis of magnetic anisotropy directed along $\mathbf{M}$. Both directions $\mathbf{M}$ and $-\mathbf{M}$ are energetically equivalent for this wave. On the other hand, oscillatory motions in a magnetoelastic wave bear a strong resemblance to that for the oscillations of incompressible flow in a perfectly conducting fluid transmitting Alfvén waves in the presence of a uniform magnetic field. Thus, magnetoelastodynamics provides consistent mathematical treatment and physical insight into the nature of waves capable of propagating in the magnetically saturated nonconducting ISM, which can be regarded as a counterpart of Alfvén waves in magnetoactive plasma. However, the very existence of hydromagnetic waves is attributed to the perfect conductivity of cosmic dusty plasma, whereas the considered magnetoelastic waves owe their existence to the magnetic polarizability of nonconducting interstellar mediums.

To show that the presented model can provide proper account of the recent 43-m Green Bank telescope data, reported by Crutcher [1], first, we notice that from analytic estimate for v_M, Eq. (18), it follows that, at equal B and ρ, the considered wave motions are sub-Alfvénic: $v_M \approx 0.6v_A$, where $v_A = B/(4\pi\rho)^{1/2}$ is the speed of Alfvén waves. This prediction is in line with data summarized in [2]. Taking the bulk density $\rho = n\mu_{H_2} \approx 3.9\times10^{-21}$ g/cm^3 (where $n = 10^3$ cm^{-3} and μ_{H_2} is the mass of the hydrogen molecule [1]) and the magnetic field $B = 10$ μG [1], one finds that the speed of the wave of magnetization $v_M \approx 0.28$ km/s; that is, it exceeds the isothermal sound speed $c_s = (k_BT/\mu_{H_2})^{1/2} \approx 0.19$ km/s at the average intercloud temperature $T \approx 10$ K [1]. So, under conditions typical of inner regions of dark star-forming molecular clouds, the waves of magnetization are, most likely, supersonic. The characteristic time (period) of long-wavelength oscillations of a magnetic cloud is estimated (in seconds) to be $t_M = 2\pi/\omega_M = 2\pi R/v_M = 22.4\times10^{-5}R$, where R is the cloud radius. The fact that the above predictions are not inconsistent with available data (Crutcher *et al.*, 1996; Crutcher, 1999) suggests that supersonic motions observed toward the core of dark molecular clouds

poorly ionized by ultraviolet photons may be due to wave motions considered here.

The authors acknowledge partial support (J.Y.) from the Korean Research Foundation, grant 1999-015-DI0021, and (S.B.) from the Asia Pacific Center for Theoretical Physics.

REFERENCES

1. R. M. Crutcher, Astrophys. J. **520**, 706 (1999).
2. R. M. Crutcher, T. H. Troland, B. Lazareff, and I. Kazès, Astrophys. J. **456**, 217 (1996).
3. R. M. Crutcher, T. H. Troland, A. A. Goodman, *et al.*, Astrophys. J. **407**, 175 (1993).
4. P. Padoan and Å. Nordlund, Astrophys. J. **526**, 279 (1999).
5. J. M. Stone, E. C. Ostriker, and C. F. Gammie, Astrophys. J. Lett. **508**, L99 (1998); C. F. Gammie and E. C. Ostriker, Astrophys. J. **466**, 814 (1996).
6. T. Nakano, Astrophys. J. **494**, 587 (1998).
7. M. M. McLow, R. S. Klessen, A. Burkert, and M. D. Smith, Phys. Rev. Lett. **80**, 2754 (1998).
8. J. Arons and C. E. Max, Astrophys. J. Lett. **196**, L77 (1975).
9. W. W. Duley and D. A. Williams, Mon. Not. R. Astron. Soc. **260**, 37 (1993).
10. R. V. Jones and L. Spitzer, Astrophys. J. **146**, 943 (1967).
11. P. J. De Gennes and P. A. Pincus, Phys. Condens. Matter **11**, 189 (1970).
12. S. I. Bastrukov and P. Y. Lai, J. Phys.: Condens. Matter **11**, L205 (1999).
13. S. I. Bastrukov and P. Y. Lai, Phys. Scr. **61**, 369 (2000).
14. H. F. Tiersten, J. Math. Phys. **5**, 1298 (1964).
15. C. Kittel, *Introduction to Solid State Physics* (Wiley, New York, 1996, 7th ed.; Nauka, Moscow, 1978).
16. L. D. Landau, E. M. Lifshitz, and L. P. Pitaevskiĭ, *Electrodynamics of Continuous Media* (Nauka, Moscow, 1982; Pergamon, New York, 1995, 3rd ed.), Para. 76, Problem 2, p. 264.
17. S. I. Bastrukov and D. V. Podgaĭny, Phys. Rev. E **54**, 4465 (1996); Astron. Zh. **74**, 910 (1997) [Astron. Rep. **41**, 813 (1997)].
18. S. I. Bastrukov, V. V. Papoyan, and D. V. Podgaĭny, Pis'ma Zh. Éksp. Teor. Fiz. **64**, 593 (1996) [JETP Lett. **64**, 637 (1996)]; Astrophysics **39**, 475 (1996).
19. S. I. Bastrukov, Phys. Rev. E **53**, 1917 (1996).
20. S. I. Bastrukov, F. Weber, and D. V. Podgaĭny, J. Phys. G **25**, 107 (1999).

JETP Letters, Vol. 71, No. 10, 2000, pp. 399–402. Translated from Pis'ma v Zhurnal Éksperimental'noĭ i Teoreticheskoĭ Fiziki, Vol. 71, No. 10, 2000, pp. 583–587.

PLASMA, GASES

TEA CO_2 Laser-Induced Selective Molecular Dissociation in a Cold Shock Wave

G. N. Makarov* and A. N. Petin**

* *Institute of Spectroscopy, Russian Academy of Sciences, Troitsk, Moscow region, 142190 Russia*
e-mail: g.makarov@isan.troitsk.ru
** *Troitsk Institute for Innovation and Thermonuclear Research, Troitsk, Moscow region, 142190 Russia*
Received March 27, 2000; in final form, April 25, 2000

Selective molecular IR multiphoton dissociation (SF_6 was taken as an example) was studied under the nonequilibrium conditions of a cold shock wave (pressure shock) formed upon the interaction of a pulsed gas-dynamically cooled molecular flow with a solid surface. An anomalously large gain (by more than an order of magnitude) in the product yield (compared to the molecular excitation in an unperturbed flow) with a minor selectivity loss (less than 25–30%) was observed. © *2000 MAIK "Nauka/Interperiodica".*

PACS numbers: 33.80.-b; 42.62.Fi; 82.40.Fp; 82.50.Fv

1. The use of gas-dynamic cooling of molecular jets and flows [1] for enhancing selectivity of laser-induced processes, including selective molecular IR multiphoton dissociation [2–4], is well known. Strong gas cooling leads to a sharp narrowing of molecular absorption bands and an ensuing increase in the selectivity of excitation and dissociation processes. However, photochemical processes in jets and flows are inefficient. Because of low concentration of molecules and low gas temperature, the rates of chemical reactions, including those yielding target products, are low. This paper reports the results of the experiment on studying isotope-selective molecular IR multiphoton dissociation (SF_6 was taken as an example) under the nonequilibrium conditions of a cold shock wave (pressure shock) formed upon the interaction of a pulsed gas-dynamically cooled molecular flow with a solid surface. An anomalously large increase (by 10–20 times) in the product yield, as compared to the molecular excitation in an unperturbed flow, was observed with a minor selectivity loss.

2. The scheme of the experiment is shown in Fig. 1. Molecular flow was produced by a pulsed nozzle of the "current loop" type [5] with a hole diameter of 0.75 mm. The duration of the nozzle-gating pulse was $\cong$100 μs. Gas pressure over the nozzle could be varied in the range 0.1–3 atm. Two thin metallic strips attached to the nozzle exit cone formed a molecular flow [4] in a vacuum chamber evacuated to a pressure of $(1–2) \times 10^{-6}$ torr. The number of molecules flowing out of the nozzle in one pulse depended on the pressure over the nozzle and varied from $\cong 10^{16}$ to $\cong 10^{17}$ molecules/pulse in the experiments. Mean velocity of the flow molecules was measured by the time-of-flight technique [6, 7] and found to be 420 ± 20 m/s.

At a distance of $\cong$50–150 mm from the nozzle, a solid surface (plates made from KBr or CaF_2 crystal) was installed perpendicularly to the flow. The supersonic molecular flow interacted with the surface to produce a pressure shock (shock wave) ahead of it [8–11] under the strongly nonuniform, nonstationary, and nonequilibrium conditions. The characteristic wave front size (on the order of a molecular mean free path [8, 9]) was equal to 0.2–5 mm in our experiments.

The molecules were excited near the surface at a distance of Δx = 1.5–3 mm from it. Laser radiation was focused into this region by a cylindrical lens with focal distance of 12 cm. The lens axis was parallel to the surface. The laser beam cross section in the lens focus was $\cong 0.18 \times 12$ mm.

The molecular dissociation was studied in a normal shock and in the unperturbed flow (without a surface in the path of the flow). The experiments consisted of measuring the intensity of HF* luminescence ($\lambda \cong 2.5$ μm) accompanying the SF_6 dissociation in the presence of H_2 or CH_4, so that it was taken as a measure of the SF_6 dissociation yield [3]. The SF_4 product yield and its enrichment with the ^{34}S isotope were also measured. The HF* luminescence was recorded on a PbS IR detector with detecting area 1×1 cm. The enrichment factor for SF_4 was defined as

$$K_{34}^{prod} = [^{34}SF_4]/[^{32}SF_4]\zeta,$$

where $[^{34}SF_4]/[^{32}SF_4]$ is the concentration ratio of the molecules (indicated in brackets) in the SF_4 product and $\zeta = {}^{34}S/{}^{32}S \cong 0.044$ is the percentage ratio of sulfur isotopes in the initial SF_6 gas. The ratio of $^{34}SF_4$ and $^{32}SF_4$ concentrations in the product was determined

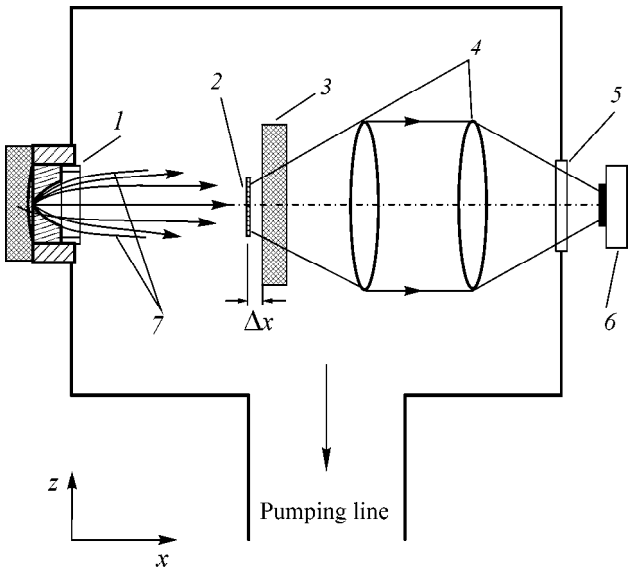

Fig. 1. Scheme of experimental setup (the section in the *xz*-plane; laser beam is directed along the *y*-axis). (*1*) Pulsed nozzle, (*2*) laser beam, (*3*) surface (KBr or CaF_2), (*4*) condenser, (*5*) window, (*6*) IR detector, and (*7*) strips forming molecular flow.

from the IR spectra in the ν_6 range (728 cm^{-1}), where the isotope shift for $^{32}SF_4$ and $^{34}SF_4$ is equal to $\cong$12.3 cm^{-1} [12].

3. The HF* luminescence intensity is shown in Fig. 2 as a function of the time delay τ_d between the nozzle and the TEA CO_2 laser pulses for the cases when SF_6 is excited in a mixture with CH_4 (SF_6/CH_4 = 10/1) in an unperturbed flow (curve *1*) and in a flow interacting with the surface (curve *2*). The total gas pressure over the nozzle was 1 atm. The separation between the nozzle and surface was 51 mm, and Δx = 2.5 mm. It is seen that the maximum of the HF* luminescence intensity in the case of SF_6 excitation in the flow interacting with the surface is almost an order of magnitude greater than in the case of the unperturbed flow. A sharp shock front appears in the zone of molecular excitation (at a distance of Δx = 2.5 mm from the surface) at τ_d = 370 μs. For smaller distances Δx between the surface and the excitation zone, the HF* luminescence emission peak was observed at smaller time delays τ_d, while its intensity increased. For example, the shock front for Δx = 1.6 mm was observed at τ_d = 310 μs, while the HF* intensity in the shock was approximately 20 times higher than in the unperturbed flow.

In Fig. 3, the HF* luminescence intensity is shown as a function of the gas pressure over the nozzle for the cases when SF_6 is excited in a mixture with CH_4 (SF_6/CH_4 = 1/1) in the unperturbed flow (curve *1*) and in the shock (curve *2*). The distance from the nozzle to the surface was 102 mm, and Δx = 2.5 mm. It is seen that, over the whole pressure range studied, the HF* luminescence in the shock is appreciably (more than 20-fold) stronger than in the unperturbed flow.

We also directly measured the yield of the final SF_4 product formed upon the excitation of molecules in the shock and in the unperturbed flow. The measuring technique was described in [4, 13]. The SF_4 yield was measured for the unperturbed flow at τ_d = 260 μs and, for the flow interacting with surface, at τ_d = 260 and

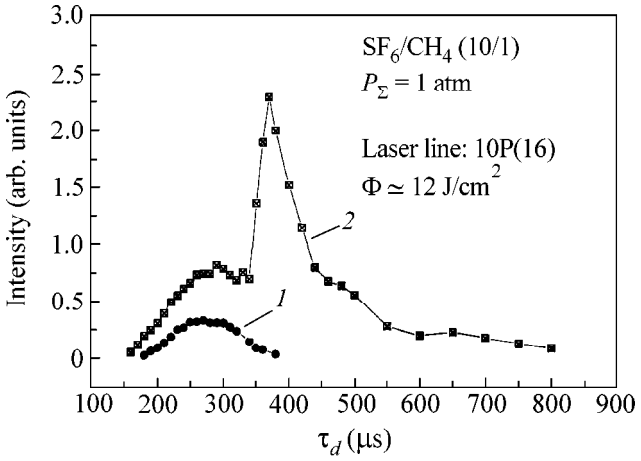

Fig. 2. The HF* luminescence intensity as a function of time delay τ_d between the nozzle and the TEA CO_2 laser pulses exciting SF_6 in a mixture with CH_4 (SF_6/CH_4 = 10/1) in (curve *1*) the unperturbed flow and (curve *2*) the flow interacting with the surface.

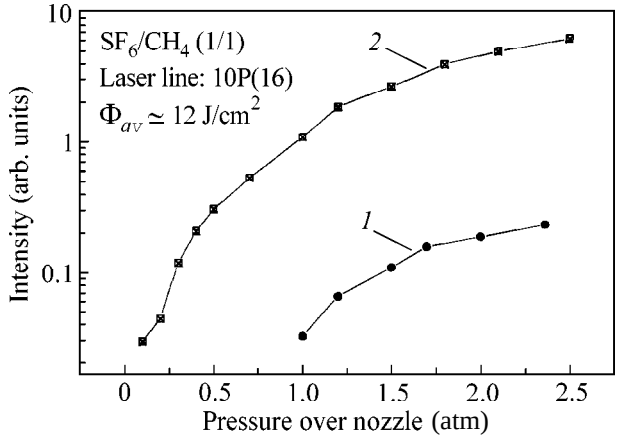

Fig. 3. The HF* luminescence intensity as a function of gas pressure over the nozzle for the excitation of SF_6 in a mixture with CH_4 (SF_6/CH_4 = 1/1) in (curve *1*) the unperturbed flow and (curve *2*) the shock.

370 μs. These time delays corresponded to the maxima in the time-of-flight spectra (cf. Fig. 2). The distance from the nozzle to the surface was 51 mm, and Δx = 2.5 mm. The SF_6 pressure over the nozzle was 1.25 atm. It was found that, for the molecules excited in the flow interacting with surface, the SF_4 yield at τ_d = 260 μs was 2.5 times higher, while, in the shock (at τ_d = 370 μs), it was approximately 12 times higher than in the unperturbed flow. Note that similar results were also obtained for the CF_3I molecule. The yield of the C_2F_6 product in the shock was approximately 16 times higher than in the unperturbed flow.

To study the selectivity of the process, the enrichment factor was measured for the ^{34}S isotope in SF_4 arising upon SF_6 excitation both in the shock and in the unperturbed flow. The molecules were excited at a frequency of 929 cm^{-1} [the 10P(36) line of the CO_2 laser] coinciding with the ν_3 mode of $^{34}SF_6$ [14]. At the energy density of ≅12 J/cm^2, the enrichment factor was found to be $K_{34}^{prod} = 17 \pm 4$ for the molecules excited in the unperturbed flow and $K_{34}^{prod} = 14 \pm 3$ for the molecules excited in the shock. Therefore, the product yield in the shock is more than an order of magnitude higher than in the incident flow, whereas the loss in selectivity is quite small.

The product yield increases in the shock because of an increase in (1) gas density, (2) rate of chemical reaction, and (3) dissociation yield. The latter occurs because (i) the excitation in the shock is more efficient and (ii) the molecules excited by the IR pulse below the dissociation threshold and, hence, not dissociating in the collision-deficient unperturbed flow, undergo collisional dissociation in the shock. The limiting increase in the gas density in a normal shock is determined by the formula [8–10] $\rho_2/\rho_1 = (\gamma + 1)/(\gamma - 1)$, where ρ_1 and ρ_2 are the gas densities in the incident flow and the shock, respectively, and $\gamma = c_p/c_v$ is the ratio of specific heats. For SF_6, $\gamma \cong 1.1$, so that $\rho_2/\rho_1 \cong 21$. Note that the limiting density was not achieved at a distance of Δx = 2.5 mm from the surface in these experiments (the HF* emission was more intense at shorter Δx distances), so that the increase in the SF_4 yield in the shock was likely caused not only by the increase in the gas density but also by the other factors discussed above.

The selectivity in the shock is rather high, because the molecular vibrational and, possibly, rotational temperatures in the flow interacting with the surface are low. As a rule, the gas-dynamically cooled molecular flow is nonequilibrium: $T_{1,\,tr} \le T_{1,\,rot} \le T_{1,\,vib}$ ($T_{1,\,tr}$, $T_{1,\,rot}$, and $T_{1,\,vib}$ are the translational, rotational, and vibrational temperatures of molecules, respectively). Because of the different translational, rotational, and vibrational relaxation rates [11], "inverse" nonequilibrium conditions may be realized in the shock: $T_{2,\,tr} \ge T_{2,\,rot} \ge T_{2,\,vib}$. In the case of a pulsed flow of low-density gas, the vibrational temperature in the shock may almost coincide with the vibrational temperature in the incident flow ($T_{2,\,vib} \cong T_{1,\,vib}$), because the vibrational–translational relaxation time is long (for SF_6, $p\tau_{V-T} \cong$ 150 μs torr [15]). However, $T_{2,\,tr} > T_{1,\,tr}$ and $T_{2,\,rot} > T_{1,\,rot}$. The deceleration-induced gas heating in the shock can be estimated as [8, 10] $\Delta T = v_0^2/2c_p$, where v_0 is the flow rate and c_p is the gas specific heat. Substituting the corresponding values for SF_6 ($v_0 \cong$ 420 m/s and $c_p \cong$ 665 J/(kg K), one obtains $\Delta T \cong$ 130 K. With the translational temperature of $T_{1,\,tr} \le$ 40 K for SF_6 in the incident flow [7], $T_{2,\,tr} \le$170 K in the shock. It is worth noting that, insofar as the specific heat of SF_6 in the gas-dynamically cooled flow is probably smaller than the value used above for $T \cong$ 300 K, the translational temperature $T_{2,\,tr}$ may also be higher than the above estimate. The rotational and translational temperatures are likely close to each other, while the vibrational temperature $T_{2,\,vib} \cong T_{1,\,vib} \le$ 150 K [7]. For this reason, if the vibrational temperature of molecules dominates the selectivity, then the dissociation selectivity in the shock should not strongly differ from that in the incident flow, just as was observed in our experiments. Note also that the heating-induced selectivity decrease in the shock in some cases may be compensated by its increase caused by an increase in the concentration of illuminated molecules [16].

We are grateful to V.N. Lokhman and S.A. Mochalov for assistance in preparing the manuscript. This work was supported in part by the Russian Foundation for Basic Research, project no. 00-03-33003a.

REFERENCES

1. J. B. Anderson, in *Gasdynamics, Molecular Beams and Low Density Gasdynamics* (Marcel Dekker, New York, 1974), Vol. 4, p.1.
2. V. N. Bagratashvili, V. S. Letokhov, A. A. Makarov, and E. A. Ryabov, *Multiple Photon Infrared Laser Photophysics and Photochemistry* (Harwood, New York, 1985).
3. S. S. Alimpiev, G. S. Baronov, S. M. Karavaev, *et al.*, Kvantovaya Élektron. (Moscow) **10**, 376 (1983).
4. G. N. Makarov, V. N. Lokhman, D. E. Malinovskiĭ, and D. D. Ogurok, Kvantovaya Élektron. (Moscow) **25**, 545 (1998).
5. W. R. Gentry and C. F. Giese, Rev. Sci. Instrum. **49**, 595 (1978).
6. V. M. Apatin, L. M. Dorozhkin, G. N. Makarov, and L. M. Pleshkov, Appl. Phys. B **29**, 273 (1982).
7. V. M. Apatin and G. N. Makarov, Zh. Éksp. Teor. Fiz. **84**, 15 (1983) [Sov. Phys. JETP **57**, 8 (1983)].
8. Ya. B. Zel'dovich and Yu. P. Raizer (Raĭzer), *Physics of Shock Waves and High-Temperature Hydrodynamic Phenomena* (Nauka, Moscow, 1966; Academic, New York, 1966, 1967).

9. L. D. Landau and E. M. Lifshitz, *Fluid Mechanics* (Nauka, Moscow, 1986; Pergamon, Oxford, 1987).
10. G. N. Abramovich, *Applied Gas Dynamics* (Nauka, Moscow, 1991), Part 1.
11. E. V. Stupochenko, S. A. Losev, and A. I. Osipov, *Relaxation Processes in Shock Waves* (Nauka, Moscow, 1965).
12. K. O. Christe, E. C. Curtis, C. J. Schack, *et al.*, Spectrochim. Acta, Part A **32**, 1141 (1976).
13. G. N. Makarov, D. E. Malinovsky, and D. D. Ogurok, Laser Chem. **17**, 205 (1998).
14. R. S. McDowell, B. J. Krohn, H. Flicker, and M. C. Vásquez, Spectrochim. Acta, Part A **42**, 351 (1986).
15. J. I. Steinfeld, I. Burak, D. G. Sutton, and A. V. Novak, J. Chem. Phys. **52**, 5421 (1970).
16. G. N. Makarov, Pis'ma Zh. Tekh. Fiz. **24**, 35 (1998) [Tech. Phys. Lett. **24**, 921 (1998)].

Translated by V. Sakun

JETP Letters, Vol. 71, No. 10, 2000, pp. 403–406. From Pis'ma v Zhurnal Éksperimental'noĭ i Teoreticheskoĭ Fiziki, Vol. 71, No. 10, 2000, pp. 588–592.

PLASMA, GASES

Cluster Generation from Flowing Plasma[1]

B. M. Smirnov

Institute of High Temperatures Scientific Association (IVTAN), Russian Academy of Sciences, Izhorskaya ul. 13/19, Moscow, 127412 Russia

e-mail: smirnov@orc.ru

Received February 4, 2000; in final form, March 27, 2000

The method of generation of cluster beams is analyzed in the regime when large clusters grow in a flow of a dense afterglow plasma and clusters are formed in a narrow region near the axis of this flow. This method gives a high intensity of the cluster beam in comparison with standard methods of cluster generation. Numerical parameters are evaluated for processes involving iridium clusters in an argon plasma. © *2000 MAIK "Nauka/Interperiodica".*

PACS numbers: 36.40.Wa; 61.46.+w; 52.20.-j

The method of generation of clusters from a plasma [1] deals with growing clusters in a dense plasma. This method is profitable for metals with a not low boiling temperature when the standard method of transformation of a vapor into clusters [2–6] is useless because of low pressures of metallic vapors and the laser method of cluster generation [7–10] gives a low intensity and small cluster sizes. The afterglow plasma in which clusters grow consists of a dense buffer gas and a small admixture of a metal which is inserted in the plasma in the form of a gaseous compound and exists in this form in a cold plasma region. In a hot region, this compound is decomposed into an atomic vapor and metallic clusters grow in the plasma. These clusters reach large sizes because of the large time of the cluster growth process. Since clusters are charged, they can be separated from a plasma, and this method provides intense cluster beams. The analysis of these processes was made recently [1]. Now we focus on the regime of plasma evolution when clusters are formed near the center of the plasma flow and analyze the processes during evolution of this cluster plasma.

Gasdynamics and heat processes in plasma flow. The generator of cluster beams under consideration consists of three basic elements. The first one is a plasma generator of low power (below 1 kW), and in the second part of this generator a narrow beam of molecules containing metallic atoms is inserted near the axis of the flowing afterglow plasma. Molecules are decomposed in this region, and forming metallic atoms, join in clusters or attach to clusters. As a result, all the metal is collected near the flow axis in the form of clusters. After this stage, the central flow part is directed into a vacuum through a nozzle where atoms of a buffer gas are removed by pumping and the beam of charged clusters is governed by external electric fields.

When a gaseous compound of a heat-resistant metal is inserted in a flow of a buffer gas, molecules of the compound are mixed with the gas and are decomposed into atoms in hot regions in which temperatures exceed the boundary temperature T_1 of their decay. An atomic vapor of a heat-resistant metal may be transformed into a gas of clusters in regions in which temperatures are below the boundary temperature T_2 of existence of these clusters. In the second part of the cluster generator, where clusters are formed, the flow temperature at the center varies from T_2 up to T_1. For definiteness, below we will guided by the compound IrF_6 inserted with concentration of 10^{-3} in argon at a pressure of 100 torr, so that the forming iridium clusters can be used for fabrication of rhodium–iridium thermocouples. In this case, we have T_1 = 1300 K, T_2 = 3200 K with the accuracy 100–200 K.

Because of a small concentration, the metallic compound does not influence the gasdynamical and thermal properties of a plasma flow. We take a simple parabolic temperature distribution over the flow cross section. Introducing an effective temperature T_{eff} of the flow, we have for the flow rate

$$Q = \int N_a u_z 2\pi\rho d\rho = N_a(T_{ef}) u_z \pi r_0^2, \qquad (1)$$

where ρ is the distance from the tube center and r_0 is the tube radius. Under the argon pressure of p = 100 torr, the center flow temperature T_0 = 3000 K, the tube radius r_0 = 1 cm, and the average flow speed $u_z = 6 \times 10^3$ cm/s, we have for the effective flow temperature T_{eff} = 1800 K, and the flow rate is $Q = 1 \times 10^{22}$ s^{-1} = 0.7 g/s. Then the Reynolds number is $\text{Re} = u_z r_0 m_a N_a(T_{\text{eff}})/\eta(T_{\text{eff}}) \sim 300$, where m_a is the atom mass, $\eta(T_{\text{eff}})$ is a typical gas viscosity, and the gas flow is laminar. Next, from the Navier–Stokes equation it follows for the pressure gra-

[1] This article was submitted by the author in English.

dient $dp/dz = 2 \times 10^{-3}$ torr/cm under the above parameters. This means that we have p = const along the flow.

Cooling of this plasma is determined in part by heat transport to the walls due to the gas thermal conductivity, and the heat balance equation for the afterglow plasma has the form

$$u_z H = 2\pi r_0 \kappa \frac{dT}{d\rho}(r_0) = 4\pi\kappa(T_w)\Delta T. \quad (2)$$

Here, $H = \int c_p T(\rho) N_a 2\pi\rho d\rho \approx c_p Q(T_{\text{eff}} - T_w)/u_z$ is the enthalpy per unit length of the flow, c_p is the specific heat capacity per atom of a buffer gas, and $\kappa(T_w)$ is the thermal conductivity coefficient of a buffer gas near the walls. In particular, under the above flow conditions, we have $u_z H = 400$ W and $4\pi\kappa\Delta T = 7$ W/cm. At laboratory tube lengths $l \approx 30$–40 cm, the flow cooling from T_2 up to T_1 can be attained additionally by a tube expansion.

The basic condition for the flow parameters is such that, on the one hand, decay of molecules at the flow center proceeds rapidly, and, on the other hand, nucleation of a forming metallic vapor is possible there. The rate constant of detachment of halogen atoms in collisions of a molecule with argon atoms can be represented in the form $k_{\text{det}} = k_g \exp(-\varepsilon_{\text{ch}}/T)$, where in the iridium case at $T = 3000$ K, the gas-kinetic rate constant is $k_g = 2 \times 10^{-10}$ cm^3/s and ε_{ch} is the binding energy of halogen atoms in the molecule ($\varepsilon_{\text{ch}} \approx 2.5$ eV for the IrF_6 molecule). Under the conditions considered, the decay of molecules proceeds during a time $\tau_{\text{ch}} \sim 10^{-4}$ s at $T = 3000$ K. This process leads to cooling of the buffer gas, and at the concentration 10^{-3} of the IrF_6 molecules the temperature decrease is $\delta T = 60$–70 K on average. In reality, the cooling is stronger, because decay of molecules proceeds rapidly and heat is taken from a restricted central region of the flow. This effect is compensated particularly by heat release resulting from formation of metallic clusters. The optimal temperature at the center can be operated by the initial plasma temperature.

Nucleation and charging processes in afterglow plasma. The character of the nucleation process in this plasma is similar to that in the case when an atomic vapor is transformed in a gas of clusters in a buffer gas [11]. Indeed, the first stage of the nucleation process is the formation of diatomic metallic molecules in three-body collisions of metallic atoms and atoms of the buffer gas, and then diatomic molecules are nuclei of condensation for cluster growth. Therefore, clusters are large at the end of the growth process and a typical time τ of transformation of metallic atoms into clusters and the average cluster size n (the number of cluster atoms) are given by [11]

$$\tau \sim \frac{1}{k_0 N}\left(\frac{k_0}{K_3 N_a}\right)^{1/4}, \quad n \sim (k_0 N \tau)^3 \sim \left(\frac{k_0}{K_3 N_a}\right)^{3/4}. \quad (3)$$

Here, k_0 is the specific rate constant of atom attachment to a cluster ($k_0 = 3 \times 10^{-11}$ cm^3/s for iridium at $T = 3000$ K), $K_3 \sim 10^{-33}$ cm^6/s is the three-body rate constant of formation of diatomic molecules in three-body collisions, N_a is the number density of atoms of a buffer gas, and N is the number density of free and bound metallic atoms. In particular, in the iridium case under consideration, the transformation time is $\tau \sim 10^{-4}$ s and the mean cluster size is $n \approx 7 \times 10^3$.

The nucleation process proceeds in a narrow region near the axis. In particular, the way Δx which atoms pass into a buffer gas during the transformation process is $\Delta x \sim \sqrt{D\tau} \sim 0.1$ cm, where $D \approx 50$ cm^2/s is the diffusion coefficient of metallic atoms in a buffer gas at the tube axis. As a result of the nucleation and diffusion processes, the effective radius of the region occupied by clusters is $\rho_0 = 0.2$ cm in the iridium case and is smaller than the tube radius. Thus, the formed clusters are located in a narrow region near the axis and do not change their positions during the flight time because of a large mass. The subsequent cluster growth results from coagulation of clusters, but during the flight time at the axis $\tau_{fl} \sim 3 \times 10^{-3}$ s this process virtually does not change the mean cluster size in this case.

Charging of clusters proceeds simultaneously with cluster growth. When clusters are forming, the charging process results from the equilibrium

$$e + M_n^{-Z} \longleftrightarrow M_n^{-Z-1}, \quad A^+ + M_n^{-Z} \longleftrightarrow A + M_n^{-Z+1}, \quad (4)$$

where e, M, A are an electron, a metallic atom, and a buffer gas atom, respectively, and the cluster charge Z for iridium clusters in argon is equal in electron charges to

$$Z/n^{1/3} = 0.08(T/1000), \quad (5)$$

where the temperature T is expressed in K and we assume Ar^+ to be the basic ion in argon. Similar values of the charge correspond to other metals. In particular, averaging over 18 heat-resistant metals gives for the numerical coefficient in Eq. (5) 0.080 ± 0.005, if the clusters are located in argon.

Processes (4) also determine the rate of recombination of this plasma. The rate of attachment of electrons and ions to clusters is

$$1/\tau_{at} = k_1 N_b / n^{1/3}. \quad (6)$$

The rate constant is $k_1 \sim 10^{-10}$ cm^3/s, N_b is the number density of bound atoms in clusters, and in the iridium case we have $1/\tau_{at} \sim 10^5$ s^{-1}. As a result of processes (4), the number density of electrons and ions drops rapidly in the region occupied by clusters. One can neglect the thermoemission of electrons from the cluster surface if the following criterion is valid:

$$1/\tau_{\text{rel}} \ll (dT/dt)(W/T^2), \quad (7)$$

Table

N_e, cm^{-3}	10^8	10^{10}	10^{12}	10^{14}
T_*, 10^3 K	1.85	2.19	2.69	3.47
$\nu_{em}/n^{2/3}$, s^{-1}	1.2	170	2.6×10^4	4.2×10^6

where τ_{rel} is a typical time of a decrease in the plasma density and W is the metal work function, which is the ionization potential of a large cluster. In the iridium case the right-hand side of this relation is equal to $\sim 4 \times 10^3$ s^{-1}, so that at the first stage of cluster evolution, the criterion (7) is not fulfilled. Hence, through a time $\sim\tau_{at}$, when the plasma number density drops significantly, thermoemission of electrons becomes responsible for the charge equilibrium of clusters. The table lists the temperatures T_* at which the cluster charge is zero at a given number density N_e of electrons and the rates $\nu_{em}(T_*)$ of thermoemission of electrons for iridium clusters. If the thermoemission process is dominant in cluster charging and released electrons remain in the cluster region, the positive charge of clusters is close to zero because of a high number density of clusters.

At low temperatures the cluster charge is determined by transport of electrons and ions to the cluster region from regions where clusters are absent. We have the following balance equation for the plasma density:

$$\rho_0^2 \frac{N_e'}{\tau_a} \sim D_a N_e. \qquad (8)$$

Here, ρ_0 the radius of a region containing clusters, N_e' is the electron number density in this region, N_e is the electron number density in neighboring regions where clusters are absent, and D_a is the coefficient of ambipolar diffusion of the plasma. In particular, in the iridium case at the flow exit ($T = 1500$ K near the axis), we have $N_e = 3 \times 10^{12}$ cm^{-3} and $N_e' \sim 1 \times 10^{10}$ cm^{-3}. A typical relaxation time due to transport of electrons and ions to walls is $\tau_{rel} \sim 0.1$ s. Hence, the criterion (7) holds true now, and clusters get a negative charge which is lower than that according to Eq. (5) because of the large time of establishment of equilibrium (4). As a result, clusters are charged negatively and equilibrium (4) may be partially restored at low temperatures.

Processes in an expanding afterglow plasma. At the last stage of plasma evolution, the central part of a plasma flow which contains clusters passes through a nozzle in a vacuum. Then, atoms of a buffer gas are extracted by pumping and the beam of clusters is crossed by an electron beam, so that the clusters obtain a negative charge. This cluster beam can be governed by external transverse and longitudinal electric fields when the buffer gas pressure becomes small. In particular, the mobility of charged iridium clusters reduced to the normal density of argon atoms under equilibrium (4) is $K = K_0 n^{-1/3}$, where $K_0 = 0.47$ cm^2(V s) at $T = 1000$ K. From this it follows that transport of charged clusters in an external field is negligible in a plasma flow and can be remarkable in a vacuum chamber when the gas pressure becomes small. Then the cluster beam can be focused and accelerated.out of

When the afterglow plasma with clusters flows after a nozzle and expands in a vacuum, atomic particles are scattered and pumped from the plasma flow, while collisions of clusters with atoms of a buffer gas do not create a remarkable transverse momentum of an individual cluster because of the large cluster mass. Pumping allows one to remove the scattered atoms which move towards the walls. As a result, after a while, the plasma flow is transformed into a beam of clusters. Collection of clusters near the center of the plasma flow allows us to use only the central flow part for generation of a cluster beam.

Above, we neglect the presence of halogen atoms in the plasma flow. Indeed, at high temperatures $T > T_1$, the halogen atoms do not react with clusters, and at low temperatures, these atoms are pumped out. Nevertheless, halogen atoms can partake in some processes; in particular, attachment of electrons to halogen atoms can change the plasma properties and the character of cluster charging. In addition, the presence of halogen atoms in a buffer gas requires a certain wall material and a special purification of the pumped buffer gas. Hence, this problem demands an additional analysis.

Thus, generation of a cluster beam from a plasma is determined by competition of some processes and is possible in a certain range of plasma parameters. In particular, at the first stage of the process, on the one hand, a fast decomposition of molecules is required with formation of metallic atoms at the flow axis and, on the other hand, a fast nucleation of metallic atoms must proceed in this region. Although due to competition of various processes, this method requires a special analysis for each specific case, it can be used for generation of cluster beams of various heat-resistant metals.

As follows from the above analysis, generation of a cluster beam from a plasma includes a variety of competing processes and provides a high intensity of the output cluster beam. In particular, the maximum specific intensity of clusters is 80 μg/(cm^2 s) [12] for the standard method and silver clusters. In the iridium case under consideration, we have for this value 20 mg/(cm^2 s) and 3 mg/s for the total rate of clusters. Note the importance of chemical regeneration [13] in this method, which provides a high number density of metallic atoms. If metallic atoms result from metal vaporization, the num-

ber density of atoms cannot exceed that at the saturated vapor pressure. In particular, for iridium, this value at the melting point is 3×10^{13} cm^{-3}, while using decomposition of IrF_6 molecules allows one to increase this value by two to three orders of magnitude. In addition, collection of clusters near the flow axis simplifies extraction of clusters from the plasma flow and increases the specific intensity of the beam of metallic clusters. Because all the metal is transformed into clusters, this method of generation of cluster beams can provide the same rate of metal deposition on targets as that in the case of beams of atoms or atomic ions. But intense beams of charged clusters are governed better than intense beams of atomic ions. Therefore, the cluster technology of deposition of films of heat-resistant metals has advantages with respect to use atomic beams and atomic ion beams.

This study was supported in part by the Russian Foundation for Basic Research, project no. 99-02-16094.

REFERENCES

1. B. M. Smirnov, Pis'ma Zh. Éksp. Teor. Fiz. **68**, 741 (1998) [JETP Lett. **68**, 779 (1998)]; J. Phys. D **33**, 115 (2000).
2. E. W. Becker, K. Bier, and W. Henkes, Z. Phys. **146**, 333 (1956).
3. W. Henkes, Z. Naturforsch. A **16**, 842 (1961); **17**, 786 (1962).
4. O. F. Hagena, Z. Phys. D **4**, 291 (1987); **17**, 157 (1990); **20**, 425 (1991).
5. J. Gspann, Z. Phys. D **3**, 143 (1986); **20**, 421 (1991).
6. H. Haberland, M. Mall, M. Moseler, *et al.*, J. Vac. Sci. Technol. A **12**, 2925 (1994).
7. R. E. Smalley, Laser Chem. **2**, 167 (1983).
8. P. Milani and W. A. de Heer, Rev. Sci. Instrum. **61**, 1835 (1990).
9. O. Cheshnovsky, S. H. Yang, C. L. Pettiette, *et al.*, Chem. Phys. Lett. **139**, 233 (1987); Rev. Sci. Instrum. **58**, 2131 (1987).
10. A. Perez, P. Melinon, V. Dupuis, *et al.*, J. Phys. D **30**, 709 (1997).
11. B. M. Smirnov, Usp. Fiz. Nauk **167**, 1169 (1997) [Phys. Usp. **40**, 1117 (1997)].
12. O. F. Hagena, G. Knop, and G. Linker, in *Physics and Chemistry of Finite Systems: From Clusters to Crystals*, Ed. by P. Jena, B. K. Rao, and S. N. Khanna (Kluwer, Amsterdam, 1992), Vol. II, p.1233.
13. B. Weber and R. Scholl, J. Appl. Phys. **74**, 607 (1993).

JETP Letters, Vol. 71, No. 10, 2000, pp. 407–411. Translated from Pis'ma v Zhurnal Éksperimental'noĭ i Teoreticheskoĭ Fiziki, Vol. 71, No. 10, 2000, pp. 593–599.

PLASMA, GASES

Generation of Collimated Beams of Relativistic Ions in Laser–Plasma Interactions

S. V. Bulanov[1], T. Zh. Esirkepov[2], F. Califano[3], Y. Kato[4], T. V. Liseĭkina[5], K. Mima[6], N. M. Naumova[1], K. Nishihara[6], F. Pegoraro[7], H. Ruhl[8], Y. Sentoku[6], and Y. Ueshima[9]

[1]*Institute of General Physics, Russian Academy of Sciences, ul. Vavilova 38, Moscow, 117942 Russia*
e-mail: bulanov@fpl.gpi.ru
[2]*Moscow Institute of Physics and Technology, Institutskiĭ per. 9, Dolgoprudnyĭ, Moscow region, 141700 Russia*
[3]*INFM, Sez. A, 56126 Pisa, Italy*
[4]*APRC JAERI-Kansai, 619-0215 Kizu, Kyoto, Japan*
[5]*Institute of Computational Technologies, Siberian Division, Russian Academy of Sciences, Novosibirsk, 630090 Russia*
[6]*Institute of Laser Engineering, Osaka University, 565-0105 Osaka, Japan*
[7]*University of Pisa and INFM, 56126 Pisa, Italy*
[8]*TQE TH-Darmstadt, 64289 Darmstadt, Germany*
[9]*APRC JAERI-Kansai, Neyagawa, Osaka, 572 Japan*
Received April 10, 2000

A method is proposed for generating collimated beams of fast ions in laser–plasma interactions. Two-dimensional and three-dimensional particle-in-cell simulations show that the ponderomotive force expels electrons from the plasma region irradiated by a laser pulse. The ions with unneutralized electric charge that remain in this region are accelerated by Coulomb repulsive forces. The ions are focused by tailoring the target and also as a result of pinching in the magnetic field produced by the electric current of fast ions. © *2000 MAIK "Nauka/Interperiodica".*

PACS numbers: 52.40.Nk

The study of the mechanisms for ion acceleration in the interaction of high-power laser pulses with matter is very important for further development of the theory of nonlinear plasma dynamics in superstrong electric fields [1] and also for practical applications in controlled fusion research [2, 3] and hadron therapy in oncology [4]. In the experiments on laser–plasma interaction carried out by Krushelnik *et al.* [5], the ions were observed to be accelerated to energies of several tens of megaelectronvolts. In [6, 7], the mechanism for ion acceleration was interpreted as resulting from the so-called "Coulomb explosion." According to those papers, the Coulomb explosion is associated with the break of plasma quasineutrality inside the self-focusing channel. The plasma quasineutrality breaks, because the ponderomotive force and/or the quasistatic magnetic field pressure [7] expel electrons from the channel and the ions are accelerated in the radial direction by the charge-separation electric field. In the nonquasineutral plasma approximation, the energy of fast ions is proportional to the ponderomotive potential; i.e., in the limit $a \gg 1$, it is a linear function of the laser-pulse amplitude $m_e c^2 a$, where $a = eE/m_e\omega c$ is the dimensionless pulse amplitude.

As was pointed out in [8–10], the ion acceleration is more efficient in the field of a petawatt laser pulse, in which case the ion energy is proportional to the squared laser-pulse amplitude $m_e c^2 a^2$. The ions are accelerated preferentially in the propagation direction of the pulse. The intensity of petawatt laser pulses reaches $\approx 10^{22}$ W/cm^2, in which case the inequality $a > (m_i/m_e)^{1/2}$ holds for a hydrogen plasma.

Here, we study the mechanism for generating well-collimated ion beams with energies of several hundred megaelectronvolts in overdense and underdense plasmas.

In order to study ion acceleration in an underdense plasma, we carried out a two-dimensional particle-in-cell (PIC) simulation of the interaction between a short laser pulse and a plasma slab of length 150λ, the ion-to-electron mass ratio being $m_i/m_e = 1840$. We modeled a circularly polarized Gaussian laser pulse of length $l_\parallel = 20\lambda$, width $l_\perp = 10\lambda$, and amplitude $a = 50$, assuming that the plasma density corresponds to the ratio $\omega_{pe}/\omega = 0.45$ of the plasma frequency to the laser frequency.

The results of two-dimensional simulations are illustrated in Figs. 1 and 2. In Figs. 1a and 1b respec-

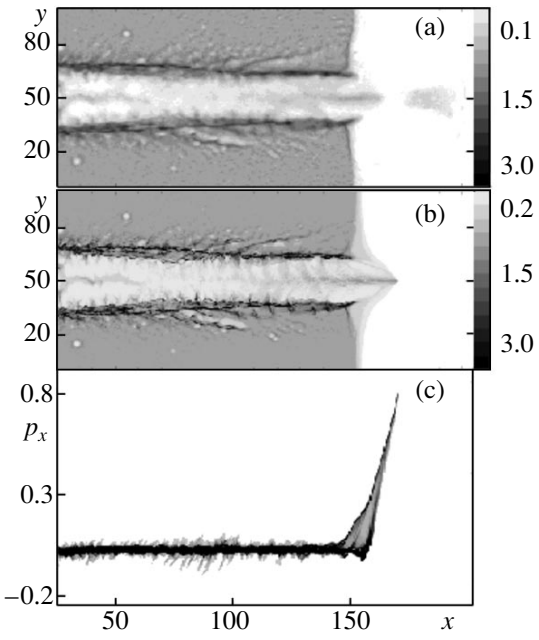

Fig. 1. Distributions of the (a) electron and (b) ion densities in the (x, y) plane and (c) the ion phase plane (p_{xi}, x) at the time $t = 230(2\pi/\omega)$.

tively, we plot the distributions of the electron and ion densities in the (x, y) plane at the time $t = 230(2\pi/\omega)$. By this time, the laser pulse has propagated through the plasma slab and, as is seen from both the electron and ion density distributions, has formed a channel from which the electrons and ions are expelled preferentially in the radial direction. However, the channel is not empty: a dense plasma filament forms on the channel axis. The mechanism for the formation of a plasma filament is associated with the phenomenon of the "inverted corona," which was discussed in [11]. In our problem, the inverted corona arises because, in the interaction with the channel walls, the laser radiation not only expels the plasma from the channel but also effectively heats the plasma and drives a hot plasma flow converging to the channel axis. At later times, the filament is maintained by plasma pinching in a self-consistent quasistatic magnetic field of the electric current flowing inside the channel [12]. At the exit from the channel, the electrons escape from the filament and the ions that remain in the channel and form a cloud with an unneutralized electric charge expand preferentially in the longitudinal direction. As a result, the ions acquire a kinetic energy corresponding to the electrostatic potential of the filament. From Fig. 1c, which displays the ion phase plane (p_{xi}, x), we can see that the maximum momentum acquired by the ions is $p_x = 0.8m_ic$.

At the exit from the channel, the ions form a collimated high-density beam. Figure 2 shows the electron (dashed curve) and ion (dashed-and-dotted curve) densities and the z-component of the magnetic field (solid curve) as functions of the y-coordinate at $x = 155.5$ (Fig. 2a) and $x = 168.5$ (Fig. 2b). From Fig. 2a, we can see that, in the region immediately at the exit from the channel (at $x = 155.5$), the filament plasma is quasineutral, because the electron and ion densities are the same. The plasma density inside the filament is higher than the initial plasma density by a factor of 6. The y-profile of the magnetic field, which is seen to vanish at the channel axis, implies that the electric current in the plasma is carried by the electrons (the magnetic field gradient is negative). In the region where fast ions are concentrated (at $x = 168.5$ in Fig. 2b), the profiles of the electron and ion densities and magnetic field are radically different: the ion density exceeds the electron density by a factor of 10. Nevertheless, a high-density ion beam remains strongly localized: the beam radius is as small as several microns. This effect is attributed to the pinching of ions in the magnetic field of the ion electric current. That the magnetic field in the vicinity of the beam axis is produced by the ion current is clear from Fig. 2b, in which the magnetic field gradient is seen to be positive.

Ion acceleration in the interaction between a laser pulse and a thin dense plasma slab (a foil) of overcritical density was discussed by Esirkepov *et al.* [9]. They also explained the mechanism for ion acceleration in

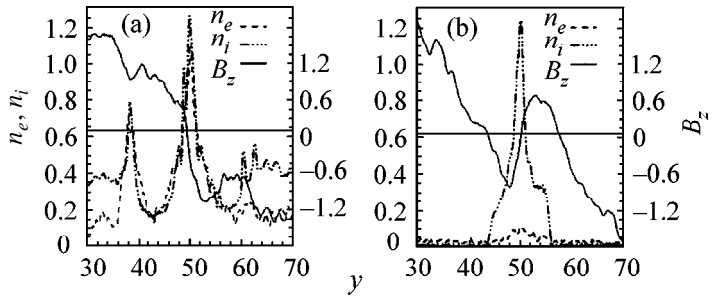

Fig. 2. The y-profiles of the electron (dashed curve) and ion (dashed-and-dotted curve) densities and of the z-component of the magnetic field (solid curve) at x = (a) 155.5 and (b) 168.5.

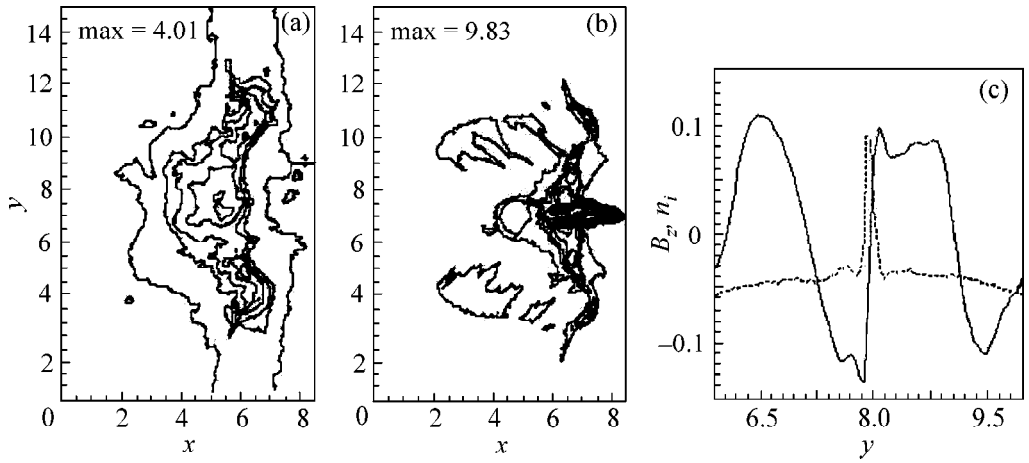

Fig. 3. Distributions of the (a) electron and (b) ion densities in the (x, y) plane and (c) profiles of the ion energy density (dashed curve) and of the quasistatic magnetic field (solid curve) inside the ion beam (c) at the time $t = 15(2\pi/\omega)$.

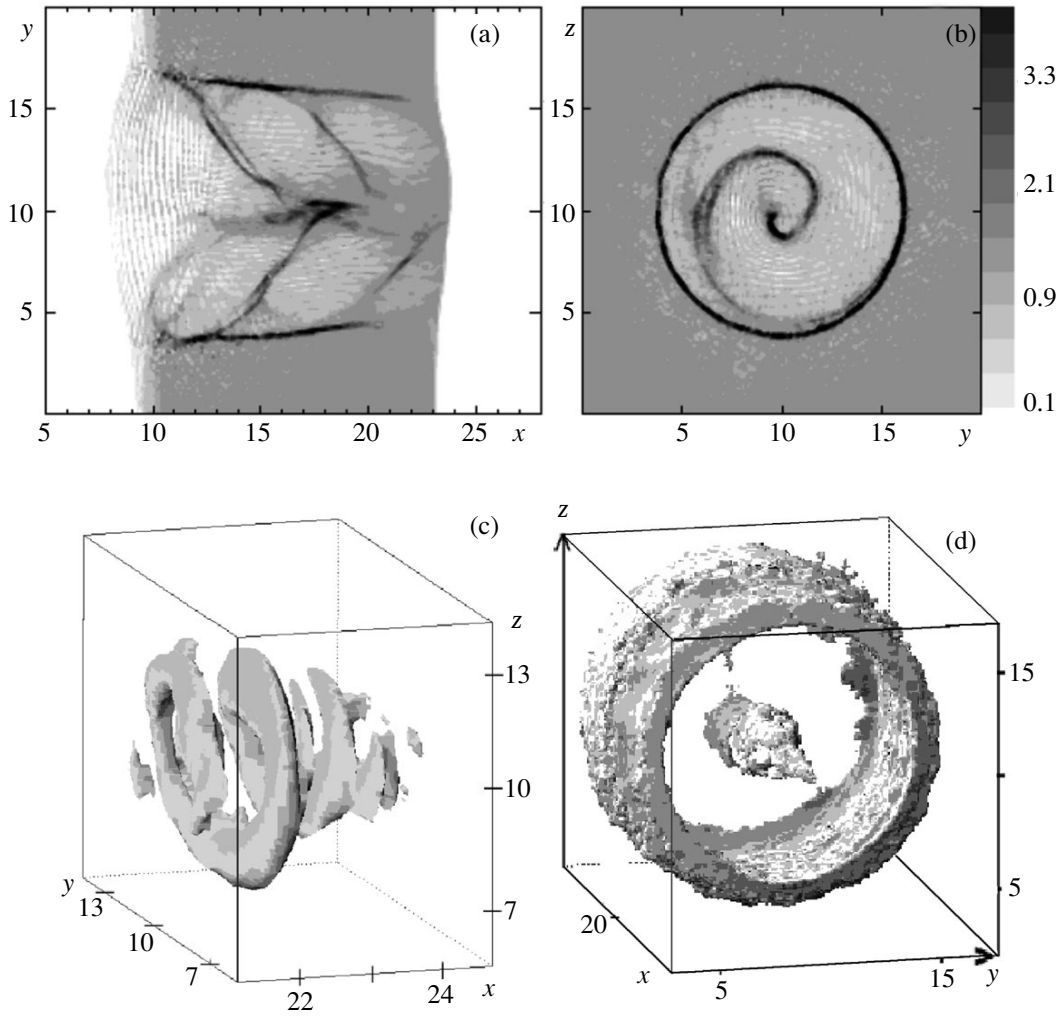

Fig. 4. Ion density distributions (a) in the (x, y) plane at $z = 0$ and (b) in the (y, z) plane at $x = 15\lambda$, (c) the isosurface $\sqrt{(E^2 + B^2)/2} = 40$, and (d) the fast ion beam at the channel axis (the isosurface $n_i = 1.8$).

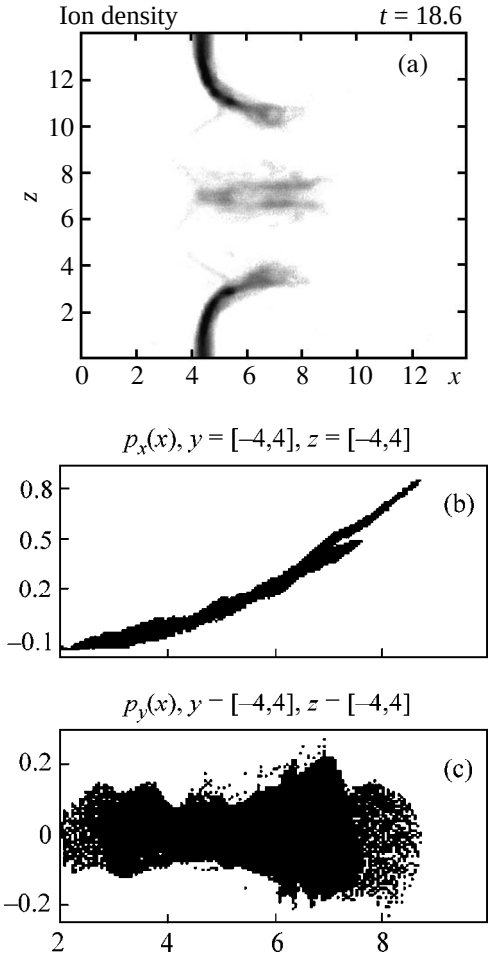

Fig. 5. (a) Fast ion beam at the axis, (b) the phase plane (p_{xi}, x), and (c) the phase plane ($p_\perp$, x).

terms of the Coulomb explosion of an irradiated foil site, from which the electrons are expelled by the ponderomotive pressure of laser light. They demonstrated that the expansion of a cloud of accelerated ions is accompanied by the onset of an electromagnetic instability, which gives rise to filamentation. Here, we propose to intensify the tendency toward filamentation by using a target tailored in the desired fashion. Specifically, we model the following situation: A dense plasma slab with a thickness of 2λ initially occupies the region $5\lambda < x < 7\lambda$; the central part of the slab is parabolic in shape and is convex toward the incident laser light. The plasma density inside the slab is $n = 30n_{cr}$, and the ion-to-electron mass ratio is 1840. A laser pulse with the amplitude $a = 89$ is p-polarized.

The tailoring of the target foil makes ion acceleration more efficient and leads to enhanced focusing of both the penetrating laser radiation and the plasma flows expanding in the propagation direction of the laser pulse. Note that the focusing of plasma flows in the interaction between a moderate-power laser pulse and a semicylindrical foil was studied by Askar'yan *et al.* [13].

We assume that a laser pulse propagates along the x-axis and is Gaussian in shape in both the transverse and longitudinal directions, the pulse length and width being 5.5λ and $R = 5\lambda$, respectively. With the parameters adopted here, the plasma slab is opaque to laser radiation. In the course of interaction between the pulse and the target, the electrons are expelled from the plasma slab, thereby giving rise to a strong charge-separation electric field. The energy of fast electrons can be as high as 200 MeV, and the ions are accelerated mainly in the propagation direction of the pulse. Fast ions moving along the x-axis form a thin dense filament. In Figs. 3a and 3b, respectively, we plot the electron and ion density distributions in the (x, y) plane at the time $t = 15(2\pi/\omega)$. A thin ion beam is clearly seen in Fig. 3b. Figure 3c shows y-profiles of the ion energy density (dashed curve) and of the quasistatic magnetic field (solid curve) inside the ion beam for $x = 4.65$ at the time $t = 12(2\pi/\omega)$. We can see that the magnetic field is produced by the ion electric current. The peak momentum of the fast ions equals $p_{xi}/m_ic \sim 1$. In this case, the acceleration mechanism can also be explained in terms of the Coulomb explosion, and the quasistatic magnetic field lowers the rate at which the beam expands in the radial direction. The thickness of the ion beam is equal to 0.2λ; and the beam density, which substantially exceeds the local electron density, is as high as 10^{22} cm^{-3}.

The two-dimensional simulation presented above gives a qualitatively correct description of ion acceleration but overestimates the energy of fast particles, because, in the two-dimensional approximation, the Coulomb potential of the charged cloud diverges logarithmically at large distances. For this reason, we carried out three-dimensional simulations of the interaction of a laser pulse with both underdense and overdense plasmas. The results of a three-dimensional numerical analysis of ion acceleration by the PIC method are illustrated in Figs. 4 and 5.

In the case of an underdense plasma, a circularly polarized laser pulse of length 20λ, diameter $R = 10\lambda$, and amplitude $a = 50$ interacts with a plasma slab with a length of 15λ and a density corresponding to $\omega_{pe}/\omega = 0.45$. The formation of an ion channel with a dense filament at the axis is illustrated in Figs. 4a and 4b, which show the cross section $z = 0$ in the (x, y) plane and the cross section $x = 15\lambda$ in the (y, z) plane, respectively, at the time $t = 30$ $(2\pi/\omega)$ A circularly polarized pulse scrapes off a thin plasma layer from the channel walls. When scraped off, the plasma layer inside the channel becomes spiral-shaped. Such a modulation of the plasma density results in a nonlinear modulation of the laser pulse: the pulse also assumes the shape of a spiral (Fig. 4c). In the three-dimensional case, the density of fast ions inside the beam is higher (Fig. 4d) and their energy is lower than those in the two-dimensional case.

According to the three-dimensional analysis, the momentum of fast ions is equal to $p_{xi} = 0.61 m_i c$.

The results of three-dimensional simulations of the interaction between a linearly polarized laser pulse and a tailored target (a paraboloid of revolution) are illustrated in Fig. 5 for a plasma density of $n = 25 n_{cr}$ and a slab thickness of 0.5λ and for a semiinfinite pulse with a waist diameter of 5λ and an amplitude of $a = 25$. Laser radiation causes the formation of a thin ion beam at the channel axis (Fig. 5a). From Figs. 5b and 5c, we can see that the longitudinal component of the ion momentum $p_{xi} = 0.8 m_i c$ is significantly higher than the transverse momentum component $p_\perp = 0.2 m_i c$.

We conclude that a petawatt laser pulse interacting with a plasma generates thin collimated beams of fast ions with energies of several hundred megaelectronvolts and a relatively small divergence. The number of ions accelerated per pulse is about 10^{12}.

REFERENCES

1. G. A. Mourou, C. P. J. Barty, and M. D. Perry, Phys. Today **51**, 22 (1998).
2. M. Tabak, J. Hammer, M. E. Glinsky, *et al.*, Phys. Plasmas **1**, 1626 (1994).
3. A. P. Fews, P. A. Norreys, F. N. Beg, *et al.*, Phys. Rev. Lett. **73**, 1801 (1994).
4. V. S. Khoroshkov and E. I. Minakova, Eur. J. Phys. **19**, 523 (1998).
5. K. Krushelnik, E. L. Clark, M. Zepf, *et al.*, Phys. Plasmas **7**, 2055 (2000).
6. G. S. Sarkisov, V. Yu. Bychenkov, V. N. Novikov, *et al.*, Phys. Rev. E **59**, 7042 (1999).
7. A. V. Gordeev and T. V. Loseva, Pis'ma Zh. Éksp. Teor. Fiz. **70**, 669 (1999) [JETP Lett. **70**, 684 (1999)].
8. S. V. Bulanov, I. A. Vshivkov, G. I. Dudnikova, *et al.*, Fiz. Plazmy **25**, 748 (1999) [Plasma Phys. Rep. **25**, 701 (1999)].
9. T. Zh. Esirkepov, Y. Sentoku, K. Mima, *et al.*, Pis'ma Zh. Éksp. Teor. Fiz. **70**, 80 (1999) [JETP Lett. **70**, 82 (1999)].
10. F. Pegoraro, S. V. Bulanov, F. Califano, *et al.*, IEEE Trans. Plasma Sci. (in press).
11. G. A. Askar'yan, S. V. Bulanov, and I. V. Sokolov, Fiz. Plazmy **25**, 603 (1999) [Plasma Phys. Rep. **25**, 549 (1999)].
12. G. A. Askar'yan, S. V. Bulanov, F. Pegoraro, and A. M. Pukhov, Pis'ma Zh. Éksp. Teor. Fiz. **60**, 240 (1994) [JETP Lett. **60**, 251 (1994)].
13. G. A. Askar'yan, M. G. Korolev, and L. L. Yakushkin, Pis'ma Zh. Éksp. Teor. Fiz. **57**, 164 (1993) [JETP Lett. **57**, 167 (1993)].

Translated by O. Khadin

JETP Letters, Vol. 71, No. 10, 2000, pp. 412–416. From Pis'ma v Zhurnal Éksperimental'noĭ i Teoreticheskoĭ Fiziki, Vol. 71, No. 10, 2000, pp. 600–605.

CONDENSED MATTER

Critical Exponents for a Three-Dimensional Impure Ising Model in the Five-Loop Approximation[1]

D. V. Pakhnin and A. I. Sokolov

St. Petersburg Electrotechnical University, St. Petersburg, 197376 Russia

e-mail: ais@sokol.usr.etu.spb.ru

Received April 4, 2000

The renormalization-group functions governing the critical behavior of the three-dimensional weakly-disordered Ising model are calculated in the five-loop approximation. The random fixed point location and critical exponents for impure Ising systems are estimated by means of the Padé–Borel–Leroy resummation of the renormalization-group expansions derived. The asymptotic critical exponents are found to be $\gamma = 1.325 \pm 0.003$, $\eta = 0.025 \pm 0.01$, $\nu = 0.671 \pm 0.005$, $\alpha = -0.0125 \pm 0.008$, $\beta = 0.344 \pm 0.006$, while for the correction-to-scaling exponent, a less accurate estimate $\omega = 0.32 \pm 0.06$ is obtained. *© 2000 MAIK "Nauka/Interperiodica".*

PACS numbers: 75.10.Hk; 75.40.Cx; 05.50.+q; 05.70.Jk

Today, two regular field-theoretical methods exist to evaluate the universal critical quantities of uniaxial impure magnets described by the three-dimensional (3D) random Ising model: the $\sqrt{\epsilon}$-expansion invented by Harris and Lubensky [1, 2] and Khmelnitskiĭ [3] and the renormalization-group (RG) approach in three dimensions. The former technique, being well developed [4, 5], was recently shown to have limited numerical power, since $\sqrt{\epsilon}$-expansions for critical exponents, calculated starting from the five-loop series [6] up to the $\sqrt{\epsilon}^4$ and $\sqrt{\epsilon}^5$ terms [7], exhibit an irregular structure making them unsuitable for subsequent resummation and extracting numerical estimates [8].

On the contrary, the field-theoretical RG approach in three dimensions proved to be very effective when used to estimate the critical exponents and other universal characteristics of the $O(n)$-symmetric systems [9–19]. The weakly disordered Ising model at criticality is known to be described by the n-vector φ^4 field theory with the quartic self-interaction having a hypercubic symmetry, provided $n \longrightarrow 0$ (the replica limit) and the coupling constants have proper signs. In the 1980s, the RG expansions for 3D cubic and impure Ising models were calculated in the two-loop [20], three-loop [21, 22], and four-loop [23, 24] approximations, paving the way for estimating the universal critical quantities [20–33]. The four-loop 3D RG expansions, however, resummed by the generalized Padé–Borel–Leroy method, do not allow one to optimize the resummation procedure, since there is the only approximant ([3/1]) that does not suffer from positive axis poles. Moreover, accounting for the four-loop terms in the 3D RG series shifts the random fixed point coordinates and the correction-to-scaling exponent ω appreciably with respect to the three-loop estimates, indicating that at this step the RG based iterations still do not achieve their asymptote.

In such a situation a calculation of the higher order contributions to the RG functions looks very desirable. In this Letter, the five-loop RG expansions for the 3D impure Ising model are obtained and the numerical estimates for the critical exponents are found.

We start from the Landau–Wilson Hamiltonian of the 3D n-vector cubic model:

$$H = \frac{1}{2}\int d^3x\left[m_0^2\varphi_\alpha^2 + (\nabla\varphi_a)^2 + \frac{u_0}{12}\varphi_\alpha^2\varphi_\beta^2 + \frac{v_0}{12}\varphi_\alpha^4\right], \quad (1)$$

where φ is an n-component real order parameter, m_0^2 being the reduced deviation from the mean-field transition temperature. In the replica limit, this Hamiltonian describes the impure Ising model provided $u_0 < 0$ and $v_0 > 0$.

The RG functions for the Hamiltonian (1) are found within a massive theory. To extend known four-loop RG series [23, 24] to the five-loop order, we calculate the tensor (field) factors generated by the cubic interaction. Taking then the values of 3D integrals from [34], we arrive, under $n = 0$, at the following expansions:

$$\frac{\beta_u}{u} = 1 - 8u - 6v + \frac{4(190u^2 + 300uv + 69v^2)}{27}$$
$$- 199.64042u^3 - 493.84155u^2v - 302.86779uv^2$$
$$- 65.937285v^3 + 1832.2067u^4 + 6192.5121u^3v$$
$$+ 6331.2264u^2v^2 + 2777.3942uv^3 + 495.00575v^4 \quad (2)$$

[1] This article was submitted by the authors in English.

$$- 20770.177u^5 - 89807.670u^4v - 130340.91u^3v^2$$
$$- 90437.636u^2v^3 - 33088.223uv^4 - 5166.3920v^5,$$

$$\frac{\beta_v}{v} = 1 - 12u - 9v + \frac{4(370u^2 + 624uv + 231v^2)}{27}$$
$$- 469.33397u^3 - 1228.6059u^2v - 957.78166uv^2$$
$$- 255.92974v^3 + 5032.6923u^4 + 17967.851u^3v$$
$$+ 21964.394u^2v^2 + 11856.957uv^3 + 2470.3925v^4 \quad (3)$$
$$- 64749.282u^5 - 294450.70u^4v - 493917.04u^3v^2$$
$$- 407119.31u^2v^3 - 170403.12uv^4 - 29261.585v^5.$$

$$\gamma^{-1} = 1 - u - \frac{3v}{2} + 2u^2 + 6uv + 3v^2 - 9.4527182u^3$$
$$- 42.537232u^2v - 49.298206uv^2 - 16.817754v^3$$
$$+ 70.794806u^4 + 424.76884u^3v + 752.04939u^2v^2$$
$$+ 516.26675uv^3 + 130.47743v^4 - 675.69961u^5 \quad (4)$$
$$- 5067.7471u^4v - 12193.045u^3v^2$$
$$- 12966.212u^2v^3 - 6587.8339uv^4 - 1326.2123v^5.$$

$$\eta = \frac{8(2u^2 + 6uv + 3v^2)}{27} + 0.39494402u^3$$
$$+ 1.7772481u^2v + 1.9994041uv^2 + 0.66646804v^3$$
$$+ 6.5121099u^4 + 39.072660u^3v + 68.665263u^2v^2$$
$$+ 47.140073uv^3 + 11.785018v^4 - 21.647206u^5 \quad (5)$$
$$- 162.35405u^4v - 382.02381u^3v^2$$
$$- 389.99671u^2v^3 - 193.00269uv^4 - 38.600539v^5.$$

The five-loop RG series for generic n are presented in [35].

Numerical values of critical exponents are determined by the coordinates of the random fixed point. To find its location, the Padé–Borel–Leroy resummation technique is applied, which demonstrated high effectiveness both for $O(n)$-symmetric models [9, 11, 15] and for anisotropic systems preserving their internal symmetries (see, e.g., [36]). Since the RG functions depend on two variables, the Borel–Leroy transformation is taken in a generalized form:

$$f(u, v) = \sum_{ij} c_{ij} u^i v^j = \int_0^\infty e^{-t} t^b F(ut, vt)\,dt,$$
$$F(x, y) = \sum_{ij} \frac{c_{ij} x^i y^j}{(i + j + b)!}. \quad (6)$$

To perform an analytical continuation, the resolvent series

$$\tilde{F}(x, y, \lambda) = \sum_{n=0}^{\infty} \lambda^n \sum_{l=0}^{n} \frac{c_{l,n-l} x^l y^{n-l}}{n!} \quad (7)$$

is constructed with coefficients that are uniform polynomials in u, v and then Padé approximants $[L/M]$ in λ at $\lambda = 1$ are used.

For the resummation of the five-loop RG expansions, we employ three different Padé approximants: [4/1], [3/2], and [2/3]. The first of them, being pole-free, is known to give good numerical results for basic 3D models of phase transitions, while the others are near-diagonal and should reveal, in general, the best approximating properties. The coordinates of the random fixed point resulting from the series (2) and (3) under $b = 0$ and $b = 1$ are presented in Table 1, where superscript "p" stands to mark that the Padé approximant has a "nondangerous" positive axis pole.

Table 1, where the widely accepted variables $U = 8u$ and $V = 8v$ are used instead of u and v, also contains the four-loop estimates. The four-loop series were processed on the base of the Padé approximant [3/1], since use of the diagonal approximant [2/2] leads to an integrand in Eq. (6) that has a dangerous pole near the random fixed point both for β_u and β_v.[2] The fixed point location given by the approximant [2/3] is presented for $b = 0$ only, because for $b = 1$ this approximation predicts no random fixed point.

As is seen from Table 1, Padé approximants [4/1] and [3/2] yield numerical values of U_c and V_c which are very close to each other. Moreover, for $b = 0$ they are also close to those given by the approximant [3/1]: the largest difference between the five-loop and four-loop estimates does not exceed 0.03. With increasing b, corresponding numbers diverge, indicating that $b = 0$ is an optimal value of the shift parameter. On the contrary, Padé approximant [2/3] gives a random fixed point location which deviates appreciably from those predicted by approximants [4/1], [3/2], and [3/1]. This approximant, however, leads to poor numerical results even for simpler systems. Indeed, when used to evaluate the coordinate of the Ising fixed point, it results in $V_c = 1.475$ (under $b = 0$), while the best estimate today

[2] In fact, under $b = 1$ the approximant [3/2] generates the expression for β_v that is also spoiled by a positive axis pole at the random fixed point. This pole, however, being well removed from the origin ($t = 40.12$), turns out not to be dangerous; i.e., it does not influence, in practice, the evaluation of the Borel integral.

Table 1

	b	[4/1]	[3/2]	[2/3]	[3/1]
U_c	0	−0.7200	−0.7148	−0.6871	−0.6991
	1	−0.7445	−0.7385[p]		−0.6839
V_c	0	2.0182	2.0125	2.0571	1.9922
	1	2.0296	2.0236[p]		1.9877
ω	0	0.266	0.303	0.462[c]	0.376
	1	0.263	0.325[p]		0.361

Table 2

b		0	1	2	3	5	10	15
$(\gamma^{-1})^{-1}$	[4/1]	1.3236	1.3244	1.3250	1.3254	1.3260	1.3268	1.3272
	[3/2]	–	–	–	1.3253[p]	1.3260	1.3265	1.3267
γ	[4/1]	1.3245	1.3248	1.3250	1.3252	1.3254	1.3257	1.3259
	[3/2]	1.3246[p]	1.3251[p]	1.3254[p]	1.3257[p]	1.3261[p]	1.3267[p]	1.3270[p]
η	[4/1]	0.0312	0.0276	0.0251	0.0231	0.0204	0.0166	0.0148
(via η_2)	[3/2]	–	–	–	0.0287[p]	0.0217[p]	0.0167[p]	0.0149

is $V_c = 1.411$ [14]. This forces us to reject the data given by the approximant [2/3].

To finally determine the coordinates U_c and V_c, we average the numerical data given by three working Padé approximants at $b = 0$. This procedure yields the values

$$U_c = -0.71, \quad V_c = 2.01, \tag{8}$$

which are claimed to be the results of our search of the random fixed point location. To estimate their apparent accuracy, we accept that deviations of these numbers from the exact ones will not exceed the differences between them and the four-loop results, since, among all proper estimates, the four-loop ones most strongly differ from the averaged values. Hence, the error bounds for U_c and V_c are believed to be no greater than ±0.02. Another way to estimate the apparent accuracy is to trace how the averaged values of the random fixed point coordinates vary with the variation of b. We calculate U_c and V_c using the pole-free approximants [4/1] and [3/1] for b lying between 0 and 15. Running through this interval, the averaged coordinates change their values by about 0.02, indicating that an accuracy of the estimates found is of the order of a few per cent.

Let us evaluate further the critical exponents. The exponent γ is estimated by the Padé–Borel–Leroy summation of the series (4) for γ^{-1} and of the analogous RG expansion for γ, with approximants [4/1] and [3/2] being employed. The numerical value of the Fisher exponent is also found in two different ways: via the estimation of the critical exponent $\eta_2 = (2 - \eta)(\gamma^{-1} - 1)$ having the RG expansion which exhibits a good summability and by direct substitution of the fixed point coordinates into the series (5) with rapidly diminishing coefficients. Direct summation of the RG expansion for η gives $\eta = 0.027$; numerical results obtained by making use of the resummation procedures just described are collected in Table 2.

In this table, symbol $(\gamma^{-1})^{-1}$ means that the RG series for γ^{-1} was resummed. The empty cells are due to the dangerous poles spoiling corresponding approximations. The estimates for η standing in the 5th and 6th lines were obtained under $\gamma = 1.325$ by the resummation of the RG series for η_2.

As is seen, two methods of evaluating γ lead to remarkably close numerical results which very weakly depend on the tune parameter. Indeed, with increasing b from 0 to 15, the estimates for γ obtained by the resummation of the RG series for γ and γ^{-1} on the base of the pole-free approximant [4/1] vary by less than 0.0036, while the difference between them never exceeds 0.0013. Under the same variation of b, the value of γ averaged over these two most reliable approximations remains within the segment [1.3240, 1.3266]. On the other hand, the accuracy of determination of the critical exponents depends not only on the quality of the resummation procedure but also on the accuracy achieved in the course of locating of the random fixed point. That is why we investigated to what extent the estimates for γ vary when the coordinates of the random fixed point run through their error bars. It was found that γ calculated at the optimal value of tune parameter $b = 2$ (see Table 2) does not leave the segment [1.3228, 1.3263]. Hence, the error bounds for the value of γ are believed to be about ±0.003.

Less stable numerical results are found for the Fisher exponent η. As is seen from Table 2, the values of η given by the RG series for η_2 and the pole-free Padé approximant [4/1] spread from 0.0148 to 0.0312. The average over this interval is equal to 0.023, while the direct summation of the series (5) gives 0.027. Hence, 0.025 should play the role of the most likely value of exponent η. Since the estimates for η found via the evaluation of η_2 are sensitive to the accepted value of γ, the apparent accuracy achieved in this case is not believed to be better than ± 0.01.

Having estimated γ and η, we evaluate other critical exponents using well-known scaling relations. The final results of our five-loop RG analysis are as follows:

$$\gamma = 1.325 \pm 0.003, \quad \eta = 0.025 \pm 0.01,$$
$$\nu = 0.671 \pm 0.005, \qquad (9)$$
$$\alpha = -0.0125 \pm 0.008, \quad \beta = 0.344 \pm 0.006.$$

It is interesting to compare these numbers with those obtained earlier within the lower order RG approximations. For the exponent γ previous 3D RG calculations gave the values 1.337 [20, 25] (two-loop), 1.328 [22] (three-loop), 1.326 [23] (four-loop), and 1.321 [24] (four-loop). Being found by means of different resummation procedures, they are, nevertheless, centered around our estimate, which is thus argued to be close to the exact value of γ or, more precisely, to the true asymptote of the RG iterations.

In conclusion, we evaluate the correction-to-scaling exponent ω. This exponent is known to be equal to the eigenvalue of the stability matrix

$$\begin{pmatrix} \frac{\partial \beta_u}{\partial u} & \frac{\partial \beta_u}{\partial v} \\ \frac{\partial \beta_v}{\partial u} & \frac{\partial \beta_v}{\partial v} \end{pmatrix} \qquad (10)$$

that has a minimal modulus. The derivatives entering this matrix are evaluated numerically at the random fixed point on the base of the resummed RG expansions for β_u and β_v and then the matrix eigenvalues are found. Such a procedure leads to the estimates for ω presented in Table 1 (lower lines); the superscript "*c*" denotes that ω is complex within the corresponding approximation and its real part is presented. The numerical values obtained are seen to be considerably scattered and sensitive to the tune parameter. The average over three working Padé approximants, however, being equal to 0.315 at $b = 0$ and to 0.316 at $b = 1$, turns out to be stable under the variation of b unless b becomes large. It is natural, therefore, to accept that

$$\omega = 0.32 \pm 0.06. \qquad (11)$$

This number is smaller by 0.05–0.07 than its counterparts given by recent Monte Carlo simulations [37] and the alternative RG analysis [32], but their central values lie within the declared error bounds (11). Hence, an agreement between the results discussed exists. On the other hand, the estimate just found needs to be refined, along with the estimates for η and α also exhibiting appreciable uncertainties. Hopefully, a proper processing of the six-loop expansions obtained very recently [38] would enable one to further improve the accuracy of the predictions given by the field-theoretical RG approach.

This work was supported by the Ministry of Education of the Russian Federation, grant no. 97-14.2-16. One of the authors (A.I.S.) gratefully acknowledges the support of the International Science Foundation, grant no. p99-943.

REFERENCES

1. A. B. Harris and T. C. Lubensky, Phys. Rev. Lett. **33**, 1540 (1974).
2. T. C. Lubensky, Phys. Rev. B **11**, 3573 (1975).
3. D. E. Khmelnitskiĭ, Zh. Éksp. Teor. Fiz. **68**, 1960 (1975) [Sov. Phys. JETP **41**, 981 (1975)].
4. B. N. Shalaev, Zh. Éksp. Teor. Fiz. **73**, 2301 (1977) [Sov. Phys. JETP **46,** 1204 (1977)].
5. C. Jayaprakash and H. J. Katz, Phys. Rev. B **16**, 3987 (1977).
6. H. Kleinert and V. Schulte-Frohlinde, Phys. Lett. B **342**, 284 (1995).
7. B. N. Shalaev, S. A. Antonenko, and A. I. Sokolov, Phys. Lett. A **230**, 105 (1997).
8. R. Folk, Yu. Holovatch, and T. Yavors'kiĭ, J. Phys. Stud. (Ukr.) **2**, 213 (1998); cond-mat/9909121.
9. G. A. Baker, Jr., B. G. Nickel, and D. I. Meiron, Phys. Rev. B **17**, 1365 (1978).
10. J. C. Le Guillou and J. Zinn-Justin, Phys. Rev. B **21**, 3976 (1980).
11. S. A. Antonenko and A. I. Sokolov, Phys. Rev. E **51**, 1894 (1995).
12. C. Gutsfeld, J. Kuester, and G. Muenster, Nucl. Phys. B **479**, 654 (1996).
13. R. Guida and J. Zinn-Justin, Nucl. Phys. B **489**, 626 (1997).
14. R. Guida and J. Zinn-Justin, J. Phys. A **31**, 8103 (1998).
15. A. I. Sokolov, Fiz. Tverd. Tela (St. Petersburg) **40**, 1284 (1998) [Phys. Solid State **40**, 1169 (1998)].
16. H. Kleinert, Phys. Rev. D **57**, 2264 (1998).
17. H. Kleinert, Phys. Rev. D **60**, 085001 (1999).
18. A. I. Sokolov, E. V. Orlov, V. A. Ul'kov, and S. S. Kashtanov, Phys. Rev. E **60**, 1344 (1999).
19. M. Stroesser, S. A. Larin, and V. Dohm, Nucl. Phys. B **540**, 654 (1999).
20. G. Jug, Phys. Rev. B **27**, 609 (1983).
21. A. I. Sokolov and B. N. Shalaev, Fiz. Tverd. Tela (Leningrad) **23**, 2058 (1981) [Sov. Phys. Solid State **23**, 1200 (1981)].
22. N. A. Shpot, Phys. Lett. A **142**, 474 (1989).
23. I. O. Mayer, A. I. Sokolov, and B. N. Shalaev, Ferroelectrics **95**, 93 (1989).

24. I. O. Mayer, J. Phys. A **22**, 2815 (1989).
25. I. O. Maier and A. I. Sokolov, Fiz. Tverd. Tela (Leningrad) **26**, 3454 (1984) [Sov. Phys. Solid State **26**, 2076 (1984)].
26. I. O. Maier and A. I. Sokolov, Izv. Akad. Nauk SSSR, Ser. Fiz. **51**, 2103 (1987); I. O. Maier and A. I. Sokolov, Ferroelectr. Lett. Sect. **9**, 95 (1988).
27. N. A. Shpot, Zh. Éksp. Teor. Fiz. **98**, 1762 (1990) [Sov. Phys. JETP **71**, 989 (1990)].
28. C. Bervillier and M. Shpot, Phys. Rev. B **46**, 955 (1992).
29. H. Kleinert and S. Thoms, Phys. Rev. D **52**, 5926 (1995).
30. H. Kleinert, S. Thoms, and V. Schulte-Frohlinde, Phys. Rev. B **56**, 14428 (1997).
31. I. Mayer, Physica A (Amsterdam) **252**, 450 (1998).
32. R. Folk, Yu. Holovatch, and T. Yavors'kii, Pis'ma Zh. Éksp. Teor. Fiz. **69**, 698 (1999) [JETP Lett. **69**, 747 (1999)].
33. K. B. Varnashev, cond-mat/9909087.
34. B. G. Nickel, D. I. Meiron, and G. A. Baker, Jr., *Compilation of 2-pt and 4-pt Graphs for Continuous Spin Model* (Univ. of Guelph Report, 1977).
35. D. V. Pakhnin and A. I. Sokolov, cond-mat/9912071.
36. S. A. Antonenko and A. I. Sokolov, Phys. Rev. B **49**, 15901 (1994).
37. H. G. Ballesteros, L. A. Fernández, V. Martín-Mayor, *et al.*, Phys. Rev. B **58**, 2740 (1998).
38. J. M. Carmona, A. Pelissetto, and E. Vicari, cond-mat/9912115.

JETP Letters, Vol. 71, No. 10, 2000, pp. 417–421. Translated from Pis'ma v Zhurnal Éksperimental'noĭ i Teoreticheskoĭ Fiziki, Vol. 71, No. 10, 2000, pp. 606–611.

CONDENSED MATTER

Incompressible Electron Phase in Field-Effect Transistors

S. I. Dorozhkin and M. O. Dorokhova

Institute of Solid-State Physics, Russian Academy of Sciences, Chernogolovka, Moscow region, 142432 Russia

e-mail: dorozh@issp.ac.ru

Received April 5, 2000; in final form, April 10, 2000

The formation of regions of compressible and incompressible phases in the quantum Hall effect regime has been considered for a two-dimensional (2D) electron system that is created in a field-effect transistor. This effect arises from long-period fluctuations of the density of ionized donors supplying electrons to the 2D system. It is shown that the motion of these regions caused by variations of the average electron density gives rise to minima in the capacitance of the capacitor formed by the 2D electron system and the transistor gate. When the corrections to the capacitance are small, the shape of the minima reproduces the donor density distribution function. Experimental data are presented that demonstrate good agreement with the predictions of the model.

PACS numbers: 73.40.Hm; 85.30.Tv

The occurrence of a discrete energy spectrum with a high degree of Landau level degeneracy in two-dimensional (2D) electron systems in quantizing magnetic fields results in a nontrivial behavior of screening properties of such systems. Namely, within the Thomas–Fermi approximation, the system perfectly screens the random potential when one of the Landau levels is only partially filled and does not screen it at all in the case of fully filled levels. Conventionally, the corresponding states are referred to as compressible and incompressible, respectively. Given a long-period (as compared to the magnetic length) random nucleation potential of sufficiently large amplitude, this property of a 2D electron system must lead [1] to its separation into alternate regions of the compressible and incompressible phases. The widths of the corresponding strips of different phases were calculated in [2], provided that the potential is regular, the 2D electron density monotonically varies near the edge of the sample, and the sample is homogeneous along the other direction (see also [3–8]). In this case, a strip of the incompressible phase separates the regions in which successive Landau levels are partially filled. A voltage difference arises across the strip, which is compensated for by a chemical potential jump equal to the distance between the levels. In samples with a metal electrode (gate) parallel to the 2D electron system, the width of these strips must undergo a change when the distance between the 2D system and the gate becomes smaller than, or comparable with, the width of the incompressible strips [7]. In this paper, we will describe the formation of regions of the incompressible phase in samples with a gate and a smoothly varying density of donors supplying electrons to the 2D system in real semiconductors. Our approach is based on the capacitor approximation that was previously used in [9] to describe a nonequilibrium state with a current flowing through the 2D system. The approximation employed can be simply generalized to the case when the chemical potential of 2D electrons is described by a more complicated function of electron density that differs from the corresponding dependence for noninteracting electrons at zero temperature, which was suggested in [2–7]. In particular, our model is easily adapted to the consideration of nonuniform states in the case of the fractional quantum Hall effect. In addition, we will describe effects associated with the motion of incompressible regions over a sample upon variation of the gate voltage.

Consider the structure described in the inset in Fig. 1. Assume that the 2D electron system is created by means of size quantization in a narrow potential well whose shape does not depend on the electric field in the structure. Equating the change in the free energy of the system of charges in the structure to the work done by a source of direct-current voltage to separate the charges, we obtain the following relationship:

$$\frac{4\pi e^2 n_s d}{\kappa} - \frac{4\pi e^2 n_d d_1}{\kappa} + \epsilon_0 + \mu - \mu_g = eV_g. \qquad (1)$$

Here, n_s and n_d are the surface densities of electrons and ionized donors, respectively; ϵ_0 is the position of the two-dimensional subband bottom, from which the chemical potential μ of the 2D electron system is measured; μ_g is the chemical potential of the gate electron system; κ is the dielectric constant; and V_g is the voltage applied across the gate and the 2D system. In a quantizing magnetic field H at zero temperature and in the absence of correlation effects, the dependence of the chemical potential μ on n_s is described by a step

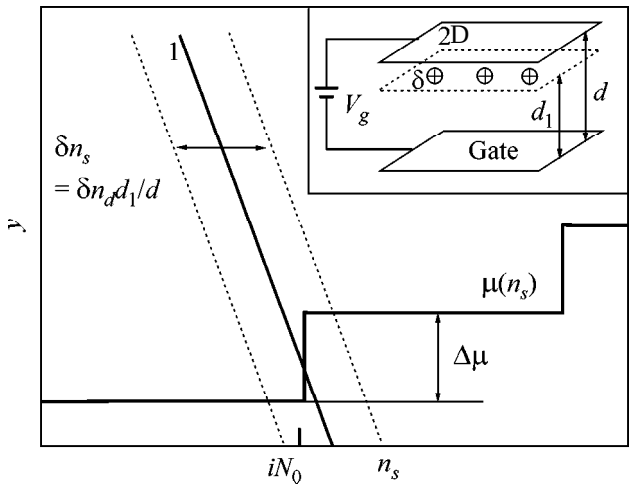

Fig. 1. Schematic diagram demonstrating the behavior of solutions of Eq. (1) for a step dependence of the chemical potential μ on the electron density n_s. The inset shows a circuit of a sample with a gate and a delta-layer (δ) of donors supplying electrons to the 2D electron system.

function of n_s with steps at $n_s = iN_0$ (that is, when an integer number i of levels are filled and the number of electronic states on each of them per unit surface area is equal to $N_0 = eH/hc$). The step height Δμ (see Fig. 1) is determined by the values of the cyclotron and Zeeman splittings. Next, we will assume that Eq. (1) also remains valid in the case when the donor density depends on the (x, y) coordinates in the plane of the δ-layer of donors but weakly varies on the scale equal to d (this assumption is equivalent to neglect of the edge effects in a plane capacitor). In this case, the values of n_d, n_s, and μ become dependent on these coordinates. In accordance with Eq. (1), the electron density at given values of n_d and V_g is found as the intersection point of the dependence $y = \mu(n_s)$ and the straight line $y = eV_g + \mu_g - \varepsilon_0 + \lambda n_d d_1 - \lambda n_s d_1$, where $\lambda = 4\pi e^2/\kappa$ (solid line *1* and the two dotted lines parallel to *1* in Fig. 1 corresponding to values $n_d = n_{d0}$ and $n_d = n_{d0} \pm \delta n_d/2$, respectively). For the step dependence $\mu(n_s)$ under consideration, the intersection point falls on either the vertical ($n_s = iN_0$) or one of the horizontal portions of this dependence. Each type of obtained solution is accomplished for a finite range of the density of ionized donors ($\delta n_d^{(1)} = \Delta\mu/\lambda d_1$ and $\delta n_d^{(2)} = N_0 d/d_1$, respectively). A set of points on the (x, y) plane that corresponds to the first of the above ranges forms a region occupied by the incompressible electron phase. On the contrary, the second range ($\delta n_d^{(2)}$) corresponds to the region of the perfect compressibility of the electron system. In the case when the jump Δμ equals the cyclotron splitting value, it is easy to verify that the ratio $\delta n_d^{(1)}/\delta n_d^{(2)} = \kappa\hbar^2/2m^*e^2d = a_B/2d$, where a_B is the Bohr radius in the given material. For samples with 2D electron systems occurring near a GaAs/AlGaAs heterojunction, $m^* = 0.07m_e$, $\kappa \approx 12$, and the value of d has a scale of 1000 Å, so that the ratio $\delta n_d^{(1)}/\delta n_d^{(2)}$ is much less than one. The behavior of the system under consideration depends on the relation between the values of $\delta n_d^{(1)}$ and $\delta n_d^{(2)}$ and the limits of variations of the donor density in the sample $\delta n_d = n_d^{\max} - n_d^{\min}$. At $\delta n_d < \delta n_d^{(1)}$, depending on V_g (or on the average value of electron density $\overline{n_s}$, which is the same) the electron system can be both found in either a uniform incompressible or compressible state and subdivided into regions in which one of these states is accomplished. In the case when incompressible regions with a constant electron density peculiar to these regions form in the sample, the change in the donor density at the (x, y) coordinates is compensated for by the change of the charge density in the gate. At $\delta n_d^{(1)} < \delta n_d < \delta n_d^{(2)}$, uniform states in the sample can be formed only by the compressible phase. Finally, at $\delta n_d > \delta n_d^{(2)}$, the uniform states cannot exist.

It is easy to see from Eq. (1) that a change in the gate voltage V_g leads to a change in the values of n_d, which determine the limits of the ranges corresponding to different types of compressibility of the electron system, that is, to motion of the compressible and incompressible regions. Here, we consider the motion of these regions in the case of $\delta n_d^{(1)} \ll \delta n_d < \delta n_d^{(2)}$. If these inequalities are fulfilled and the donor density is characterized by long-period fluctuations (compared to d), the incompressible phase occupies only a small part of the sample surface area and mainly separates regions with partially filled Landau levels. First, we consider a very simple geometry when the donor density depends only on the x coordinate (Fig. 2). The width of the strip of the incompressible phase arising in this case equals $w = \delta n_d^{(1)}/(dn_d/dx)|_{x = x_0} = \Delta\mu/\lambda d_1 (dn_d/dx)|_{x = x_0}$, and the velocity of its motion is $dx_0/dV_g = -e/\lambda d_1 (dn_d/dx)|_{x = x_0}$ (here, x_0 is the coordinate of the point at which the chemical potential falls in the middle of the band gap). Note that the expression obtained for the width of the strip of the incompressible phase differs in its structure and by the linear dependence on the value of Δμ from the expression obtained in [2] for structures without a gate, where $w \sim \sqrt{\Delta\mu}$. It is natural that our consideration is valid only at $w \gg d$. Let us calculate the change in the charge Q of a plane capacitor formed by the layer of 2D electrons and the gate (see the inset in Fig. 1) upon a small change in the gate voltage ΔV_g. We will consider in this case that the charge of donors is frozen and does not vary upon variation of V_g, as usually occurs in real samples. From Eq. (1), it is evident that the change in the surface electron density in the com-

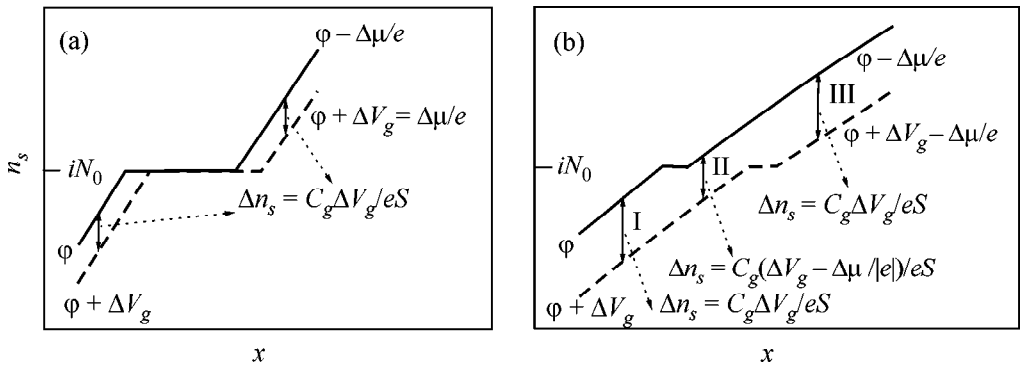

Fig. 2. Dependence of the electron density n_s on the x coordinate in the region of a sample near the strip of the incompressible phase for two values of the gate voltage (solid and dashed lines) differing by the ΔV_g value. Panels (a) and (b) refer to the cases of $d \ll w$ and $d \gg w$, respectively. The values of the electric potential (φ, etc.) in regions separated by an incompressible strip are indicated near the curves.

pressible regions equals $\Delta n_s = \kappa \Delta V_g/4\pi e d$. Moreover, it is easy to see in Fig. 2a that the capacitor at $w \gg d$ is charged as though a strip of width w in the sample simply does not takes a charge. As a result, the measured capacitance $C \equiv dQ/dV_g$ must be smaller than the geometrical capacitance $C_g = \kappa S/4\pi d$ (here, S is the area of the capacitor plates) because of the decrease in the effective area of the plates by the quantity δS proportional to w. This result can be easily generalized to the case of smooth fluctuations of the donor density in both coordinates defined by the distribution function $f(n_d, \overline{n_d})$ (here, $\overline{n_d}$ is the average value of n_d). At the chosen relation $\delta n_d^{(1)} \ll \delta n_d$, the wanted equation for the change in the capacitor charge takes the form $\Delta Q = \kappa(S - \delta S)\Delta V_g/4\pi d = \kappa S \Delta V_g(1 - f(n_{d0}, \overline{n_d})\delta n_d^{(1)})/4\pi d$, where n_{d0} is the donor density corresponding to the position of the chemical potential in the middle of the band gap. Thereby, we showed that the measured capacitance of the capacitor in the case under consideration is smaller than the geometrical capacitance C_g by the value $|\Delta C| = C_g \Delta\mu f(n_{d0}, \overline{n_d})/\lambda d_1 = C_g^2 \Delta\mu f(n_{d0}, \overline{n_d})d/Se^2 d_1$. This expression can be reduced to the expression for the correction to the capacitance [11]. This correction can be derived from Eq. (34) in [10] obtained by neglecting the sizes of the regions of the incompressible phase and phenomenologically introducing a Gaussian distribution function for the electron density in the 2D system. For this purpose, it should be assumed that the donor density is described by a Gaussian distribution and the electron density is described by the distribution function induced by the distribution chosen for donors in the case of perfect screening. It is easy to notice that this distribution is also described by a Gaussian function with a distribution width for electrons σ that differs from the corresponding value for the donor density σ_d by the geometrical factor $\sigma = d_1\sigma_d/d$. As a result, we obtain the following equation for the correction to the capacitance caused by the chemical potential jump:

$$\Delta C = -\frac{C_g^2}{S}\frac{\Delta\mu}{e^2}\frac{1}{\sqrt{\pi}\sigma}\exp\left(-\frac{(iN_0 - \overline{n_s})^2}{\sigma^2}\right). \qquad (2)$$

The consideration presented above is related to the case when the width of the incompressible strip is significantly larger than the distance to the gate d. At the same time, it is evident that the width of incompressible strips can be much smaller than d when the distance between the donor layer and the 2D system is much smaller than the distance to the gate. In this case, the formation of strips proceeds through a mechanism similar to that considered in [2]. If, at the same time, the distance between strips is much larger than d, the capacitor approximation used above is applicable at large distances from the strip. Let us find in this case the change in the capacitor charge upon a change in the gate voltage by a value of $\Delta V_g \gg \Delta\mu/e$, accompanied by displacement of narrow strips of the incompressible phase (Fig. 2b). In the presence of only one strip, the capacitor is naturally subdivided into three regions: region I with $n_s < iN_0$ is separated from region III with $n_s > iN_0$ by region II through which the incompressible strip has passed, as a result of which the relation between n_s and iN_0 in this region has changed. It is easily seen that the change in the voltage difference (and, respectively, in the electron density) with respect to the gate in region II differs from the corresponding value in regions I and III by a value of $\Delta\mu/e$. Then, the change in the capacitor charge is $\Delta Q = \kappa((S - \Delta S)\Delta V_g + \Delta S(\Delta V_g - \Delta\mu/|e|))/4\pi d$. Here, ΔS is the value by which the area of the region with $n_s < iN_0$ has changed upon the change in the gate voltage. If the electron density distribution in a sample is described by the function $f(n_s, \overline{n_s})$, then $\Delta S \approx Sf(iN_0, \overline{n_s})C_g\Delta V_g/|e|S$ and, in the

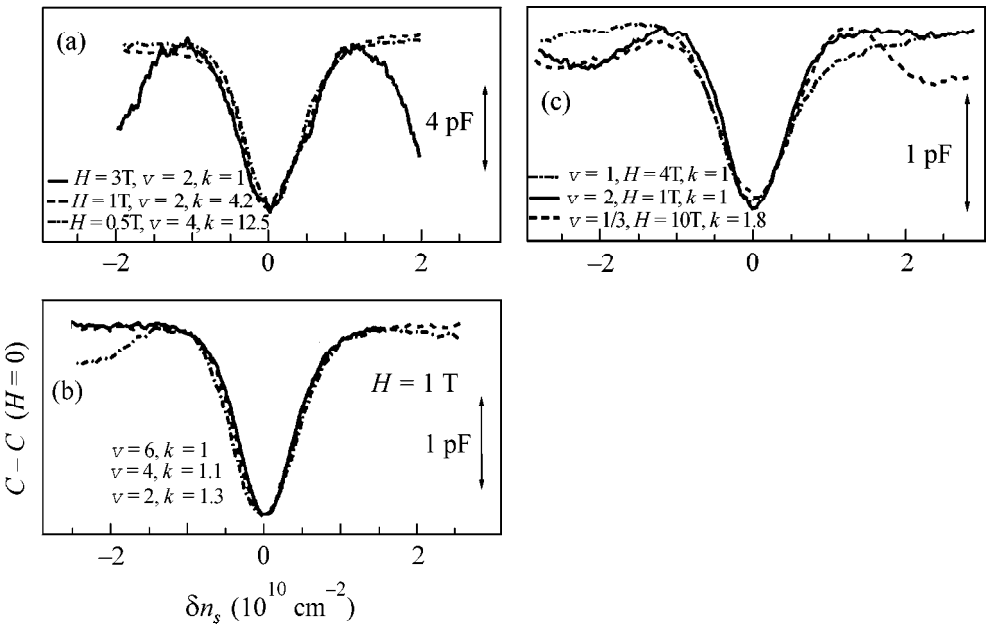

Fig. 3. Comparison of the shapes of the minima in the capacitance corresponding to chemical potential jumps in states of the integer and fractional quantum Hall effects. The procedure of comparison is described in the text.

case of the Gaussian distribution, we obtain an equation for the capacitance that coincides with Eq. (2).

The consideration given above indicates that the shape and the width of the peculiarity in the capacitance of a field-effect transistor corresponding to a chemical potential jump are determined by the density distribution function of ionized donors (which, in the case when the incompressible phase occupies a small part of the sample area, leads to an electron distribution function of the same shape); therefore, these features should depend neither on the magnitude of the jump $\Delta\mu$ (that is, in particular, on the magnetic field) nor on the nature of this jump. It is this behavior that was observed for the peculiarity in the capacitance of a field-effect transistor based on a single GaAs/AlGaAs heterojunction with the following architecture of layers above the heterojunction: AlGaAs layer (70 nm)–delta-layer of donors (Si)–AlGaAs layer (500 nm)–delta-layer of donors (Si)–GaAs layer (10 nm). The structure surface was coated with a metal layer that formed a Schottky barrier with the heterojunction. The size of the rectangular gate was 0.4×2.3 mm. A layer of 2D electrons was formed near the heterojunction on the GaAs side. The absolute value of the capacitance between the gate and the 2D system was found equal to approximately 165 pF. The experimental data for the shape of the minima in the capacitance presented in Fig. 3 turned out to be coincident for all samples made of the same plate of the material. The shapes of the various minima were compared using their parallel translation without changing the scale of the horizontal axis n_s and also using a change of the scale of the vertical axis by multiplying the signal by a factor k. This factor is given in the figures together with the values of the filling factors corresponding to the minima and with the values of the magnetic field at which the corresponding curves were measured. It is evident in Fig. 3 that the peculiarities in the capacitance have near-Gaussian shape. The minima have similar widths for the even filling factors (Figs. 3a, 3b) when the chemical potential jump is determined mainly by the cyclotron splitting; for the odd factors (Fig. 3c), when the Coulomb effects are dominant and significantly increase the splitting compared to the seed Zeeman value; and for the fractional filling factor of 1/3, when the fractional quantum Hall effect is observed and the energy gap is fully determined by the electron–electron interaction. It should be mentioned that the observed behavior of the width of the capacitance peculiarity fully contradicts the behavior expected in the case of short-range scatterers [12], when the broadening of the Landau levels depends on the magnetic field magnitude and the level number.

The authors are grateful to the Russian Foundation for Basic Research, INTAS, and Russian MNTP "Physics of Solid-State Nanostructures."

REFERENCES

1. A. L. Éfros, Phys. Rev. B **45**, 11354 (1992).
2. D. B. Chklovskiĭ, B. I. Shklovskiĭ, and L. I. Glazman, Phys. Rev. B **46**, 4026 (1992).
3. D. B. Chklovskiĭ, K. A. Matveev, and B. I. Shklovskiĭ, Phys. Rev. B **47**, 12605 (1993).

4. N. R. Cooper and J. T. Chalker, Phys. Rev. B **48**, 4530 (1993).
5. J. H. Davies and I. A. Larkin, Phys. Rev. B **49**, 4800 (1994).
6. A. V. Khaetskiĭ, V. I. Fal'ko, and G. E. W. Bauer, Phys. Rev. B **50**, 4571 (1994).
7. I. A. Larkin and J. H. Davies, Surf. Sci. **361**/**362**, 517 (1996).
8. J. H. Oh and R. R. Gerhardts, Phys. Rev. B **56**, 13519 (1997).
9. V. B. Shikin, Pis'ma Zh. Éksp. Teor. Fiz. **66**, 545 (1997) [JETP Lett. **66**, 581 (1997)].
10. F. G. Pikus and A. L. Efros, Phys. Rev. B **47**, 16395 (1993).
11. S. I. Dorozhkin, R. J. Haug, K. von Klitzing, and K. Ploog, Phys. Rev. B **51**, 14729 (1995).
12. T. Ando, A. B. Fowler, and F. Stern, Rev. Mod. Phys. **54**, 437 (1982).

Translated by A. Bagatur'yants

JETP Letters, Vol. 71, No. 10, 2000, pp. 422–425. Translated from Pis'ma v Zhurnal Éksperimental'noĭ i Teoreticheskoĭ Fiziki, Vol. 71, No. 10, 2000, pp. 612–617.

CONDENSED MATTER

Orientational Pinning of the Striped Phase in a Quantum Hall Liquid

É. E. Takhtamirov and V. A. Volkov

Institute of Radio Engineering and Electronics, Russian Academy of Sciences, Mokhovaya ul. 11, Moscow, 103907 Russia

Received April 4, 2000; in final form, April 10, 2000

A new class of collective states, which are assumed to be due to the spontaneous formation of a charge density wave ("striped" phase) upon filling high Landau levels, was recently observed in a 2D electron system based on GaAs/AlGaAs(001). The following unsolved problem is considered in the work: what is the reason for stripe pinning along the crystallographic direction [110]? It is shown that the effective mass of 2D electrons is anisotropic for a single heterojunction (001) A_3B_5. This natural anisotropy is due to the C_{2v} symmetry of the heterointerface and, even being weak (0.1%), can govern the stripe direction. A magnetic field parallel to the interface induces "magnetic" anisotropy of effective mass. The competition of these two types of anisotropy (natural and magnetic) provides a quantitative description of the experiment. © *2000 MAIK "Nauka/Interperiodica".*

PACS numbers: 73.20.Dx; 73.40.Hm; 71.45.Lr

1. Introduction. Even before the discovery of the quantum Hall effect, it had been assumed [1] that a uniform 2D electron system in strong magnetic fields corresponding to the filling of the lowest Landau level, $N = 0$ (filling factor $\nu < 1$), can be unstable against the formation of a 1D charge density wave with a period on the order of magnetic length. This instability is due to the exchange interaction resulting in the effective attraction between electrons. The analysis was carried out in the Hartree–Fock approximation, which overestimates the exchange interaction and ignores electron–electron correlations. After the discovery of the fractional quantum Hall effect, it became clear that, for $\nu < 1$, it is the correlation interaction that leads to the formation of a uniform state of the Laughlin liquid type. Nevertheless, the role of correlations diminishes with filling a large number of Landau levels and, in principle, one can expect the indicated instability to appear. It was predicted in 1996 [2] that a 1D charge density wave may appear near the half-filling of Landau levels, beginning with $N = 2$ [3]. Such a striped phase with a period of the order of the Larmor diameter should be energetically more favorable than the Laughlin liquid and the Wigner crystal [2, 4].

How should this phase be manifested in the transport measurements if it is really formed and pinned for some reason? Such a problem was considered, probably, for the first time in a series of old papers [5–7], where the anisotropic conductivity was calculated [5] and the high-frequency [6] and heating [7] effects were studied. In the presence of a periodic 1D potential $U(x)$ induced by the charge density wave, each Landau level transforms into a narrow 1D band. At the edges of this band, the density of states has a power divergence, which is cut off upon including weak scattering. As a result, the density of states $S(E_f)$ at the Fermi level has the shape of a two-toothed fork: a minimum in the center of the band and two peaks at the band edges; the lower the density n_{im} of scatterers, the higher the peaks. Incomplete filling of this band results in the formation of stripes differing in the ν value [of the type $\nu/(\nu-1)/\nu/\ldots$] and aligned with the y-axis. The transverse (σ_{xx}) and longitudinal (σ_{yy}) conductivities obey different mechanisms and qualitatively differently depend on ν: the σ_{yy} conductivity is high, has a band character, and is inversely proportional to n_{im} and $S^2(E_f)$, while σ_{xx} is low, has a hopping character, and is proportional to n_{im} and $S^2(E_f)$, with the product $\sigma_{xx}\sigma_{yy}$ being independent of scattering. These results were confirmed and generalized in [8, 9]. What did the experiment actually reveal?

In 1999, the conductivity of an electron system with ultrahigh mobility in the GaAs/AlGaAs(001)-based structures was studied at very low temperatures near half-integer $\nu \geq 9/2$, and a new state was revealed [10–13] which was assumed to be just the one associated with the formation of a striped phase predicted in [2]. This assumption was primarily based on the observation of a giant resistance anisotropy in this system. The ratio of resistances along the crystallographic directions $[1\bar{1}0]$ and [110] reaches the values of $R_{xx}/R_{yy} \sim 5$–3500, depending on the sample geometry, where [110] is the "easy" conductivity direction. Moreover, the behavior of all conductivity tensor components qualitatively agrees with the theory [5, 8, 9]. The predicted behavior of the $\sigma_{xx}\sigma_{yy}$ product near the half-filling of the upper Landau level numerically agrees with the experiment [14]. It was also shown in [12, 13] that the

magnetic field $B_\parallel \sim 1$ T parallel to the interface can change the direction of easy conductivity. The authors of [12] concluded that, at high enough $B_\parallel$, the direction of easy conductivity is perpendicular to the $B_\parallel$ direction. A similar result was obtained in [13] for $\mathbf{B}_\parallel \parallel [110]$ near all half-integer $\nu \geq 9/2$ and for $\mathbf{B}_\parallel \parallel [1\bar{1}0]$ near $\nu = 11/2$ and $\nu = 15/2$. The theoretical analysis [15, 16] of the influence of $\mathbf{B}_\parallel$, carried out in the Hartree–Fock approximation in the model of a parabolic quantum well, partially explained the results. All this is strong evidence for the formation of a striped phase. However, the mechanism responsible for the orientation of the charge density stripes along a certain preferred direction in a macroscopic sample (orientational pinning) at $B_\parallel = 0$ remains to be clarified. This is one of the fundamental unsolved problems.

In this work, Kroemer's assumption [17] that the reduced (C_{2v}) symmetry of the potential in a heterostructure based on semiconductors without an inversion center can cause an appearance of a preferred direction for the conductivity is justified. Symmetry reduction means that the cubic axis normal to the interface is transformed from the fourfold mirror–rotational axis (S_4) to the twofold axis (C_2). We demonstrate below that, owing to the asymmetry of the potential of an atomically abrupt heterojunction, the effective mass (EM) of 2D electrons is anisotropic (natural anisotropy). At the same time, the presence of $\mathbf{B}_\parallel$ also gives rise to the EM anisotropy (magnetic anisotropy) [18]. Therefore, it is natural to treat (to the lowest order in $B_\parallel^2$) the results of many-particle numerical calculations of the $\mathbf{B}_\parallel$ effect on the orientation of the striped phase [15, 16] as a manifestation of the magnetic anisotropy of EM. Thus, the many-particle problem of orientational pinning of the striped phase reduces to a one-particle problem of determining the EM anisotropy. We derive below analytical expressions for both types of EM anisotropy (natural and magnetic) and demonstrate that they can compete with each other. At a certain magnitude and direction of $\mathbf{B}_\parallel$, these two types of anisotropy exactly cancel, leading to the disappearance of resistance anisotropy, in agreement with the experiment.

2. Natural anisotropy. Before proceeding to the many-particle problem, it is necessary to construct a one-particle Hamiltonian for the conduction band in a (001) III–V heterostructure. As was shown in [19], the correctly constructed multiband set of equations for the envelope functions retains information on the heterostructure symmetry C_{2v}, which is lower than the symmetry T_d of the constituent materials. This symmetry reduction is described, in particular, by certain short-range potentials localized at the heterointerface. Mixing of heavy and light holes at the center of the 2D Brillouin zone is one of the consequences of symmetry reduction [19, 20]. This mixing explains the giant optical anisotropy (with the same principal axes [110] and $[1\bar{1}0]$) that was discovered in [21] for the quantum wells based on semiconductors with different cations and anions. Evidently, low symmetry should also manifest itself in the equation for the envelope functions in the conduction band. Nevertheless, a single-band equation obtained in [19] carries no information on the C_{2v} symmetry, because the corresponding small contributions were neglected. We must now take them into account. Since the terms with the symmetry higher than C_{2v} are of no interest here, the effective Hamiltonian can include only the operators of kinetic and potential energies used in the standard EM approximation, as well as the anisotropic contribution of C_{2v} symmetry, which will be obtained below.

A single-band Hamiltonian of the C_{2v} symmetry can be obtained by the method of invariants. Leaving aside spin–orbit interaction, one can conclude that the C_{2v} symmetry should manifest itself in the kinetic energy operator. Let us direct the 2D quasi-momentum components along the cubic axes: $p_x \parallel [100]$ and $p_y \parallel [010]$. Then the part of the kinetic energy operator quadratic in the generalized 2D momentum (P_x, P_y) should be

$$T = \frac{P_x^2 + P_y^2}{2m^*} + \frac{1}{2}\mathcal{A}(P_xP_y + P_yP_x). \quad (1)$$

Here, m^* is the EM of the conduction band and the quantity $\mathcal{A}$ (which may depend on z) accounts for the natural anisotropy of EM in the plane of 2D electron gas. Let us obtain an explicit expression for $\mathcal{A}$ by using a multiband matrix Hamiltonian [19] acting on the column of envelope functions. In the **k** representation, it takes the form

$$H_{nn'}^{(\mathrm{eff})} = H_{nn'}^{(kp)} + \frac{1}{2\pi}D_{0nn'}, \quad (2)$$

where n and n' are the band indices. The first term in Eq. (2) includes the contributions from the smooth potentials and **kp** interaction and has the standard form. The second term in Eq. (2) is a contribution from the atomically abrupt heterointerface potential taken to first order in the small parameter $\bar{k}a$, where $1/\bar{k}$ is the characteristic length of changing the envelope functions and a is the lattice constant. One can pass to the single-band variant of envelope-function calculations by applying the perturbation theory, with the **kp** and $\mathbf{D}_0$ operators as small perturbation. The second order in the **kp** interaction gives the first (standard) term in Eq. (1). The third order (second order in **kp** and first in $\mathbf{D}_0$) provides the second term of Eq. (1), with $\mathcal{A}(z) = \alpha\delta(z)$ and

$$\alpha = \sum_{n,n'}{}' \frac{2\langle c|p_x|n\rangle D_{0nn'}\langle n'|p_y|c\rangle + 4D_{0cn}\langle n|p_x|n'\rangle\langle n'|p_y|c\rangle}{m_0^2(\epsilon_c - \epsilon_n)(\epsilon_c - \epsilon_{n'})}. \quad (3)$$

Here, $\delta(z)$ is the Dirac delta function, $z = 0$ defines the heterointerface position, $\langle n|p_i|n'\rangle$ is the ith component of the interband momentum matrix element, c is the index of conduction band, m_0 is the mass of free electron, and ϵ_n is the energy of the nth band edge in one of the structure materials. In the simplest model, the key parameters $D_{0nn'}$ of the theory have the form

$$D_{0nn'} = \sum_{j=\pm1,\pm2,\ldots} \frac{\langle n|\delta U \sin(4\pi jz/a)|n'\rangle}{4\pi j/a} \times \int_{-\infty}^{+\infty} \frac{dG(z)}{dz} \cos\left(\frac{4\pi}{a} jz\right) dz. \quad (4)$$

The functions $G(z)$ and $\delta U(\mathbf{r})$ are so defined that the crystal potential of the heterostructure has the form $U(\mathbf{r}) = U_1(\mathbf{r}) + G(z)\delta U(\mathbf{r})$, where U_1 and $U_2 = U_1 + \delta U$ are the crystal potentials of both structure materials. Note that the D_{0XY} parameter accounts for the mixing of the heavy and light holes at the center of the 2D Brillouin zone, with X and Y being the indices of the Bloch functions corresponding to the edge of the Γ_{15} valence band and transforming as x and y under symmetry operations of the T_d group [19, 20].

3. Inclusion of the "magnetic" anisotropy. Reducing the tensor of reciprocal effective mass to the principal axes, so that $x \parallel [1\bar{1}0]$ and $y \parallel [110]$ in the new coordinates, and introducing magnetic field $\mathbf{B}$ in the vector-potential gauge $\mathbf{A} = (B_y z, -B_x z + B_z x, 0)$, one obtains for the orbital part of the 3D Hamiltonian of conduction band

$$H_{3D} = \frac{p_z^2}{2m^*} + V(z) + \frac{1}{2}\left(\frac{1}{m^*} - \alpha\delta(z)\right)\left(p_x + \frac{e}{c}B_y z\right)^2 + \frac{1}{2}\left(\frac{1}{m^*} + \alpha\delta(z)\right)\left(p_y - \frac{e}{c}B_x z + \frac{e}{c}B_z x\right)^2. \quad (5)$$

Here, $V(z)$ is the effective potential of the conduction band edge, e is the elementary charge, and c is the light speed. For a finite thickness of the 2D layer, the magnetic field component parallel to the heterointerface can be treated perturbatively [18]. To second order in $B_\parallel$, this procedure brings about a diamagnetic shift of the dimensional-quantization subbands and an increase (for the lowest subband) in EM in the direction perpendicular to $\mathbf{B}_\parallel$. The natural EM anisotropy can also be treated perturbatively. For simplicity, we assume that $\mathbf{B}_\parallel$ is parallel to either $[1\bar{1}0]$ or $[110]$, so that $B_x B_y = 0$. Collecting all terms second-order in $B_\parallel$ and first-order in α, one obtains the following expression for the 2D Hamiltonian of the lowest subband:

$$H_{2D}^1 = E_1 + \frac{e^2}{2m^*c^2}(B_x^2 + B_y^2)(\langle z^2\rangle_{11} - \langle z\rangle_{11}^2) + \frac{1}{2m^*}\left(1 - \frac{\Delta_{nat}}{2} - \frac{B_y^2}{B_\parallel^2}\Delta_B\right)\left(p_x + \frac{e}{c}B_y\langle z\rangle_{11}\right)^2 + \frac{1}{2m^*}\left(1 + \frac{\Delta_{nat}}{2} - \frac{B_x^2}{B_\parallel^2}\Delta_B\right)\left(p_y + \frac{e}{c}B_z x - \frac{e}{c}B_x\langle z\rangle_{11}\right)^2. \quad (6)$$

The parameters of the natural EM anisotropy and the EM anisotropy induced by the magnetic field are

$$\Delta_{nat} = 2m^*\alpha\langle\delta(z)\rangle_{11}, \quad \Delta_B = \frac{2e^2B_\parallel^2}{m^*c^2}\sum_m{}' \frac{|\langle z\rangle_{1m}|^2}{E_m - E_1}, \quad (7)$$

where E_m is the energy of the bottom of the mth subband at $B = 0$. The expression for Δ_B in Eq. (7) is valid to the terms second-order in the parameter $\hbar\omega_c/(E_2 - E_1)$, where $\omega_c = eB_z/m^*c$. For the field $B_z = 2.5$ T (in the experiment [13], this field corresponds to the filling factor $\nu = 9/2$), one can neglect this correction in the estimation of Δ_B, because $\hbar\omega_c \approx 4$ meV, while the gap $E_2 - E_1$ should exceed the Fermi energy E_f measured from the lowest subband; one has $E_f \approx 10$ meV for the 2D electron concentration $N_s = 2.7 \times 10^{11}$ cm^{-2}.

4. Estimates. Based on the experimental data [13], we estimate Δ_{nat} and Δ_B for $B_\parallel = 0.5$ T (if $\mathbf{B}_\parallel \parallel [110]$, this magnetic field converts the resistance from anisotropic to isotropic; at larger $B_\parallel$, the direction of "easy" conductivity rotates by 90°). Since the information on the samples is incomplete, we carried out a series of self-consistent calculations by varying the concentration N_a of residual acceptors in GaAs. At $N_a = 10^{14}$ cm^{-3} and N_s taken from [13], the results are

$$\sum_m{}' \frac{|\langle z\rangle_{1m}|^2}{E_m - E_1} \approx 1 \times 10^{-11} \text{ cm}^2/\text{eV}, \quad \langle\delta(z)\rangle_{11} \approx 1 \times 10^5 \text{ cm}^{-1}. \quad (8)$$

For other N_a values (from 10^{13} to 10^{15} cm^{-3}), the results differ from Eq. (8) by a factor less than two. Equations (7) and (8) yield the following value for the EM anisotropy induced by magnetic field $B_\parallel = 0.5$ T:

$$\Delta_B = 1.3 \times 10^{-3} = 0.13\%. \quad (9)$$

The parameter α can be determined from the equality $\Delta_{nat} = \Delta_B$ to give

$$\alpha = \frac{0.65 \times 10^{-8} \text{ cm}}{m^*} = 1.1 \times 10^{20} \text{ cm/g}. \quad (10)$$

The two-band approximation with energy gap E_g yields the following estimate for Eq. (3):

$$\alpha \sim \frac{2\langle c|p_x|X\rangle D_{0XY}\langle Y|p_y|c\rangle}{m_0^2 E_g^2} = \frac{D_{0XY}}{m^* E_g}. \qquad (11)$$

Thus, it follows from the experimental data [13] and Eqs. (10) and (11) that $D_{0XY} \sim 0.4 \times 10^{-8}$ eV cm. Let us compare this value with the literature data.

It was found in [20] that different estimates carried out for the GaAs/AlAs heterostructures either on the basis of pseudopotential and tight-binding calculations or from the comparison with the experiment on the anisotropic exchange splitting of exciton levels in the II-type superlattices GaAs/AlAs lead to a sizable scatter of the D_{0XY} parameter. The value obtained in [20] lies in the range $(0.35, 0.99) \times 10^{-8}$ eV cm. Using linear interpolation, one obtains the upper bound $D_{0XY} = 0.3 \times 10^{-8}$ eV cm for the GaAs/$Al_{0.3}Ga_{0.7}$As heterostructure. This value is in fair agreement with the value obtained above.

5. Discussion. We can now conclude that the natural anisotropy of EM is likely the mechanism that pins the stripe directions at $B_\parallel = 0$ (see also the end of Section 1). It follows from this conclusion that the parameter α entering Eq. (1) is negative, $\alpha < 0$. The competition between the natural anisotropy Δ_{nat} and anisotropy Δ_B induced by the magnetic field $\mathbf{B}_\parallel = (0, B_y)$ makes the 2D electron spectrum at $B_\parallel = 0.5$ T isotropic. As a result, the stripe directions are randomized and the resistance becomes isotropic. On further increase in $B_\parallel$, the magnetic anisotropy prevails and the stripes rotate at 90°. The role of EM anisotropy in the formation of many-electron anisotropic states can be understood as follows. A 2D electron system with anisotropic EM and isotropic Coulomb interaction is, obviously, equivalent to a 2D electron system with isotropic (cyclotron) mass and anisotropic Coulomb interaction. One can expect that this effective anisotropic interaction is precisely the one which pins the orientation of the striped phase to ensure its observation in the magnetotransport.

For holes, the heterointerface contribution of symmetry C_{2v} (and, hence, responsible for the pinning of the striped phase) is greater than for the conduction band, because it appears in the first-order perturbation treatment [19], whereas the anisotropic EM in Eq. (1) was obtained in the third order. For this reason, one would expect that the hole striped phase is more stable and can form upon filling the lower Landau levels (cf. [22]).

We are grateful to B.I. Shklovskiĭ for stimulating discussions and useful remarks. This work was supported by the Russian Foundation for Basic Research (project no. 99-02-17592), the INTAS (grant no. 97-11475), and the Russian State Programs "Physics of Solid-State Nanostructures" (project no. 99-1124) and "Surface Atomic Structures" (project no. 3.1.99).

REFERENCES

1. H. Fukuyama, P. M. Platzman, and P. W. Anderson, Phys. Rev. B **19**, 5211 (1979).
2. M. M. Fogler, A. A. Koulakov, and B. I. Shklovskiĭ, Phys. Rev. B **54**, 1853 (1996).
3. M. M. Fogler and A. A. Koulakov, Phys. Rev. B **55**, 9326 (1997).
4. R. Moessner and J. T. Chalker, Phys. Rev. B **54**, 5006 (1996).
5. G. R. Aĭzin and V. A. Volkov, Zh. Éksp. Teor. Fiz. **87**, 1469 (1984) [Sov. Phys. JETP **60**, 844 (1984)]; Zh. Éksp. Teor. Fiz. **92**, 329 (1987) [Sov. Phys. JETP **65**, 188 (1987)].
6. G. R. Aĭzin and V. A. Volkov, Fiz. Tekh. Poluprovodn. (Leningrad) **19**, 1780 (1985) [Sov. Phys. Semicond. **19**, 1094 (1985)].
7. G. R. Aĭzin and V. A. Volkov, Fiz. Tverd. Tela (Leningrad) **27**, 475 (1985) [Sov. Phys. Solid State **27**, 290 (1985)].
8. A. H. MacDonald and M. P. A. Fisher, Phys. Rev. B **61**, 5724 (2000).
9. F. von Oppen, B. I. Halperin, and A. Stern, Phys. Rev. Lett. **84**, 2937 (2000).
10. M. P. Lilly, K. B. Cooper, J. P. Eisenstein, *et al.*, Phys. Rev. Lett. **82**, 394 (1999).
11. R. R. Du, D. C. Tsui, H. L. Stormer, *et al.*, Solid State Commun. **109**, 389 (1999).
12. W. Pan, R. R. Du, H. L. Stormer, *et al.*, Phys. Rev. Lett. **83**, 820 (1999).
13. M. P. Lilly, K. B. Cooper, J. P. Eisenstein, *et al.*, Phys. Rev. Lett. **83**, 824 (1999).
14. J. P. Eisenstein, M. P. Lilly, K. B. Cooper, *et al.*, cond-mat/0003405 at xxx.lanl.gov.
15. T. Jungwirth, A. H. MacDonald, L. Smrčka, and S. M. Girvin, Phys. Rev. B **60**, 15574 (1999).
16. T. D. Stanescu, I. Martin, and P. Phillips, Phys. Rev. Lett. **84**, 1288 (2000).
17. H. Kroemer, cond-mat/9901016 at xxx.lanl.gov.
18. T. Ando, A. Fowler, and F. Stern, Rev. Mod. Phys. **54**, 437 (1982).
19. É. E. Takhtamirov and V. A. Volkov, Zh. Éksp. Teor. Fiz. **116**, 1843 (1999) [JETP **89**, 1000 (1999)].
20. E. L. Ivchenko, A. Yu. Kaminski, and U. Rössler, Phys. Rev. B **54**, 5852 (1996).
21. O. Krebs, W. Seidel, J. P. André, *et al.*, Semicond. Sci. Technol. **12**, 938 (1997).
22. M. Shayegan, H. C. Manoharan, S. J. Papadakis, and E. P. De Poortere, Physica E (Amsterdam) **6**, 40 (2000).

Translated by R. Tyapaev

JETP Letters, Vol. 71, No. 10, 2000, pp. 426–429. Translated from Pis'ma v Zhurnal Éksperimental'noĭ i Teoreticheskoĭ Fiziki, Vol. 71, No. 10, 2000, pp. 618–624.

CONDENSED MATTER

"Inversion Wake" of an Isolated Moving Pearl Vortex in a Thin Magnetic Superconductor Film

A. I. Lomtev

Galkin Physicotechnical Institute, National Academy of Sciences of Ukraine, Donetsk, 83114 Ukraine
e-mail: lomtev@kinetic.ac.donetsk.ua

Received January 6, 2000; in final form, April 6, 2000

The magnetic structure of an isolated two-dimensional Pearl vortex uniformly moving in a thin magnetic superconductor film is studied. The moving process and the magnetic subsystem sizably renormalize the Pearl vortex field and induce the formation of an "inversion wake" behind the vortex at a large distance on the order of $10\lambda_{\text{eff}}$ from its center. The effect can be observed in the magneto-optical experiments. © *2000 MAIK "Nauka/Interperiodica".*

PACS numbers: 74.76.-w; 74.60.-w

1. At present, a great many magnetic superconductors with new unique properties are known [1–3]. In addition to the ternary compounds [4], magnetism and superconductivity was found to coexist in HTSC compounds of the REBaCuO, RECuO, etc. types, where RE stands for the rare-earth ion. Strong antiferromagnetic correlation of copper spins within the CuO_2 planes in the superconducting state is among the crucial features of the HTSC materials [5].

An external magnetic field enters bulky type II magnetic superconductors in the form of Abrikosov vortices [6] to induce magnetization of a magnetic subsystem around the normal vortex core at a distance of at least the order of the London penetration depth λ. A rather intense transport electric current flowing through a superconductor in a rarefied mixed state suppresses pinning and causes the near-isolated Abrikosov vortices to move with a constant velocity [7].

In studying the magnetic structure of an isolated Abrikosov vortex slowly and uniformly moving in a bulky (three-dimensional) magnetic superconductor, it was predicted in [8] that an "inversion wake" should appear at large distances (of order 10λ) behind the vortex. Note that if the distance between the vortices $d_0 \gg \lambda$, the transport current in the bulk of a superconductor is absent (because of the Meissner effect) and the current flows only in a near-surface skin layer. For this reason, this phenomenon, strictly speaking, cannot be reduced to a two-dimensional problem (as it was done in [8]), because the system is nonuniform along the core axis Z.

Therefore, the solution obtained in [8] for the two-dimensional case and the properties of this solution are valid only in the superconductor bulk, namely, in the regions at distances $h_0 \gg \lambda$ from the interfaces, where the system can approximately be regarded as two-dimensional. As the interface between superconductor and vacuum is approached, the solution will alter, and it is not at all evident whether the inversion wake phenomenon will persist in the exact solution of the three-dimensional problem. Another important point is that the inversion wake behind the Abrikosov vortex is very difficult, if ever, to observe experimentally in the superconductor bulk. It will be seen below that this problem does not arise in the case of a thin superconducting film.

The external magnetic field enters the thin magnetic superconductor films of thickness $d \ll \lambda$ in the form of two-dimensional Pearl vortices [9–11] and induces the magnetization of a magnetic subsystem around the normal vortex core at distances on the order of the effective Pearl penetration depth $\lambda_{\text{eff}} = \lambda^2/d \gg \lambda$. A rather intense transport current flowing through the superconducting film in a rarefied mixed state suppresses pinning and causes the near-isolated Pearl vortices to move with a constant velocity v. It is known that the vortex moves with the velocity proportional to the transport current, which also creates a magnetic field. Note that, due to the linearity of the Maxwell equations (because of the superposition principle), the constant additive correction from the magnetic field of the transport current to the total magnetic field of the Pearl vortex is proportional to the vortex speed v and does not affect the final solution. Moreover, owing to the inequality $v/c \ll 1$, this correction is negligibly small even compared to the magnetic field of the inversion wake and, thus, can be ignored.

It is clear from the above that the study carried out in this work on the magnetic structure of an isolated Pearl vortex uniformly moving in an ultrathin magnetic superconductor film of thickness $d \ll \lambda$ is a topical problem. This problem is reduced to that of an infinitely thin two-dimensional plane, for which all physical characteristics (field, current, etc.) of the vortex can be regarded as independent of the z-coordinate perpendicular to the plate plane.

0021-3640/00/7110-0426$20.00

We assume that the system of interest is two-dimensional regarding not only its superconducting but also magnetic properties, so that the film permeability can be written as $\mu(\mathbf{r} - \mathbf{r}', t - t') = \mu(\boldsymbol{\rho} - \boldsymbol{\rho}', t - t')\delta(z - z')$, where $\mathbf{r} = (x, y, z)$, $\boldsymbol{\rho} = (x, y)$ and $\delta(z)$ is the Dirac delta function.

The geometry of the problem is as follows: the film plane coincides with the *XY*-plane, while the vortex field is aligned with the *Z*-axis.

We also assume that the conduction electrons interact with the spin subsystem through the electromagnetic (dipole) interaction, while the exchange spin–spin interaction is neglected.

As usual, the structure of the vortex core is ignored in the London approximation, in accordance with the condition $\lambda \gg \xi$ and, hence, $\lambda_{\text{eff}} \gg \xi$ (ξ is the correlation length). When considering the isolated vortices in a thin film, one assumes implicitly that the distances between them $d_0 \gg \lambda_{\text{eff}}$ in the strongly rarefied mixed state in the range of magnetic fields $H_{c1} < B \ll H_{c2}$. Nevertheless, owing to the inequality $d \ll \lambda$, the transport current flows across the whole width of the film.

It was first pointed out in [12] that the vortex motion is driven by the Lorentz force from the superfluid current component.

We use the kinematic approach and assume that the dynamic equations allowing for the "pinning" and other dissipation mechanisms [7, 13] are already solved for the Pearl vortex and the class of solutions chosen corresponds to the uniform movement of the isolated vortex line.

It should be noted that the vortex distortion in the mixed superconducting state, in principle, should also be taken into account [14]. However, in the strongly rarefied mixed state assumed in this work, the distortion is insignificant because of the low vortex concentration and does not affect quantitatively, or even qualitatively, the "inversion wake" phenomenon for a moving Pearl vortex.

2. Following [15–17], we start from the Maxwell equation for the flux density $\mathbf{B}(\mathbf{r}, t) = \text{rot}\mathbf{A}(\mathbf{r}, t)$ [$\mathbf{A}(\mathbf{r}, t)$ is the vector potential] created by the undamped current $\mathbf{j}(\mathbf{r}, t)$ and magnetization vector $\mathbf{M}(\mathbf{r}, t)$:

$$\text{rot}\mathbf{B}(\mathbf{r}, t) = (4\pi/c)\mathbf{j}(\mathbf{r}, t) + 4\pi\text{rot}\mathbf{M}(\mathbf{r}, t). \quad (1)$$

With the London gauge $\text{div}\mathbf{A}(\mathbf{r}, t) = 0$ for the potential, the relationship between current, potential, and phase $\Theta(\mathbf{r}, t)$ of the order parameter takes the form [15]

$$\mathbf{j}(\mathbf{r}, t) = \frac{c}{4\pi\lambda^2}[\mathbf{S}(\boldsymbol{\rho}, t) - \mathbf{A}(\mathbf{r}, t)], \quad (2)$$

where vector function $\mathbf{S}(\boldsymbol{\rho}, t)$ is related to the phase gradient by the condition

$$\mathbf{S}(\boldsymbol{\rho}, t) = \frac{\Phi_0}{2\pi}\nabla\Theta(\boldsymbol{\rho}, t), \quad (3)$$

with Φ_0 being the magnetic flux quantum. With regard to Eq. (3), the phase of order parameter satisfies the equation with source

$$\text{rot}\mathbf{S}(\boldsymbol{\rho}, t) = \hat{\mathbf{z}}\Phi_0\delta(\boldsymbol{\rho} - \boldsymbol{\rho}_0(t)), \quad (4)$$

where $\hat{\mathbf{z}}$ is unit vector (directed along the *Z*-axis) of the vortex line at point $\boldsymbol{\rho}_0(t)$.

For a thin magnetic superconductor film, Eq. (2) for the current density can be written as

$$\mathbf{j}(\mathbf{r}, t) = \mathbf{I}(\boldsymbol{\rho}, t)\delta(z) = \mathbf{j}(\boldsymbol{\rho}, t)d\delta(z) = \frac{cd}{4\pi\lambda^2}[\mathbf{S}(\boldsymbol{\rho}, t) - \mathbf{A}(\mathbf{r}, t)]\delta(z). \quad (5)$$

The magnetic field $\mathbf{H}(\mathbf{r}, t)$ is related to the flux density $\mathbf{B}(\mathbf{r}, t)$ by the integral expression

$$\mathbf{H}(\boldsymbol{\rho}, z, t) = \int_{-\infty}^{t} dt' \int_{-\infty}^{\infty} d\boldsymbol{\rho}'\mu^{-1}(\boldsymbol{\rho} - \boldsymbol{\rho}', t - t')\mathbf{B}(\boldsymbol{\rho}', z, t'). \quad (6)$$

From Eqs. (1)–(6) one obtains an equation for the vector potential

$$\text{rot}\left\{\int_{-\infty}^{t} dt' \int_{-\infty}^{\infty} d\boldsymbol{\rho}'\mu^{-1}(\boldsymbol{\rho} - \boldsymbol{\rho}', t - t')\text{rot}\mathbf{A}(\boldsymbol{\rho}', z, t')\right\} = \lambda_{eff}^{-1}[\mathbf{S}(\boldsymbol{\rho}, t) - \mathbf{A}(\boldsymbol{\rho}, z, t)]\delta(z), \quad (7)$$

in which it is expressed through the source field $\mathbf{S}(\boldsymbol{\rho}, t)$.

It follows from Eq. (2) and equality $\text{div}\mathbf{j}(\mathbf{r}, t) = 0$ that $\text{div}\mathbf{S}(\boldsymbol{\rho}, t) = 0$. Applying the curl operation to Eq. (4), one arrives at the following equation for the source field $\mathbf{S}(\boldsymbol{\rho}, t)$:

$$\text{rotrot}\mathbf{S}(\boldsymbol{\rho}, t) = -\Delta\mathbf{S}(\boldsymbol{\rho}, t) = \Phi_0\text{rot}[\hat{\mathbf{z}}\delta(\boldsymbol{\rho} - \mathbf{v}t)], \quad (8)$$

where $\boldsymbol{\rho}_0(t) = \mathbf{v}t$ for a vortex uniformly moving with velocity $\mathbf{v}$.

Defining the flux density through the vector potential and making use of the relationship between the magnetic field, the flux density, and the film permeability, one obtains from the set of Eqs. (7) and (8) the following expression for the time-dependent Fourier component of the vortex magnetic field:

$$\mathbf{H}(\mathbf{q}, t) = \hat{\mathbf{z}}\Phi_0\frac{\exp(-i\mathbf{q}\mathbf{v}t)}{\mu(\mathbf{q}, \mathbf{q}\mathbf{v}) + 2q\lambda_{\text{eff}}}, \quad (9)$$

where the vector $\mathbf{q} = (\mathbf{q}_x, \mathbf{q}_y)$, and $q = (\mathbf{q}_x^2 + \mathbf{q}_y^2)^{1/2}$. This formula is valid for any type of ordering in the magnetic subsystem, i.e., for any functional form of the permeability dispersion $\mu(\mathbf{q}, \omega)$.

The following distinctions between Eq. (9) for the Pearl vortex in a two-dimensional superconductor and the corresponding Eq. (6) in [8] for the Fourier component of the magnetic field of the Abrikosov vortex in a three-dimensional superconductor are noteworthy. First, the functional dependence on the two-dimen-

sional wave vector **q** is other than in the three-dimensional case and, second, the characteristic spatial scales of field variation are different: λ in the three-dimensional superconductor and $\lambda_{\text{eff}} \gg \lambda$ in the two-dimensional superconductor.

Since $\lambda \gg a$ (a is the lattice constant), it is natural to apply a hydrodynamic description to the magnetic subsystem. Restricting ourselves to the paramagnetic temperatures, we can write for the permeability of the two-dimensional film [18]

$$\mu(\mathbf{q}, \omega) = \mu_1(\mathbf{q}, \omega) + i\mu_2(\mathbf{q}, \omega) = 1 + \frac{i4\pi\chi_0 Dq^2}{\omega + iDq^2}, \quad (10)$$

where χ_0 is the static magnetic susceptibility, and the coefficient of spin diffusion for the two-dimensional Heisenberg magnetics is [19] $D = (1/3)(2\pi)^{1/2}Ja^2[s(s+1)]^{1/2}$ (J is the intralayer exchange parameter, and s is the spin value).

Strictly speaking, the superconducting currents screen the long-wavelength portions of the exchange and electromagnetic interactions, thereby renormalizing the parameters of magnetic subsystem [20]. However, we will not take this into account, because we consider the paramagnetic range of temperatures and are interested only in the order-of-magnitude estimates.

Using Eq. (10) for the magnetic permeability, the Fourier component of vortex field (9) can be represented as

$$H(p_x, p_y, \tau) = \hat{\mathbf{z}}\Phi_0[H_{\text{Re}}(p_x, p_y, \tau) - iH_{\text{Im}}(p_x, p_y, \tau)], \quad (11)$$

where

$$H_{\text{Re}}(p_x, p_y, \tau) = \{[\mu_1(\mathbf{p}, \eta p_x) + 2p]^2 + \mu_2^2(\mathbf{p}, \eta p_x)\}^{-1} \quad (12)$$
$$\times \{[\mu_1(\mathbf{p}, \eta p_x) + 2p]\cos(p_x\tau) - \mu_2(\mathbf{p}, \eta p_x)\sin p_x\tau\},$$

$$H_{\text{Im}}(p_x, p_y, \tau) = \{[\mu_1(\mathbf{p}, \eta p_x) + 2p]^2 + \mu_2^2(\mathbf{p}, \eta p_x)\}^{-1} \quad (13)$$
$$\times \{[\mu_1(\mathbf{p}, \eta p_x) + 2p]\sin(p_x\tau) + \mu_2(\mathbf{p}, \eta p_x)\cos(p_x\tau)\},$$

$$\mu_1(\mathbf{p}, \eta p_x) = 1 + 4\pi\chi_0 p^4/(p^4 + \eta^2 p_x^2),$$
$$\mu_2(\mathbf{p}, \eta p_x) = 4\pi\chi_0\eta p_x p^2/(p^4 + \eta^2 p_x^2). \quad (14)$$

In these expressions, the following dimensionless variables are introduced: $p = (p_x^2 + p_y^2)^{1/2} = q\lambda_{\text{eff}}$; $p_x = q_x\lambda_{\text{eff}}$; $p_y = q_y\lambda_{\text{eff}}$; $\tau = vt/\lambda_{\text{eff}}$; and $\eta = v/v_0$, where the characteristic velocity $v_0 = D/\lambda_{\text{eff}}$; and the vortex is assumed to move in the positive direction of the X-axis.

Making use of Eqs. (11)–(14) and applying the inverse Fourier transform, we obtain the integral representation for the magnetic-field distribution in the isolated two-dimensional Pearl vortex uniformly moving in a thin magnetic superconductor film,

$$\mathbf{H}(x, y, t) = \mathbf{H}_S(x, y, t) + \mathbf{H}_A(x, y, t)$$
$$= \frac{\hat{\mathbf{z}}\Phi_0}{(\pi\lambda_{\text{eff}})^2}\left\{\int_0^\infty dp_x \int_0^\infty dp_y H_{\text{Re}}(p_x, p_y, \tau)\right.$$
$$\times \cos(p_x x/\lambda_{\text{eff}})\cos(p_y y/\lambda_{\text{eff}}) \quad (15)$$
$$\left. + \int_0^\infty dp_x \int_0^\infty dp_y H_{\text{Im}}(p_x, p_y, \tau)\right.$$
$$\left. \times \sin(p_x x/\lambda_{\text{eff}})\cos(p_y y/\lambda_{\text{eff}})\right\}.$$

In this expression, the $\mathbf{H}_S(x, y, t)$ function is symmetric about the X- and Y-axes, whereas the $\mathbf{H}_A(x, y, t)$ function is symmetric about the Y-axis but antisymmetric about the X-axis. The formation of a region of inverted magnetic field (inversion wake) in the direction of Pearl vortex movement (X-axis) can be explained as follows. The positive contribution to the vortex magnetic field is dominated by the superposition of two positive maxima of functions $\mathbf{H}_S$ and $\mathbf{H}_A$, whereas the inversion wake is formed by the superposition of the positive maximum of function $\mathbf{H}_S$ and the negative minimum of function $\mathbf{H}_A$.

The value of $\chi_0 \propto 10^{-3}$–10^{-5} is typical of antiferromagnetics. The characteristic velocity $v_0 \propto Jsa(a/\lambda_{\text{eff}})$ is lower than the spin-wave velocity $v_s \propto Jsa$ by a factor of $(\lambda_{\text{eff}}/a) \propto 10^3$–$10^4$. The spin-wave velocity in the CuO_2 layers is rather high because of a strong intralayer exchange: $v_s \propto (0.5\text{–}1.3) \times 10^7$ cm/s [3]; i.e., $v_0 \propto 10^3$–10^4 cm/s. Note that the highest velocity experimentally observed for the moving Abrikosov vortices in bulky superconductors is of the same order: $v_A \approx 6.6 \times 10^3$ cm/s [21].

Numerical analysis showed that for $\chi_0 \approx 10^{-3}$–10^{-4} (this is comparable with the susceptibility of the copper subsystem in HTSC materials) and $\eta = 1$, the minimum of the magnetic-field distribution (inversion wake) at an arbitrary instant of time τ is situated on the X-axis at a distance of $x_0/\lambda_{\text{eff}} \propto 5$–$7$ behind the vortex and is of the order of $|H_{\min}(x_0/\lambda_{\text{eff}}, 0, \tau)|(\pi\lambda_{\text{eff}})^2/\Phi_0 \propto 10^{-3}$–$10^{-4}$.

For $\chi_0 \propto 10^{-2}$ (which is typical of the RE-containing ternary and HTSC compounds at temperatures near the magnetic ordering temperature $T_N \propto 1$ K) and $\eta = 1$, the inversion wake is also observed in the stationary magnetic-field distribution behind the moving Pearl vortex. Its minimum at $y = 0$ is of the order of $|H_{\min}(x_0/\lambda_{\text{eff}}, 0, \tau)|(\pi\lambda_{\text{eff}})^2/\Phi_0 \propto 10^{-2}$ and is situated on the X-axis at a distance of $x_0/\lambda_{\text{eff}} \propto 5$ from the vortex center. A typical distribution of the reduced magnetic field $H(x/\lambda_{\text{eff}}, 0,$

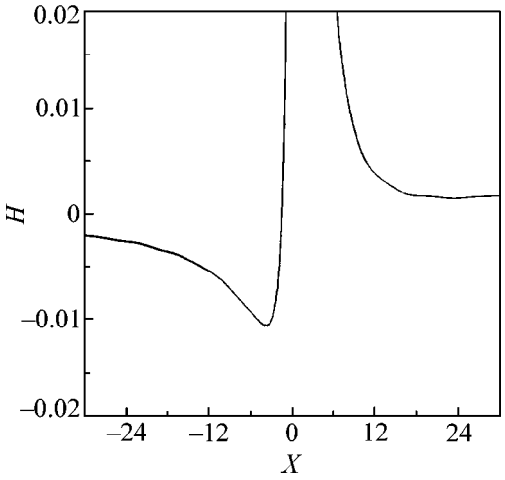

Figure.

$\tau = 1)(\pi\lambda_{eff})^2/\Phi_0$ over the $X = x/\lambda_{eff}$ variable is shown in the figure for $y = 0$, time $\tau = 1$, and the parameters listed above. In this figure, the dimensionless field in the maximum of distribution is of order 10. Note that the vortex is oblate along the *Y*-axis.

The vortex velocity v is much lower than the relaxation rate $\sim v_s$ of the magnetic subsystem. Consequently, the magnetic subsystem almost instantly follows the field of the moving vortex and renormalizes it by virtue of the time and spatial dispersion of magnetic permeability, giving rise to the inversion wake behind the vortex at large distances of the order of tens of λ_{eff} from its center.

The inversion of the magnetic field behind the vortex (inversion wake) is due to the spin-wave diffusion accompanying the process of medium (magnetic subsystem) polarization induced by the field of a uniformly moving solitary two-dimensional Pearl vortex.

It is known [22, 23] that the inversion of the longitudinal component of the magnetic field generates attractive forces between the vortices. For this reason, the vortices moving in thin films of magnetic superconductors will line up in chains. This phenomenon may have a drastic effect on the operation of the switching or memory devices based on the Pearl vortices.

The stationary or nonstationary domain structure, the cylindrical magnetic domain structure, the labyrinth structure of Bloch lines, and the structures of a moving vortex lattice or a moving solitary vortex are usually visualized at the surface of a specimen, e.g., in the magneto-optical experiments. For this reason, one may expect that, as distinct from the inversion wake of the Abrikosov vortex moving in a 3D magnetic superconductor (see [8]), the inversion wake phenomenon predicted in this work for the two-dimensional surface Pearl vortex moving in a 2D magnetic superconductor can easily be observed in the magneto-optical experiments with thin magnetic superconductor films.

I sincerely acknowledge Yu.E. Kuzovlev for stimulating discussions and assistance in numerical computations and A.N. Artemov and Yu.V. Medvedev for discussion of the results, attention, and assistance.

REFERENCES

1. A. I. Buzdin, L. N. Bulaevskiĭ, M. L. Kulich, and S. V. Panyukov, Usp. Fiz. Nauk **144**, 597 (1984) [Sov. Phys. Usp. **27**, 927 (1984)].
2. A. I. Buzdin and L. N. Bulaevskiĭ, Usp. Fiz. Nauk **149**, 45 (1986) [Sov. Phys. Usp. **29**, 412 (1986)].
3. Yu. A. Izyumov, N. M. Plakida, and Yu. N. Skryabin, Usp. Fiz. Nauk **159**, 621 (1989) [Sov. Phys. Usp. **32**, 1060 (1989)].
4. *Superconductivity in Ternary Compounds*, Vol. 2: *Superconductivity and Magnetism*, Ed. by E. Fisher and M. Maple (Springer, Heidelberg, 1982; Mir, Moscow, 1985), Vol. 2.
5. *Physical Properties of High Temperatute Superconductors*, Ed. by D. M. Ginsberg (World Sci., Singapore, 1989; Mir, Moscow, 1990), Chaps. 4 and 6.
6. A. A. Abrikosov, Zh. Éksp. Teor. Fiz. **32**, 1442 (1957) [Sov. Phys. JETP **5**, 1174 (1957)].
7. L. P. Gor'kov and N. B. Kopnin, Usp. Fiz. Nauk **116**, 413 (1975) [Sov. Phys. Usp. **18**, 496 (1975)].
8. V. N. Krivoruchko, Pis'ma Zh. Éksp. Teor. Fiz. **55**, 285 (1992) [JETP Lett. **55**, 284 (1992)].
9. J. Pearl, Appl. Phys. Lett. **5**, 65 (1964).
10. P. G. de Gennes, *Superconductivity of Metals and Alloys* (Benjamin, New York, 1966; Mir, Moscow, 1968), Chap. 3.
11. A. A. Abrikosov, *Fundamentals of the Theory of Metals* (Nauka, Moscow, 1987; North-Holland, Amsterdam, 1988), Chap. 18.
12. P. G. de Gennes and J. Matrikon, Rev. Mod. Phys. **36**, 45 (1964).
13. V. N. Krivoruchko and Yu. A. Dimashko, Sverkhprovodimost: Fiz., Khim., Tekh. **5**, 967 (1992).
14. E. B. Sonin, A. K. Tagantsev, and K. B. Traito, Phys. Rev. B **46**, 5830 (1992).
15. E. M. Lifshitz and L. P. Pitaevskiĭ, *Course of Theoretical Physics*, Vol. 5: *Statistical Physics* (Nauka, Moscow, 1978; Pergamon, New York, 1980), Chap. l.5.
16. H. Umezawa, H. Matsumoto, and M. Tachiki, *Thermo-Field Dynamics and Condensed States* (North-Holland, Amsterdam, 1982; Mir, Moscow, 1985), Chap. 11.
17. M. Tinkham, *Introduction to Superconductivity* (McGraw-Hill, New York, 1975; Atomizdat, Moscow, 1980), Chap. 5.
18. B. I. Halperin and P. C. Hohenberg, Phys. Rev. **188**, 898 (1969).
19. P. M. Richards and M. B. Salamon, Phys. Rev. B **9**, 32 (1974).
20. A. I. Buzdin, Pis'ma Zh. Éksp. Teor. Fiz. **40**, 193 (1984) [JETP Lett. **40**, 956 (1984)].
21. A. N. Samus', A. F. Popkov, V. I. Makhov, *et al.*, Sverkhprovodimost: Fiz., Khim., Tekh. **4**, 1324 (1991).
22. A. M. Grishin, A. Yu. Martynovich, and S. V. Yampol'skiĭ, Zh. Éksp. Teor. Fiz. **97**, 1930 (1990) [Sov. Phys. JETP **70**, 1089 (1990)].
23. A. I. Buzdin and A. Yu. Simonov, Zh. Éksp. Teor. Fiz. **98**, 2074 (1990) [Sov. Phys. JETP **71**, 1165 (1990)].

Translated by V. Sakun

JETP Letters, Vol. 71, No. 10, 2000, pp. 430–433. Translated from Pis'ma v Zhurnal Éksperimental'noĭ i Teoreticheskoĭ Fiziki, Vol. 71, No. 10, 2000, pp. 625–630.

CONDENSED MATTER

Behavior of Domain Structure in a Co/Ag Superlattice with Dispersion of Magnetic Anisotropy

L. M. Dedukh*, V. N. Matveev, and V. I. Nikitenko***

** Institute of Solid-State Physics, Russian Academy of Sciences, Chernogolovka, Moscow region, 142432 Russia*
e-mail: dedukh@issp.ac.ru
*** Institute of Microelectronic Technology and Ultrahigh-Purity Materials, Russian Academy of Sciences, Chernogolovka, Moscow region, 142432 Russia*

Received April 5, 2000; in final form, April 11, 2000

It is found that the magnetization reversal of an array of superthin Co films coupled by the ferromagnetic exchange interaction through the Ag layers may result in a domain structure of an unexpected new type. Due to the incoherent different-sense spin rotation upon lowering the field perpendicular to the easy axis, the specific macrodomains first form in a sample. They are separated not by the Neél domain wall but by a wide transition region containing high-density microdomains of sizes correlating with the grain sizes in the films. Further magnetization reversal proceeds through the formation of standard domain walls in the macrodomain in a magnetostatic field at the plate edge and through their shifting toward the transition region. These processes are explained with taking into account the character of the revealed magnetic anisotropy dispersion. © *2000 MAIK "Nauka/Interperiodica".*

PACS numbers: 75.70.Cn; 75.60.Ch

It is known that real magnetics inevitably contain lattice defects generating internal microstresses and microdisorientations in samples. They may combine to form macrostresses in equilibrium at distances on the order of the sample size or to form disoriented macroscopic crystal domains, such as diversified grain boundaries, textures, etc. In layered systems, macrostresses and crystallographic disorientations often arise because of a mismatch between the lattice parameters of the neighboring layers. This all produces disorientation of the easy magnetic axes (EMAs) in different crystal regions and gives rise to the anisotropy dispersion on different scales. The influence of the dispersion on the characteristics of hysteresis loops began to be studied long ago [1].

In recent years, increased interest has been demonstrated in multilayer films composed of alternating layers with different magnetic order. They exhibit a number of unique properties (giant magnetoresistance, unidirectional anisotropy, etc.) that can be used in solving problems of great practical importance and that are largely caused by the unusual behavior of the domain structure in such materials [2–4]. This behavior is strongly governed by the character of the anisotropy field. For this reason, gaining information about the influence of anisotropy dispersion on the elementary events of magnetization processes in multilayer structures is among the most important problems of this intensively developing field of fundamental and applied investigations. The results of such investigations are presented below.

A one-dimensional superlattice of 150 alternating Co and Ag layers, each 9 Å thick, was grown on an ALCATEL setup at a pressure of 7×10^{-5} mbar (Ar) by magnetron (Co) and cathode (Ag) sputtering onto a SiO_2/Si substrate at 77 K. The domain structure was studied using the magneto-optical indicator film technique [5]. A single-crystal garnet ferrite film with magnetization lying in its plane was used as an indicator film. It was placed immediately on a sample under study. The stray fields at its edges, the domain walls, and the lattice defects induced local deviations of magnetization from the indicator film plane. The deviations were detected using the double Faraday effect in the polarized light reflected from the aluminum-coated bottom surface of the film.

The magnetization reversal in different directions showed that the Co/Ag superlattice possesses an unusual, though well-defined, uniaxial anisotropy: its dispersion is responsible for the small-angle (~2°) random EMA deviations in micrograins and for an additional smooth easy-axis rotation (within 14°) across the whole superlattice sample of size 2 mm studied. The sample magnetized to saturation in the EMA direction remained single-domain after switching off the external field. On a subsequent change in the sign of external field (H), the domain walls arose at the sample edges in the region of maximum magnetostatic fields (Fig. 1a). The displacement of the walls brought about magnetization reversal of the whole sample. Due to the macroscopic anisotropy dispersion, the domain walls were curvilinear. As H departed from the EMA, the magne-

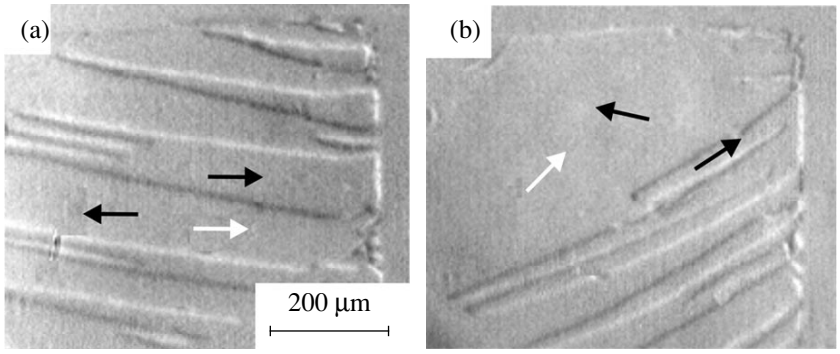

Fig. 1. Domain structures arising in the Co/Ag superlattice upon the magnetization reversal in the inverted field (a) directed along the EMA (H = –40 Oe) and (b) forming an angle of 45° with the EMA (H = –45 Oe). The white arrows indicate the direction of the inverted field, and the black arrows indicate the magnetization direction.

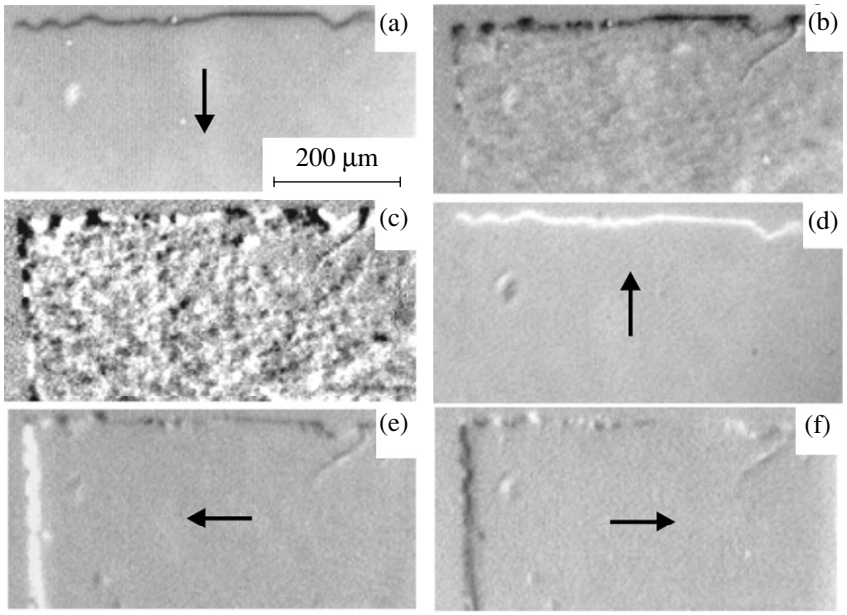

Fig. 2. Magneto-optical images of the Co/Ag superlattice magnetized along the mean HMA direction (a, d) to saturation at H = (a) 200 and (d) –200 Oe, (b) in a weak field of H = 40 Oe, and (c) after switching off the field; (e, f) photographs obtained after switching off the field (H = –200 Oe) preliminarily turned through an angle of (e) –1° and (f) +1° from the mean HMA.

tization rotation processes began to play an increasingly important role, causing a gradual change in the mutual arrangement of magnetization in the domains (Fig. 1b). The sense of elongation of tapered domains and the curvature of domain walls between them also markedly changed.

A different type of domain structure was observed in the Co/Ag superlattice upon magnetization reversal in the direction of a hard magnetic axis (HMA) perpendicular to the EMA. This process is imaged in Figs. 2a–2c for one of the superlattice corners. Figure 2a is its magneto-optical image under the conditions of magnetization to saturation in the HMA direction, which is parallel to the vertical frame of the picture. The horizontal dark stripe is due to the magnetostatic fields that arose at the sample edge perpendicular to the magnetization M and were exposed by Faraday rotation with slightly uncrossed nicols of a microscope. The vertical edge (parallel to M) of the superlattice is not seen in Fig. 1a. The changes occurring in the magnetostatic field contrast at the edges of the sample and its center upon decreasing H (Fig. 2b) give evidence for the process of incoherent rotation of the M vectors. It resulted in a microdomain structure (Fig. 2c) drastically different from the aforementioned standard structure with the edge domains separated by the domain walls, as exem-

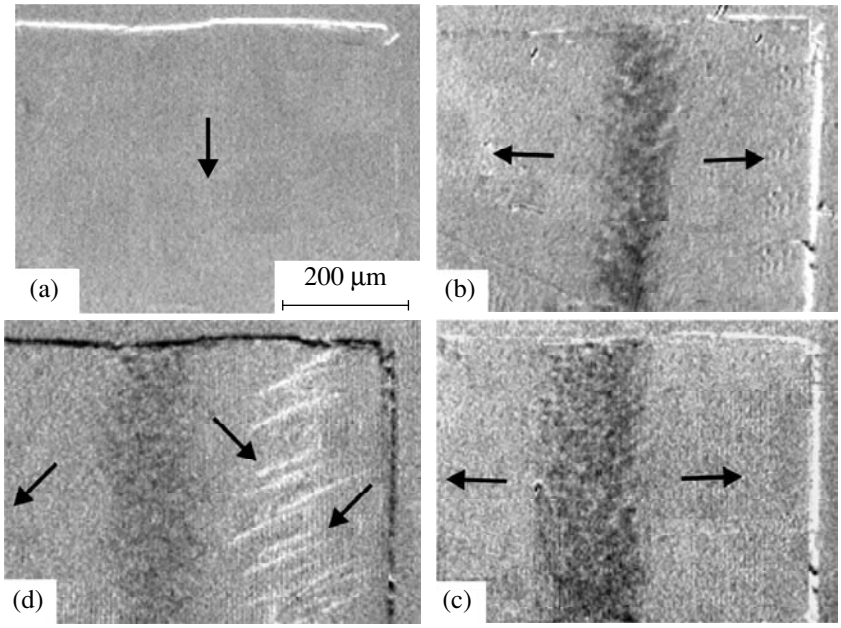

Fig. 3. Photographs of the superlattice with a gradient of the EMA "skew" angle: (a) system is magnetized along the mean HMA at $H = 800$ Oe and (b) after switching off the field; (c) change in the magnetization distribution after switching off the field preliminarily turned through an angle of +1° from its initial direction; (d) domain structure after the subsequent change in sign of the field ($H = -60$ Oe).

plified in Fig. 1. The sizes of the resulting microdomains correlate with the grain sizes in the superlattice cell substructure, which is easily exposed in the light reflected from the superlattice surface. On a subsequent change in the sign of H and its increase, the magneto-optical contrast associated with the microdomains gradually faded. The image of the superlattice magnetized in the direction opposite to that in Fig. 2a is shown in Fig. 2d.

When the field H deviated from the HMA by an angle larger than ±1°, the decrease in its magnitude induced coherent rotation of magnetization clockwise or counterclockwise in this region of the sample, giving rise to stray fields and intensifying a uniform magneto-optical contrast at the vertical edge of the superlattice. Such a uniform rotation of M upon reducing H to zero resulted in a homogeneous magnetization of the system parallel to the EMA (Figs. 2e, 2f).

A small-scale anisotropy dispersion caused by weak (within one degree) random deviations of the EMAs in the grains of the multilayer system from the mean direction specified by the growth-induced anisotropy has a crucial effect on the formation of the above-mentioned microdomain structure in the course of magnetization reversal along the HMA of the superlattice. With H parallel to HMA, the magnetization reversal was accounted for by the different-sense rotations of M in the grains whose EMAs were oppositely directed relative to the direction of the external magnetic field. This gave rise to the microdomains.

A smooth and appreciable (up to 14°) change in the easy-axis orientation across the whole sample in the direction of mean EMA resulted, upon magnetization reversal in the perpendicular direction, in a quite unusual, and as yet theoretically not considered, domain structure. Apart from the microdomain structure in the crystal regions where the local HMA deviated from H by small angles (less than 1°) of opposite signs, the macroscopic domains were also formed in the neighboring large crystal volumes as a result of the quasi-uniform different-sense rotations of M (Fig. 3b). The deviations of the local HMAs in these macrodomains were of the same sign, but the farther the macrodomain from the microdomain region the larger the deviation. The macrodomains were separated not by the usual domain wall but by a wide transition region with a high concentration of microdomains (Fig. 3b) identical to those shown in Fig. 2c. Upon the rotation of H in the film plane and its subsequent decrease from saturation, the transition region was exposed in a new region of the sublattice (Fig. 3c), where the mean HMA direction was parallel to the new H direction.[1]

[1] Hence, not only the EMA "skew" angle can be measured but the arrangement of the EMA directions in the superlattice plane can also be determined by monitoring the angle of H rotation. In particular, a gradual movement of the transition region between the macrodomains across the sample (2 mm in size) corresponded to the H rotation through 14°. The angle between the mean EMA directions in the portions of neighboring macrodomains shown in Figs. 3b and 3c is equal to 176°.

After a change in the H sign, the magnetization reversal of the macrodomains in a slowly increasing field of opposite polarity was caused not only by the M rotation but also by the creation and growth of the standard tapered domains separated by charged domain walls. These tapered domains arose in the magnetostatic field at the sample edges after the preliminary spin rotation through a large angle in the macrodomain and merged to form a single new macrodomain with the same longitudinal magnetization as in the initial macrodomain but opposite transverse magnetization (Fig. 3d).

The reason for the formation of a macroscopic domain structure upon magnetization reversal in a field perpendicular to the easy axis of a particular superlattice region is associated with the dispersion of the growth-induced anisotropy, which causes a smooth change in the EMA orientation across the whole sample. In the case considered, the angles measured between the easy axes in the center of the sample and at its edges were found to be ±7°. As the departure of H from the average HMA direction exceeded ±7°, macrodomains with an unusual transition region between them did not arise. The whole sample was remagnetized as a result of the M rotation and the appearance and growth of the domains separated by the standard domain walls (see Fig. 1).

It is known that spins necessarily rotate upon a decrease in the field that preliminarily magnetized a uniaxial magnetic parallel to the HMA. In a perfect magnetic, these processes may proceed coherently in either of the senses: clockwise or counterclockwise. The anisotropy dispersion at micro- and macroscopic distances removed this degeneracy in the sample studied. The random scatter of the small-angle (±1°) EMA deviations from the H direction resulted in incoherent spin rotation in the grains to form microdomains. The macroscopic dispersion dictated the opposite senses of spin rotation in the macroscopic volumes adjacent to the region with microdomains. As the result, the macrodomains were separated not by the Neél domain wall but by the transition region with a high concentration of microdomains.

Thus, macrodomains separated by a fixed transition region with a high concentration of microdomains arose at the stage of H decrease every half-period of an alternating field (pulsed, sinusoidal, or arbitrarily varying with time) with a sufficiently large amplitude. After changing sign of the field and a rise in its magnitude, a mobile domain wall grew in the macrodomain. The subsequent displacement of the wall to the transition region up to their annihilation resulted in magnetization reversal of the macrodomain. The magnetization reversal of the whole sample was completed by adjusting the M vectors to the H direction across the whole sample.

REFERENCES

1. M. Prutton, *Thin Ferromagnetic Films* (Butterworths, London, 1964; Sudostroenie, Leningrad, 1967).
2. J. B. Kortright, D. D. Awschalon, J. Stohr, *et al.*, J. Magn. Magn. Mater. **207**, 7 (1999).
3. A. E. Berkowitz and K. Takano, J. Magn. Magn. Mater. **200**, 552 (1999).
4. B. Heinrich and J. F. Cochran, Adv. Phys. **42**, 523 (1993).
5. L. M. Dedukh, V. S. Gornakov, Yu. P. Kabanov, *et al.*, Pis'ma Zh. Éksp. Teor. Fiz. **64**, 778 (1996) [JETP Lett. **64**, 826 (1996)].

Translated by V. Sakun

JETP Letters, Vol. 71, No. 10, 2000, pp. 434–437. Translated from Pis'ma v Zhurnal Éksperimental'noĭ i Teoreticheskoĭ Fiziki, Vol. 71, No. 10, 2000, pp. 631–636.

CONDENSED MATTER

Transport Properties of a GaAs/AlGaAs Ring Interferometer in the Tunneling Regime

A. A. Bykov*, D. G. Baksheev*, L. V. Litvin*, V. P. Migal'*, E. B. Ol'shanetskiĭ*, M. Cassé, D. K. Maude**, and J. C. Portal**, ***, ******

** Institute of Semiconductor Physics, Siberian Division, Russian Academy of Sciences, pr. Akademika Lavrent'eva 13, Novosibirsk, 630090 Russia*

e-mail: bd@isp.nsc.ru

*** CNRS-LCMI, F-38042, Grenoble, France*

**** Institute National des Sciences Appliquées, Toulouse 31077, France*

***** Institute Universitaire de France, Paris, France*

Received March 23, 2000; in final form, April 20, 2000

The transport properties of GaAs/AlGaAs submicron rings with split gates in the conditions corresponding to the ring resistance $R_{SD} > h/e^2$ are studied. Oscillations of R_{SD} as a function of the gate voltage V_G are experimentally observed. The oscillations are caused by the single-electron charging of two triangular conducting regions into which the ring is divided in the tunneling regime. © *2000 MAIK "Nauka/Interperiodica".*

PACS numbers: 73.23.-b; 73.40.Gk

Although the first fundamental experiments aimed at studying the charge carrier transport processes in mesoscopic systems were performed on submicron metal cylinders [1] and rings [2–4], a considerable part of the experimental data in this area of research were obtained from the studies of the coherent properties of electron interferometers fabricated on the basis of GaAs/AlGaAs heterojunctions [5–13]. By now, the coherent transport processes in such interferometers have been well studied for rings in the metallic conduction regime, while the transport properties of semiconductor rings in the tunneling regime remain poorly understood. The main distinction between the GaAs/AlGaAs and the metal rings consists in the fact that the dimensions of the conducting regions of a semiconductor interferometer are determined not only by the lithography but also by the depletion regions that are formed along the boundaries of the conducting channels, while, in metal ring interferometers, such depletion regions are absent. Figure 1 schematically represents a ring with a split gate ($G1$ and $G2$) and the depletion regions. The dashed lines show the geometry of the conducting regions of the interferometer in the metallic conduction regime [14]. This geometry is supported by the self-consistent calculations of the electrostatic potential and the electron density for a similar interferometer [15]. As the conduction regime in a GaAs/AlGaAs ring changes from metallic (the ring resistance is $R_{SD} < h/e^2$) to the tunneling regime ($R_{SD} > h/e^2$), the depletion regions belonging to the opposite sides of the conducting regions merge in the narrowest conducting areas, resulting in the formation of nonconducting bridges. One can see that, in this case, the ring is divided by four tunneling gaps into two triangular conducting regions located at the ring splitting points. The role of these regions in the interference processes that occur in the conditions of the tunneling-coupled edge current states was mentioned earlier [16], but no reliable experimental proof has been obtained for the conducting region geometry presented in Fig. 1. This paper reports the observation of single-electron oscillations in the resistance of GaAs/AlGaAs rings, which experimentally confirms the fact that, in the tunneling regime, the ring is divided into two conducting regions whose area is an order of magnitude less than the effective area of the ring interferometer.

The rings studied in the experiment were fabricated on the basis of a GaAs/AlGaAs heterojunction with the use of electron-beam lithography and dry etching. The 2D electron gas that was formed in the initial GaAs/AlGaAs heterojunction grown by molecular beam epitaxy had the following parameters after illumination at $T = 4.2$ K: the electron concentration $n_s = 1.45 \times 10^{12}$ cm^{-2} and the mobility $\mu = 3.4 \times 10^4$ cm^2/(V s) (the spacer thickness was 3 nm). A ring with the effective radius $r_{\text{eff}} = 0.12$ μm, which was determined from the period of h/e oscillations, was studied in detail. For a ring with $r_{\text{eff}} = 0.2$ μm, a qualitatively similar behavior was observed. The experiments were performed at temperatures from 0.1 to 40 K in magnetic fields up to 15 T. The two-terminal resistance of the rings was measured by a phase-sensitive amplifier at alternating current frequencies from 7 to 800 Hz, with the source–drain voltage not exceeding kT/e. The experimental data presented below were obtained for the ring with

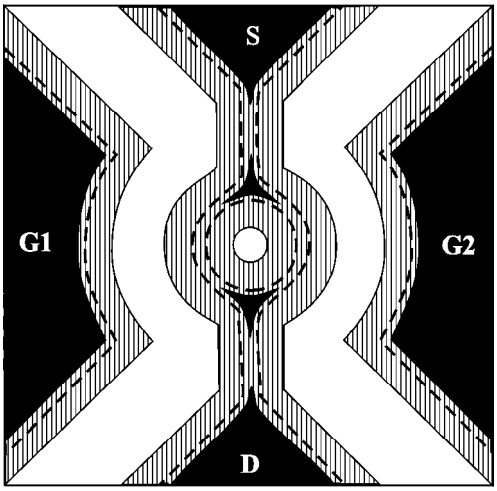

Fig. 1. Schematic diagram of a GaAs/AlGaAs ring with a split gate in the tunneling regime. The dark areas represent the 2D electron gas, the gray areas show the depletion regions, and the white areas are the etch regions. The dashed lines show the ring geometry in the metallic conduction regime.

the smaller radius whose schematic view is presented in Fig. 1.

Figure 2a shows the characteristic dependences of the ring resistance R_{SD} on the gate voltage V_G simultaneously applied to both parts of the gate. The dependence $R_{SD}(V_G)$ exhibits large-scale oscillations with a quasi-period of 40–60 mV and small-scale oscillations with the characteristic period ΔV_G = 5–6 mV. The large-scale oscillations were observed up to the temperatures 30–40 K, and their position and amplitude depended on the magnetic field strength. The small-scale oscillations disappeared at temperatures above 10 K, and their period remained constant in magnetic fields up to 15 T.

In the tunneling regime, as well as in the metallic conduction regime, the magnetoresistance of the ring (Fig. 2b) exhibits *h*/*e* oscillations whose period corresponds to a single-quantum variation in the magnetic flux through a circular area of radius $r_{\text{eff}} = 0.12$ μm. The observation of the Aharonov–Bohm oscillations testifies that, in the conditions $R_{SD} > h/e^2$, the electron transport in the ring possesses an interference component, as was observed earlier for an electron interferometer with a quantum dot in one of its channels [11].

One of the possible mechanisms that may be responsible for the periodic oscillations observed in the $R_{SD}(V_G)$ dependences is the resonance tunneling of charge carriers through the one-dimensional levels of a ring which is weakly coupled to the source and the drain [17]. In this case, for two-terminal resistance, one should observe the effect of the gate voltage V_G on the amplitude of the *h*/*e* oscillations within a half-period equal to $\Delta V_G/2$ = 2.5–3 mV. Figure 3 presents the dependences $R_{SD}(V_G)$ and $R_{SD}(B)$ on the intervals of V_G and B on which the oscillation amplitudes are comparable. These dependences show that the aforementioned effect is absent. For different gate voltages, the dependences of the resistance on magnetic field are only shifted relative to each other without any changes in the amplitude of the *h*/*e* oscillations. This result allows us to conclude that, in the GaAs/AlGaAs interferometers under study, the model of a ring weakly coupled to the source and the drain [17] is not realized. If we assume that, in the regime $R_{SD} > h/e^2$, the ring is divided in two conducting regions (lakes) coupled by tunneling with each other, as well as with the source and the drain (according to the geometry of the system), the observed periodic oscillations of the ring resistance as a function of the gate voltage can be explained by a single-electron charging of these lakes. This assumption is confirmed by the observation of spontaneous switching of the ring resistance with the accompanying jumplike phase shifts in the oscillations of $R_{SD}(V_G)$. Such behavior is characteristic of single-electron oscillations and is related to the fluctuations of the "telegraph noise" type in the polarization of the Coulomb islands. In our case, the switching may occur as a result of the uncontrolled recharging of an impurity atom in the doping layer separated from the conducting channel by a relatively thin spacer. In contrast to such behavior,

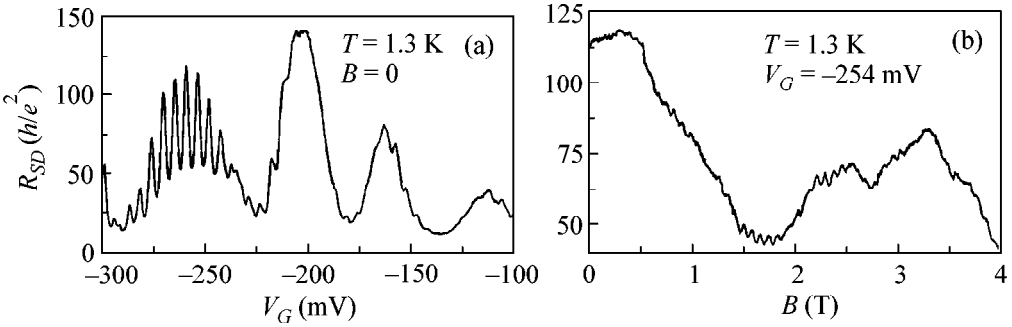

Fig. 2. The $R_{SD}(V_G)$ and $R_{SD}(B)$ dependences at T = 1.3 K. (a) B = 0; (b) V_G = –254 mV.

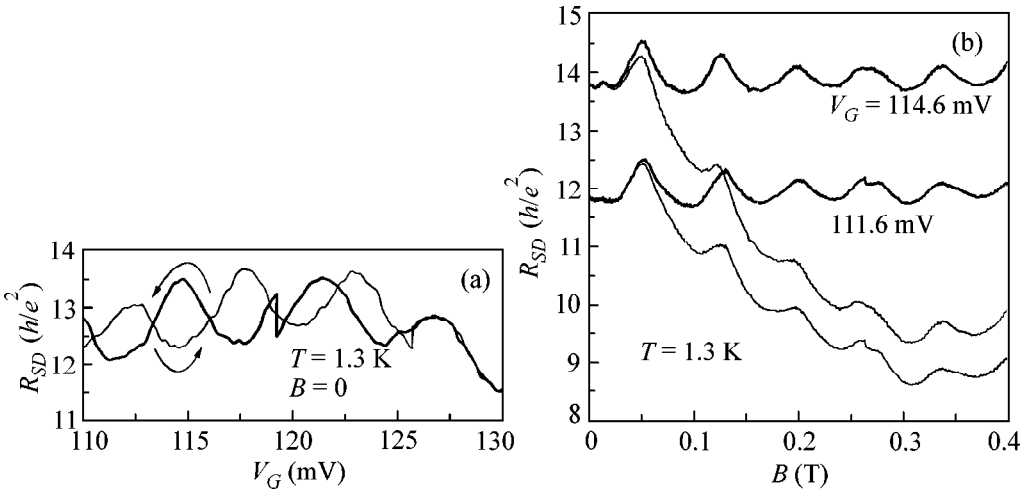

Fig. 3. The $R_{SD}(V_G)$ and $R_{SD}(B)$ dependences at T = 1.3 K. (a) The thin and thick lines correspond to different directions of the V_G sweep at B = 0. (b) The upper curve is for V_G = 114.6 mV, and the lower curve is for V_G = 111.6 mV. The thin lines correspond to the experimental dependences, and the thick lines correspond to the dependences with the subtracted monotonic component.

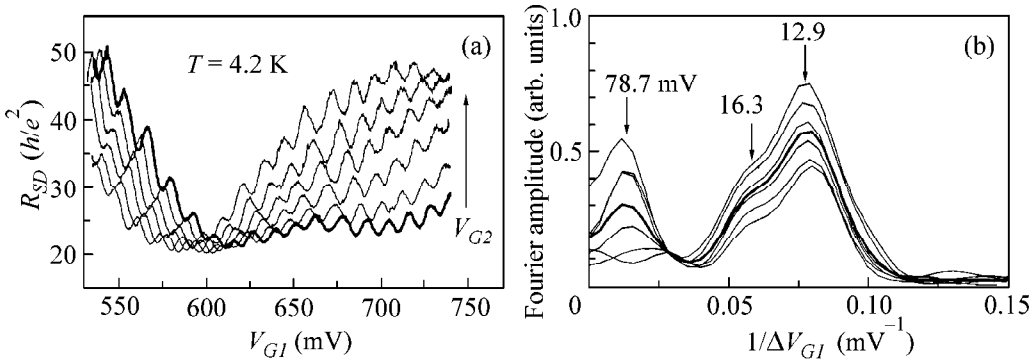

Fig. 4. (a) The $R_{SD}(V_G)$ dependences at T = 4.2 K for different values of V_{G2}. (b) The thin lines show the dependences of the Fourier amplitude on $1/\Delta V_{G1}$ for the experimental curves presented in plot (a); the thick line shows the average dependence.

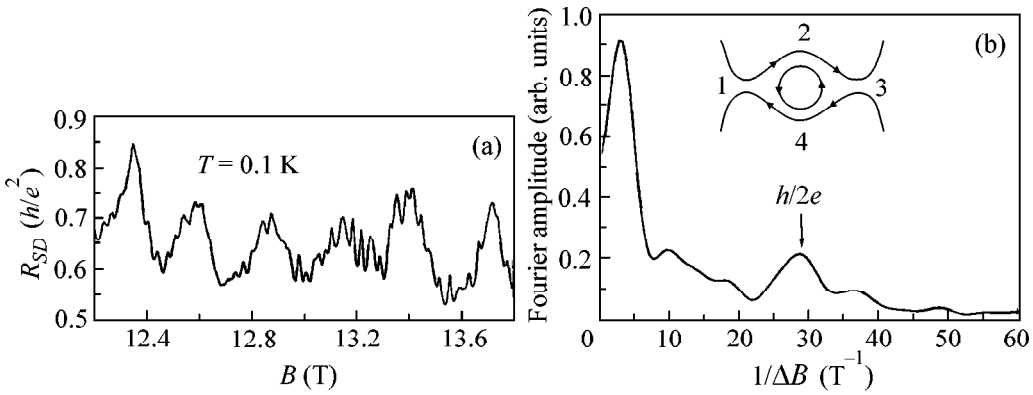

Fig. 5. (a) The $R_{SD}(B)$ dependence in the conditions of tunneling-coupled edge current states at T = 0.1 K. (b) Dependence of the Fourier amplitude on $1/\Delta B$. The inset schematically represents the edge current states.

for insignificant switchings of the ring states, the amplitude of the h/e oscillations remained constant within the experimental error.

Figure 4a presents the dependences of R_{SD} on the voltage V_{G1} applied to one part of the gate, with different voltages V_{G2} applied to the other part. As one would expect, in this case, the period of the single-electron oscillations increased by a factor of two as compared to the situation with the same voltage simultaneously applied to both parts of the gate. The geometry of Fig. 1 for the conducting regions of the ring in the tunneling regime is experimentally supported by the results of the Fourier analysis of single-electron oscillations. These results are presented in Fig. 4b. Two pronounced peaks corresponding to single-electron charging of each of the two electron lakes are observed. In the framework of this model, the aperiodic fluctuations in the $R_{SD}(V_G)$ dependences can be caused by the resonance tunneling of charge carriers through the localized states of the electron lakes. However, for an unambiguous interpretation of these fluctuations, additional experimental studies and their comparison with the theory are necessary.

Figure 5a displays the dependence of R_{SD} on magnetic field in the conditions of tunneling-coupled edge current states. The Fourier analysis of this dependence yields two peaks (Fig. 5b), one of which corresponds to the period of the $h/2e$ oscillations, and the other corresponds to a period that is an order of magnitude greater. Although qualitatively similar dependences of the resistance on magnetic field in the conditions of tunneling-coupled edge current states were observed earlier [16], no convincing interpretation of the experimental data was provided. The inset in Fig. 5b schematically represents the current states that correspond to the topology of the conducting regions of the ring. Four regions of the exchange between the edge current states are present, and they are located in the narrowest areas of the interferometer. In the framework of this model, the appearance of $h/2e$ oscillations is related to the tunneling of electrons with different spins through the internal closed state of the ring [18, 19], and the greater period oscillations can only be attributed to the area of the triangular conducting regions located at the ring splitting points. Then, the area of these regions should be a factor of 5–10 less than the effective area of the interferometer, which is quite admissible with allowance for the fabrication tolerances of electron lithography and correlates well with the ring micrographs obtained by a scanning electron microscope.

Thus, it is experimentally established that the transport properties of GaAs/AlGaAs rings in the tunneling regime are determined by two triangular conducting regions located at the splitting points of the electron channels of the interferometer. It is shown that, in the conditions $R_{SD} > h/e^2$, the Aharonov–Bohm oscillations coexist with single-electron oscillations of the ring conductivity.

The authors are grateful to O. Tkachenko, V. Tkachenko, and G. Gusev for useful discussions.

This work was supported by the Russian Foundation for Basic Research (project no. 98-02-17921), the International Program in Science and Technology "Physics and Technology of Nanostructures" (grant no. 99-1132), and the International Program in Science and Technology "Micro- and Nanoelectronics" (grant no. 02.04.5.1).

REFERENCES

1. D. Yu. Sharvin and Yu. V. Sharvin, Pis'ma Zh. Éksp. Teor. Fiz. **34**, 285 (1981) [JETP Lett. **34**, 272 (1981)].
2. R. A. Webb, S. Washburn, S. P. Umbach, *et al.*, Phys. Rev. Lett. **54**, 2696 (1985).
3. A. D. Benoit, S. Washburn, C. P. Umbach, *et al.*, Phys. Rev. Lett. **57**, 1765 (1986).
4. S. Washburn, H. Schmid, D. Kern, *et al.*, Phys. Rev. Lett. **59**, 1791 (1987).
5. G. Timp, A. M. Chang, J. E. Cunningham, *et al.*, Phys. Rev. Lett. **58**, 2814 (1987).
6. P. G. N. de Vegvar, G. Timp, *et al.*, Phys. Rev. B **38**, 4326 (1988).
7. C. J. B. Ford, T. J. Thornton, R. Newbury, *et al.*, Appl. Phys. Lett. **54**, 21 (1989).
8. K. Ismail, S. Washburn, and K. Y. Lee, Appl. Phys. Lett. **59**, 1998 (1991).
9. J. Liu, W. X. Gao, K. Ismail, *et al.*, Phys. Rev. B **48**, 15148 (1993).
10. A. A. Bykov, Z. D. Kvon, L. V. Litvin, *et al.*, Pis'ma Zh. Éksp. Teor. Fiz. **58**, 538 (1993) [JETP Lett. **58**, 543 (1993)].
11. A. Yacoby, M. Heiblum, H. Shtrikman, *et al.*, Phys. Rev. Lett. **74**, 4047 (1995).
12. R. Shuster, E. Buks, M. Heiblum, *et al.*, Nature (London) **385**, 417 (1997).
13. S. Pedersen, A. E. Hansen, A. Kristensen, *et al.*, Phys. Rev. B **61**, 5457 (2000).
14. T. Nakanishi and T. Ando, Phys. Rev. B **54**, 8021 (1996).
15. O. A. Tkachenko, V. A. Tkachenko, D. G. Baksheev, *et al.*, Pis'ma Zh. Éksp. Teor. Fiz. **71**, 366 (2000) [JETP Lett. **71**, 255 (2000)].
16. A. A. Bykov, Z. D. Kvon, E. B. Ol'shanetskiĭ, *et al.*, Pis'ma Zh. Éksp. Teor. Fiz. **58**, 897 (1993) [JETP Lett. **58**, 839 (1993)].
17. W.-C. Tan and J. C. Inkson, Phys. Rev. B **53**, 6947 (1996).
18. C. J. B. Ford *et al.*, Phys. Rev. B **49**, 17456 (1994).
19. M. Kataoka, C. J. B. Ford, G. Faini, *et al.*, Phys. Rev. Lett. **83**, 160 (1999).

Translated by E. Golyamina

JETP Letters, Vol. 71, No. 10, 2000, pp. 438–441. Translated from Pis'ma v Zhurnal Éksperimental'noĭ i Teoreticheskoĭ Fiziki, Vol. 71, No. 10, 2000, pp. 637–642.

CONDENSED MATTER

μ^-Spin Rotation Study of the Temperature-Dependent Relaxation Rate of Acceptor Centers in Silicon

T. N. Mamedov*, D. G. Andrianov, D. Gerlach***, K. I. Gritsaĭ*, V. N. Gorelkin****, O. Cormann*****, J. Major*****, ******, A. V. Stoĭkov*, M. Shevchik******, and U. Zimmerman*****

* *Joint Institute for Nuclear Research, Dubna, Moscow region, 141980 Russia*
e-mail: tmamedov@nu.jinr.ru
** *State Research Institute for the Rare-Metals Industry "GIREDMET," Moscow, 109017 Russia*
*** *Paul Scherrer Institut, CH-5232 Villigen PSI, Switzerland*
**** *Moscow Institute of Physics and Technology, Institutskiĭ per. 9, Dolgoprudnyĭ, Moscow region, 141700 Russia*
***** *Max-Planck-Institut für Metallforschung, D-70569 Stuttgart, Germany*
****** *Universität Stuttgart, Institut für Theoretische und Angewandte Physik, D-70569 Stuttgart, Germany*
Received April 13, 2000

Temperature-dependent remanent polarization of negative muons in a silicon crystal doped with phosphorus (3.2×10^{12}, 2.3×10^{15}, and 4.5×10^{18} cm^{-3}) and aluminum (2×10^{14} and 2.4×10^{18} cm^{-3}) was examined. Measurements were made over the temperature range 4–300 K in a magnetic field of 2000 G perpendicular to the muon spin. Temperature dependence of the relaxation rate was determined for the magnetic moment of a shallow Al acceptor center in a nondeformed silicon sample, and the hyperfine interaction constant was estimated for the interaction between the magnetic moments of muon and electron shell of the muonic μAl atom in silicon.

PACS numbers: 76.75.+i

Unlike shallow donor centers, shallow acceptors in semiconductor crystals with diamond structure have been adequately studied neither theoretically nor experimentally [1]. For instance, different theoretical calculations predict different ground-state energies for the shallow acceptors in Si, GaP, or InP semiconductors (see [2–4]). Only a few experimental works are known in which the shallow acceptor centers in silicon were studied by electron paramagnetic resonance (EPR) [5–8].

It was demonstrated both theoretically [9] and experimentally [10–13] that the negative-muon spin rotation (μ^-SR) method is suitable for studying the behavior of acceptor centers in semiconductors and that the results of these studies can materially supplement the data obtained by the other nuclear physical methods.

The behavior of the polarization of a negative muon in silicon depends on the charge state of an acceptor center formed through muon capture by the silicon atom. Since silicon is a diamagnetic substance (the influence of the nonzero nuclear magnetic moment of the Si^{29} isotope is negligible), the polarization vector of the ionized (diamagnetic) acceptor center placed in an external magnetic field perpendicular to the muon spin should execute undamped precession at a free-spin frequency. In the neutral (paramagnetic) state, the precession may relax and its frequency may shift due to the interaction between the magnetic moments of muon and acceptor electron shell. The magnetic moment of a shallow acceptor in silicon is specified by the quantum number $j = 3/2$ [14]. Analytic expressions for the polarization of the negative muon were derived by Gorelkin *et al.* in [15] for the $j \geq 1$ case. On the assumption that the relaxation rate (ν) of the electronic magnetic moment far exceeds the hyperfine interaction constant (A_{hf}) for the interaction between the magnetic moments of muon and electron shell, the frequency shift ($\Delta\omega$ and the relaxation rate (λ) of muon spin depend on A_{hf} and ν as [15]

$$\frac{\Delta\omega}{\omega_0} = \frac{g\mu_B}{2\mu_B}\frac{j(j+1)\hbar A_{hf}}{3k_BT} + \frac{A_{hf}^2}{2(\nu^2+\omega_e^2)}, \quad (1)$$

$$\lambda = \frac{j(j+1)}{3}\left(\frac{A_{hf}^2}{\nu} + \frac{A_{hf}^2\nu}{\nu^2+\omega_e^2}\right), \quad (2)$$

where $\Delta\omega = \omega(T) - \omega_0$ (ω_0 is the angular frequency of muon precession in the diamagnetic state of a muonic atom); $h = 2\pi\hbar$ is the Planck constant; k_B is the Boltzmann constant; μ_B and μ_μ are the Bohr and muonic magnetons, respectively; g is the acceptor g factor; and $\omega_e = g\mu_B B/\hbar$ is the angular frequency of the precession executed by the electronic magnetic moment in the external magnetic field B.

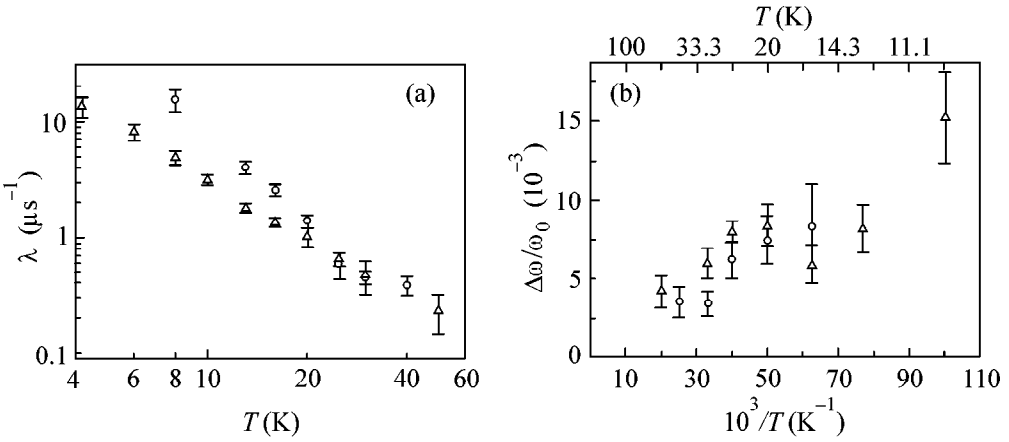

Fig. 1. Temperature-dependent (a) relaxation rate of muon spin and (b) frequency shift of muon spin precession in silicon samples with different concentrations of aluminum impurity: (○) 2×10^{14} cm^{-3} and (△) 2.4×10^{18} cm^{-3}.

With $j = 1/2$, Eqs. (1) and (2) coincide with the well-known formulas for a positive muon in a muonium atom (see, e.g., [16]).

This work reports results of the μ⁻SR studies for five silicon single-crystal samples [three *n*-type samples doped with phosphorus (3.2×10^{12}, 2.3×10^{15}, and 4.5×10^{18} cm^{-3}) and two *p*-type samples doped with aluminum (2×10^{14} and 2.4×10^{18} cm^{-3})].

Measurements were performed on a "Stuttgart μSR Spectrometer" apparatus [17] placed at the μE4 muon channel of the proton accelerator of the Paul Scherrer Institut (Switzerland). A spin-transverse external magnetic field of 2000 G was created in the samples by Helmholtz coils. The sample temperature was maintained to within 0.1 K in the range 4.2–300 K. The time-channel width of the spectrometer was 0.625 ns, and the total number of channels in the spectrum was 16000.

The procedure of reconstructing the polarization function for negative muons from the experimental μ⁻SR spectra is described in detail in [13]. The experimental data were used to determine the temperature dependences of the muon spin relaxation rate and frequency shift for the relaxing polarization component. In the case that both relaxing and nonrelaxing components were observed, their relative amplitudes and the acceptor ionization ($_\mu Al^0 \longrightarrow {}_\mu Al^-$ transition) rate were also determined.

The experimentally measured temperature dependences of the muon spin relaxation rate are presented in Figs. 1 and 2 for two aluminum-doped silicon samples and one phosphorus-doped sample (4.5×10^{18} cm^{-3}), respectively. Both relaxing and nonrelaxing components were observed for the muon spin precession at $T \lesssim 30$ K in silicon with a high concentration of phosphorus impurities (4.5×10^{18} cm^{-3}), as was observed earlier [13] for an antimony-doped (2×10^{18} cm^{-3}) sample. Accordingly, in addition to $\Delta\omega$ and λ, the acceptor ionization rate ν_{tr} was also determined from the experimental data for this sample. The resulting temperature-dependent ν_{tr} is shown in Fig. 2. For all remaining samples, including those with a high concentration of aluminum impurities (2×10^{18} cm^{-3}), only the relaxing polarization component was observed for the muon spin at $T < 50$ K. In this case, the zero-time precession amplitude corresponded to its room-temperature value.

The temperature dependence of the frequency shift is not contradictory to the Curie law $1/T$ for any of the samples studied (see, e.g., Fig. 1). This implies that the second term in Eq. (1) for the frequency shift is small compared to the first paramagnetic term. Ignoring the second term in Eq. (1), one can estimate the A_{hf} value from the experimental data for $\Delta\omega/\omega_0$ (the g factor is equal to 1.07 [8]). The resulting $A_{hf}/2\pi$ values were found to be approximately the same and equal to $\approx 3 \times 10^7$ s^{-1} for all samples. It should be noted that this

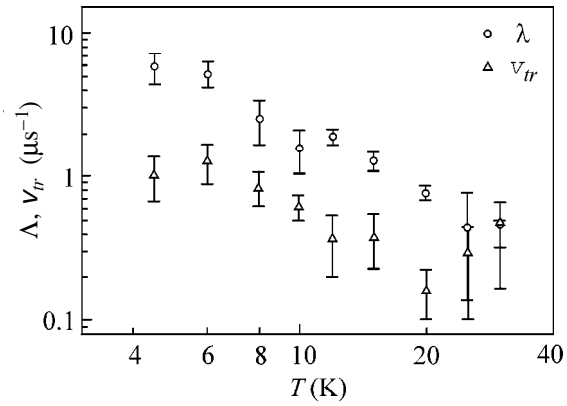

Fig. 2. Temperature-dependent (○) relaxation rate λ of muon spin in the paramagnetic state of the acceptor center and (△) transition rate ν_{tr} from the paramagnetic to the diamagnetic state of the acceptor center.

Summary table of the C and q parameters for different acceptor centers (n is the impurity concentration)

	Si : Al	Si : Al	Si : P	Si : P	Si : P
n, cm^{-3}	2×10^{14}	2.4×10^{18}	3.2×10^{12}	2.3×10^{15}	4.5×10^{18}
$C \times 10^{-7}$, s^{-1}	0.2 ± 0.1	7.3 ± 1.7	0.27 ± 0.09	0.45 ± 0.16	22.0 ± 11.0
q	3.10 ± 0.2	2.1 ± 0.1	3.1 ± 0.1	2.9 ± 0.10	1.8 ± 0.2
ν (T = 4 K), s^{-1}	1.5×10^{8}	1.3×10^{9}	2.0×10^{8}	2.5×10^{8}	2.6×10^{9}

$A_{hf}/2\pi$ value is approximately 20 times smaller than the muon spin oscillation frequency derived earlier from the experiment carried out for a silicon sample with intrinsic conductivity in zero external magnetic field at 6 K [18]. The observation of zero-field muon spin oscillations is the most reliable and direct method of determining A_{hf}. Unfortunately, the results of work [18] have not been confirmed in further experiments. The reason for such a substantial discrepancy between our estimates of the hyperfine interaction constant and the results of [18] is yet to be clarified.

In our recent work [13], we have shown that the muon spin relaxation in silicon is governed by the spin–lattice relaxation of the acceptor center. The T^q-type ($1 \le q \le 9$) temperature dependence of the spin–lattice relaxation rate was observed by the EPR method in various materials (see, e.g., [19]). To our knowledge, there is only one theoretical work [20] in which the temperature dependence was calculated for the rate of spin–lattice relaxation of an acceptor center in a perfect silicon crystal. According to [20], the spin–lattice relaxation in the temperature range 10–100 K is dominated by the phonon Raman scattering and the relaxation rate varies with temperature as T^5.

The temperature dependence obtained in this work for the muon spin relaxation rate in silicon fits Eq. (2) if one assumes that the relaxation rate of the acceptor magnetic moment varies with temperature as

$$\nu(T) = CT^q. \quad (3)$$

The experimental data were processed with $j = 3/2$ and $A_{hf}/2\pi = 3 \times 10^7$ s^{-1}. The values of the C and q parameters obtained for different samples are given in the table. Note that, unlike the C parameter, q is virtually independent of A_{hf}. One can see in the table that the power-law exponent q varies from 2 to 3 for different samples. Therefore, the temperature dependences obtained in this work for the relaxation rates of acceptor magnetic moment markedly deviate from the T^5 law expected for a perfect crystal [20]. The cause for the discrepancy between the experimental results and theoretical predictions may be that the calculations [20] did not take into account the phonon lifetime, although it varies as $1/T^2$ or, in some cases, even more steeply below the Debye temperature [21]. The weakening of the temperature dependence (decrease in the q parameter) at impurity concentrations above ~10^{18} cm^{-3} may be caused by impurity-induced crystal deformations and the ensuing distortion of the phonon spectrum [22].

The last row in the table presents the acceptor relaxation rates ν at 4 K. Although these values do not contradict the EPR data for uniaxially compressed silicon samples [5–7], the EPR data on the magnetic relaxation rates of shallow acceptors in nondeformed silicon samples are lacking.

The acceptor ionization at $T \lesssim 30$ K (see Fig. 2) can be caused by electron capture from the conduction band or by the interaction with the nearest lying donor impurity resulting in the transition of both impurity centers from the neutral to the ionized state ($A^0D^0 \longrightarrow A^-D^+$) [23]. It follows from the EPR experiments [24] that n-type silicon becomes a degenerate semiconductor at an impurity concentration of ~3×10^{18} cm^{-3} (only a single line due to conduction band electrons is observed in the EPR spectrum). For degenerate n-type silicon, both ionization mechanisms can be regarded as the capture of a conduction band electron by an acceptor. Accordingly, the rate of electron capture by the neutral acceptor is determined as (see, e.g., [25]) $\nu_{tr} = \beta n_e$, where β is the capture coefficient and n_e is the concentration of free electrons. Taking $n_e = n_D = 4.5 \times 10^{18}$ cm^{-3} and using the values of ν_{tr} given in Fig. 2, one obtains approximately the 2×10^{-13} cm^3 s^{-1} and 7×10^{-14} cm^3 s^{-1} values for the $\beta(Al^0)$ coefficient in the temperature ranges $4.5 \le T \ge 10$ K and $12 \le T \le 30$ K, respectively. To our knowledge, there is only one work [26] where the $\beta(Al^0)$ value (determined by the photoexcitation method) was equal to 4×10^{-8} cm^3 s^{-1}. However, it is worth noting (see, e.g., [27]) that the experimental data on electron capture by neutral acceptors (B, In, or Ga) in silicon show a wide (up to 5 orders) scatter in the capture coefficient, while the β values obtained in [26] are in a systematic excess over the data measured by the other methods. Our estimate obtained for $\beta(Al^0)$ at T = 30 K lies between the $\beta(In^0) = 8 \times 10^{-15}$ cm^3 s^{-1} and $\beta(In^0) = 2 \times 10^{-12}$ cm^3 s^{-1} values determined by the photoconduction relaxation method in [25] and [28], respectively.

In summary, the experimental data obtained in this work and the analytic expressions [15] for the muon spin relaxation rate and precession frequency shift in the atom with $j = 3/2$ were used to estimate the hyperfine interaction constant for the interaction between the magnetic moments of muon and electron shell of a

muonic μAl atom and to determine the temperature dependence of the relaxation rate for the magnetic moment of a shallow acceptor center in a nondeformed silicon sample. Estimations are also carried out for the coefficient of electron capture by neutral aluminum and silicon atoms.

We are grateful to the Directorate of the Paul Scherrer Institut (Switzerland) for providing the possibility of performing the experiments. This work was supported in part by the Bundesministerium für Bildung und Forschung, contract nos. 03-MA5ST1 and 03-MA5ST2.

REFERENCES

1. G. D. Watkins, Fiz. Tverd. Tela (St. Petersburg) **41**, 826 (1999) [Phys. Solid State **41**, 746 (1999)].
2. A. Baldereschi and N. O. Lipari, Phys. Rev. B **8**, 2697 (1973).
3. I. A. Merkulov and A. V. Rodina, Fiz. Tekh. Poluprovodn. (St. Petersburg) **28**, 321 (1994) [Semiconductors **28**, 195 (1994)].
4. A. V. Malyshev, I. A. Merkulov, and A. V. Rodina, Fiz. Tekh. Poluprovodn. (St. Petersburg) **30**, 159 (1996) [Semiconductors **30**, 91 (1996)].
5. G. W. Ludwig and H. H. Woodbury, Bull. Am. Phys. Soc. **6**, 118 (1961).
6. G. Feher, J. C. Hensel, and E. A. Gere, Phys. Rev. Lett. **5**, 309 (1960).
7. B. G. Zhurkin, N. A. Penin, and N. N. Sibel'din, Fiz. Tekh. Poluprovodn. (Leningrad) **2**, 827 (1968) [Sov. Phys. Semicond. **2**, 688 (1968)].
8. H. Neubrand, Phys. Status Solidi B **86**, 269 (1978).
9. V. N. Gorelkin and V. P. Smilga, Zh. Éksp. Teor. Fiz. **66**, 1201 (1974) [Sov. Phys. JETP **39**, 586 (1974)].
10. V. N. Gorelkin, V. G. Grebinnik, K. I. Gritsaĭ, *et al.*, Yad. Fiz. **56** (10), 29 (1993) [Phys. At. Nucl. **56**, 1316 (1993)].
11. W. Beez, T. Grund, M. Hampele, *et al.*, in *PSI Annual Report F1*, Annex I (PSI, Villigen, Switzerland, 1994), p.125.
12. V. N. Gorelkin, V. G. Grebinnik, K. I. Gritsaĭ, *et al.*, Pis'ma Zh. Éksp. Teor. Fiz. **63**, 539 (1996) [JETP Lett. **63**, 566 (1996)].
13. T. N. Mamedov, V. N. Duginov, D. Herlach, *et al.*, Pis'ma Zh. Éksp. Teor. Fiz. **68**, 61 (1998) [JETP Lett. **68**, 64 (1998)].
14. G. L. Bir and G. E. Pikus, *Symmetry and Stain-Induced Effects in Semiconductors* (Nauka, Moscow, 1972; Wiley, New York, 1975).
15. V. N. Gorelkin and A. S. Baturin, in *Abstracts of the 8th International Conference on Muon Spin Rotation, Relaxation and Resonance, Les Diablerets, Switzerland, 1999*, p. II-10; Physica B (Amsterdam) (in press).
16. V. P. Smilga and Yu. M. Belousov, *Muon Method for Studying Materials* (Nauka, Moscow, 1991).
17. R. Scheuermann, J. Schmidl, A. Seeger, *et al.*, Hyperfine Interact. **106**, 295 (1997).
18. M. Koch, K. Majer, J. Major, *et al.*, Hyperfine Interact. **65**, 1039 (1990).
19. S. A. Al'tshuler and B. M. Kozyrev, *Electron Paramagnetic Resonance of Transition Element Compounds* (Nauka, Moscow, 1972).
20. Y. Yafet, J. Phys. Chem. Solids **26**, 647 (1965).
21. I. Ya. Pomeranchuk, *Collection of Scientific Works* (Nauka, Moscow, 1972), Vol. 1.
22. C. Kittel, *Introduction to Solid State Physics* (Wiley, New York, 1976; Nauka, Moscow, 1978).
23. R. C. Enck and A. Honig, Phys. Rev. **177**, 1182 (1969).
24. G. Feher, Phys. Rev. **114**, 1219 (1959).
25. Ya. E. Pokrovskiĭ and K. I. Svistunova, Fiz. Tverd. Tela (Leningrad) **7**, 1837 (1965) [Sov. Phys. Solid State **7**, 1478 (1965)].
26. M. Loewenstein and A. Honig, Phys. Rev. **144**, 781 (1966).
27. A. G. Milnes, *Deep Impurities in Semiconductors* (Wiley, New York, 1973; Mir, Moscow, 1977).
28. Ya. E. Pokrovskiĭ and K. I. Svistunova, Fiz. Tverd. Tela (Leningrad) **5**, 1880 (1963) [Sov. Phys. Solid State **5**, 1373 (1963)].

Translated by V. Sakun

JETP Letters, Vol. 71, No. 10, 2000, pp. 442–445. Translated from Pis'ma v Zhurnal Éksperimental'noĭ i Teoreticheskoĭ Fiziki, Vol. 71, No. 10, 2000, pp. 643–649.

CONDENSED MATTER

Critical Behavior of the Surface of $FeBO_3$ Single Crystals

A. S. Kamzin*, B. Stahl, E. Kankeleit***, R. Gellert***, M. Muller**, and D. B. Vcherashniĭ***

** Ioffe Physicotechnical Institute, Russian Academy of Sciences, Politekhnicheskaya ul. 26, St. Petersburg, 194021 Russia*

*** Materials Science Department, Technical University, 64287 Darmstadt, Germany*

**** Institute of Nuclear Physics, Technical University, 64287 Darmstadt, Germany*

Received April 20, 2000

The behavior of the surface and near-surface layers of macroscopic $FeBO_3$ single crystals is studied over the temperature range from 291 K to Neél temperature (T_N) using depth-selective conversion-electron Mössbauer spectroscopy. Three different phases or states, namely, an antiferromagnetically ordered phase (similar to the crystal bulk state), a surface phase, and a transition layer between them coexist near the Neél point in a surface layer ~500 nm thick. The critical parameters found for the bulk phase agree well with the theoretical critical index $\nu_{th} \cong 0.63$ predicted by the 3D Ising model. As the crystal surface is approached, the critical parameter β increases to 0.51(2) but remains smaller than the value of $\beta = 0.8$ for the surface of a semi-infinite Heisenberg model. Therefore, the effective dimensionality of the system, being equal to 3 in the bulk, decreases at the crystal surface. © *2000 MAIK "Nauka/Interperiodica".*

PACS numbers: 75.30.Kz; 75.40.-s; 68.35.Rh

Critical behavior of surfaces has attracted considerable attention of researchers since the 1970s [1, 2]. A great many theoretical works on this problem have been published to date (see references in [3–7]). The first experimental studies of the surface properties were carried out for thin powders and films [8–10], because the methods for gaining information about the surface states of macroscopic crystals and its direct comparison with the bulk data were lacking. Although the interpretation of experimental data is a challenge, the investigations of thin powders and films were helpful in elucidating some surface properties. A unique interpretation of surface phenomena calls for studies of the surfaces of macroscopic crystals by the experimental methods which can be used not only for measuring the magnetic characteristics but also for a layer-by-layer analysis of a near-surface layer at depths from 1 to 100 nm with an appropriate depth resolution.

Of fundamental interest is the behavior of a thin surface layer in the region of bulk critical temperature, as well as a change in the critical parameters upon approaching the surface. The first Mössbauer studies of macroscopic samples [10–12] revealed distinctions in the bulk and surface behaviors near the critical point. The relaxation effects absent in the bulk but occurring in the surface layers of $FeBO_3$ macrocrystals near the Neél temperature were observed in [11]. It was shown in [10, 12] that the magnetic ordering temperature in a thin surface layer is lower than in the bulk of the sample. It was also found that the Neél temperature in $FeBO_3$ crystals gradually decreases within a surface layer of thickness 300 nm [12].

The use of a method allowing the surface layer to be analyzed with an accuracy of a few nanometers enabled the authors of [13] to observe the lowering of the effective magnetic field (or magnetization) as the surface of an $FeBO_3$ crystal was approached at 2.4(9) nm. Though consistent with the data in [9, 14], this result was not observed in [10–12], probably because of a low depth resolution (no higher than ~200 nm) in works [10–12].

Thus, an analysis of the available experimental data indicates that these data are not nearly numerous enough for them to be compared with the theoretical predictions.

In this work, the critical behavior of a surface layer is experimentally studied for a bulky $FeBO_3$ crystal in the region of phase transition to a disordered state at the Neél temperature (T_N). Measurements were carried out using depth-selective conversion-electron Mössbauer spectroscopy (DSCEMS). In the past decade, the DSCEMS method was intensively elaborated, and now it can be used for analysis of the nanometer scale-thick layers [15]. We used computer simulation to refine the magnetostatic electronic analyzer in a DSCEM spectrometer, with the aim of enhancing luminosity and improving the accuracy of electron energy resolution [16]. The use of a refined DSCEM spectrometer in studying the surface properties of various macroscopic crystals [13, 17] made it possible to obtain new data which are consistent with the theoretical predictions.

Mössbauer studies of critical behavior present difficulties because the effective magnetic fields are low, so that the Zeeman levels are not resolved in the spectrum. This sizably impairs the accuracy of determination of

the critical parameters. However, if the iron ions occupy equivalent positions in a crystal, an analysis of the spectra is greatly simplified in the region of critical temperature. Because of this, the studies were carried out with one of the simplest rhombohedral $FeBO_3$ crystals belonging to the orthorhombic system [18]. The magnetic structure of $FeBO_3$ is formed from two sublattices of iron ions occupying two equivalent octahedral positions antiferromagnetically coupled at temperatures below the bulk T_N = 348.3 K. Crystal symmetry (space group D^6_{3D}) allows for a weak ferromagnetic moment in the basal plane perpendicular to the threefold axis *C*, as was confirmed in [18, 19]. The bulk critical behavior of $FeBO_3$ crystals is well known [18–21].

$FeBO_3$ crystals were synthesized by spontaneous crystallization from a melt containing iron oxide 96% enriched with the ^{57}Fe isotope. Plates ~7 mm in diameter and ~150-μm thick were chosen for Mössbauer measurements. The plate planes coincided with the basal (111) plane. The sample surfaces were processed in two steps: (1) by mechanical polishing with fine polishing powders and light etchants and (2) by chemical polishing for ~50 h at room temperature in a 1 : 1 mixture of H_3PO_4 and H_2SO_4 acids. It should be emphasized that the experimental results were reproduced only for the chemically polished samples. As a result, the magnetic structure of surface layers as thin as 2 nm did not differ from the structure of crystal bulk, as was justified by the DSCEMS measurements of isomer shifts and quadrupole splittings in the range of paramagnetic temperatures. The Mössbauer spectra recorded with a DSCEM spectrometer for different electron energies in the range of the ^{57}Fe *K*-conversion line are shown in Fig. 1. It is seen from the electron-yield functions at the bottom of Fig. 1 that electrons with energies 7.25 keV mainly escape from the 20-nm layer, whereas electrons with energy 6.5 keV escape from the layer ~120 nm thick. The experimental spectra were normalized, and their residuals are shown at the right of Fig. 1.

One can see from Fig. 1 that at temperatures below T_N the spectra consist of a single well-resolved Zeeman sextet. The ratio 3 : 4 : 1 observed at 300 K for the pairs of its components suggests that the crystals were properly oriented. Below ~341 K, the spectra are virtually identical for both electron energies. At 341.25 K, the lines of the 7.25 keV spectrum are appreciably broadened. On a further rise in temperature, a line similar to the paramagnetic line appears on the background of the Zeeman sextet in the spectrum of electrons with energy 7.25 keV. The intensity of this line increases with temperature, while the lines of the sextet come close together and become less intense. Thus, the lines corresponding to the magnetically ordered and paramagnetic states coexist in the spectra of electrons with energy 7.25 keV in the T_N region.

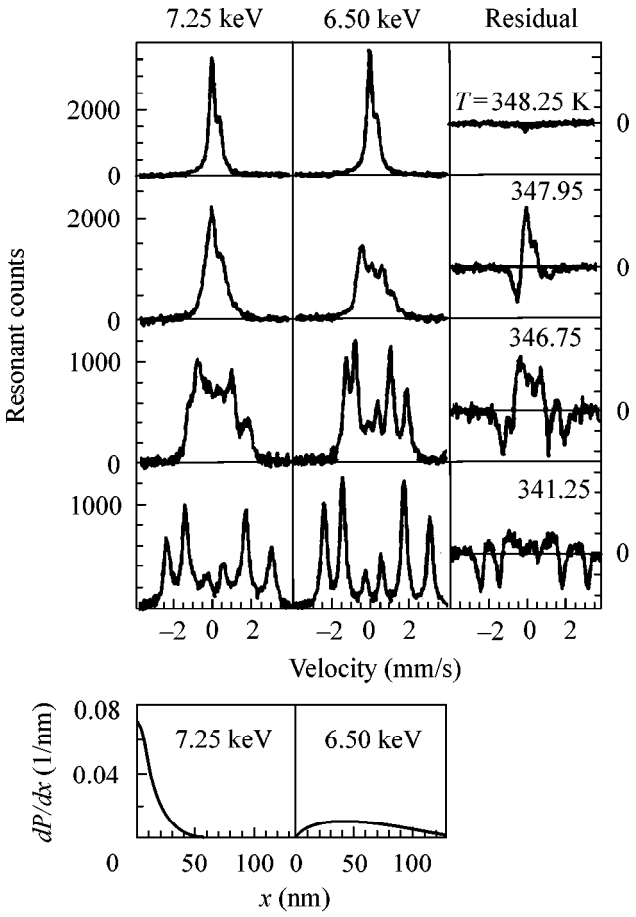

Fig. 1. Mössbauer spectra recorded using the DSCEMS method by detecting ^{57}Fe *K*-conversion electrons of two energies. The electron-yield functions are presented at the bottom. The residuals of the spectra are shown at the right.

The spectra of electrons with energy 6.8 keV suffer the following transformations upon passing through the Neél point of $FeBO_3$. The separation between the components of the Zeeman sextet gradually deceases, whereupon the sextet collapses into a paramagnetic doublet. This transformation is clearly seen in Fig. 1. At 348.25 K, i.e., only 0.1 K below T_N, the Mössbauer spectra look virtually identical for the electrons of both energies (Fig. 1). This strongly suggests that the thickness of a magnetically distinctive surface layer increased to ~200 nm. The exact thickness of this layer can be determined upon detection of the ^{57}Fe *L* electrons, which allow an analysis of surface layers as thick as 600 nm [15].

An analysis of the Mössbauer spectra for different electron energies and different temperatures showed that they can be described adequately only upon decomposition into three components or phases: *C*I, *C*II, and *C*III. The magnetic characteristics of the *C*I state are similar to those of the $FeBO_3$ bulk and agree well with the data in [12, 18–21]. The *C*II phase is sim-

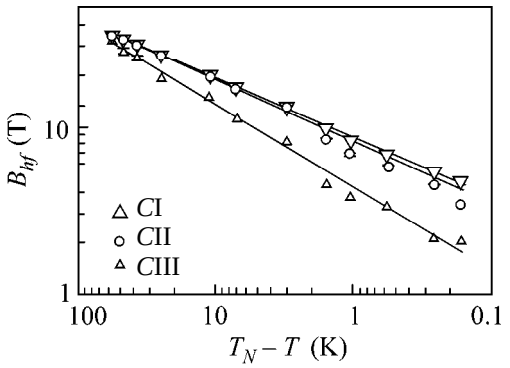

Fig. 2. Log–log plots of the effective magnetic field (B_{hf}) vs. $t = T_N - T$ for the *C*I, *C*II, and *C*III states.

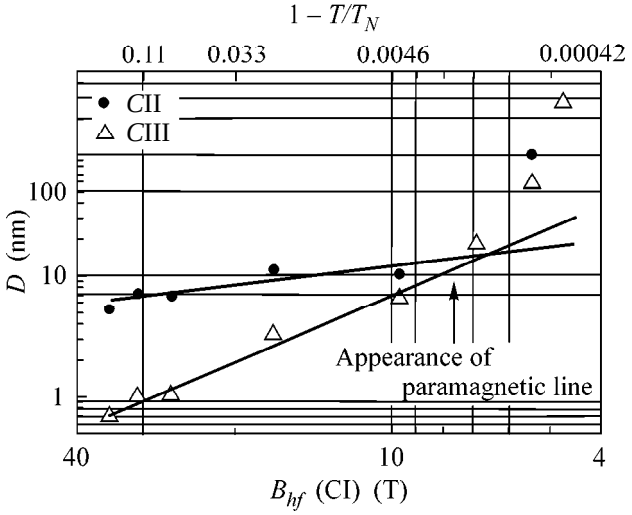

Fig. 3. Temperature-dependent layer thicknesses *D*II and *D*III for the *C*II and *C*III states, respectively. The solid lines correspond to the calculations by Eq. (2). The errors of determination are within the symbols.

ilar to *C*I, but is characterized by a slight lowering and scatter of the effective magnetic field (B_{hf}). The degree of lowering and scatter of B_{hf} is considerable for the *C*III component (at 300 K, the field decreases by 15%). The validity of such a decomposition into three phases was confirmed by the results of decomposition of the DSCEMS data according to the depth of the layer analyzed. The matter is that the other possible ways of decomposition (within the statistical experimental error) bring about results incompatible with the theory of electron transport.

The log–log plots of the temperature-dependent effective magnetic fields (B_{hf}) calculated for these three states are shown in Fig. 2. It is seen from Fig. 2 that the effective fields at the nuclei of iron ions located in a layer situated closer to the crystal surface (the *C*III phase) decrease with increasing temperature faster than the fields at the iron nuclei situated farther below the surface (the *C*I phase). To check the reproducibility of the results obtained for a given temperature, the spectra were recorded repeatedly and with different sequences of temperature. An analysis of these data showed that the results are reproducible. The critical indices for the *C*I and *C*II states coincide, within the statistical error, at temperatures below 346 K, while the distinctions at $T >$ 346 K may be explained by the statistical correlation arising in the course of mathematical processing of the spectra. The critical index $\beta_1 = 0.348(4)$ obtained from the relationship

$$B_{hf}(T) = B_{hf}(0)(1 - T/T_N)^{\beta}, \qquad (1)$$

is in compliance with the data in [18–21]. The use of Eq. (1) for calculating the critical index of the *C*II state gave $\beta_2 = 0.353(7)$, whereas the corresponding value for the *C*III state was found to be $\beta_2 = 0.51(2)$. One can see from Fig. 2 that the experimental data agree well with the results of extrapolating by Eq. (1) (shown in Fig. 2 by solid lines).

As mentioned above, the volume (or thickness) of the *C*III phase increases in the region of the Neél point. To determine the temperature dependences for the thicknesses *D*II and *D*III of the *C*II and *C*III phases, respectively, the Mössbauer spectra were analyzed. The resulting data for *D*II and *D*III are presented in Fig. 3 as functions of effective magnetic field (B_{hf}) in the *C*I state closest to the crystal bulk. For $B_{hf} \geq 10$ T, i.e., $t \geq 2$ K, the *D*II and *D*III values obey the power law

$$D(B_{hf}) = D_0 B_{hf}^{-\nu/\beta 1}, \qquad (2)$$

as follows from the coincidence of the experimental points with the solid lines displaying this power law in Fig. 3. Using the relationship $\nu_3/\beta_1 = 1.7(1)$ for *D*III and the value of $\beta_1 = 0.348(4)$ determined above for the critical index, one gets $\nu_3 = 0.59(4)$. The temperature dependence of *D*II is weaker and gives a value of 0.5(1) for the ν_2/β_1 ratio. At temperatures above 346.5 K, the thicknesses of the *D*II and *D*III phases increase much faster, in contradiction to the results obtained by the extrapolation of Eq. (2), shown in Fig. 3 by solid lines. It is conceivable that, starting at this temperature, the pattern of transition of the system to the paramagnetic state becomes more complicated. This is also confirmed by the appearance of a paramagnetic *C*III component in the Mössbauer spectra and an increase in its intensity with temperature starting at 346.5 K.

Thus, the behavior of the surface and near-surface layers of macroscopic $FeBO_3$ single crystals was studied in the region of bulk critical temperatures. It is shown experimentally that three different states occur within the surface layer of thickness ~500 nm near the Neél temperature: the antiferromagnetically ordered phase (similar to the crystal bulk state) lying deep below the surface, the surface phase, and the transition layer between them. The characteristic ν_3 value for the thickness of the surface phase at $t \geq 2$ K agrees well

with the theoretical critical index $\nu_{th} \cong 0.63$ obtained for the correlation length ξ_{bulk} in the 3D Ising model [22]. The surface correlation length $\xi_{surface}$ of a semi-infinite system should be the same [3, 6]. In the $t = 0.65$ region, the critical fluctuations become comparable with the Larmor precession of the Mössbauer nucleus (10^{-8} s) as $t \longrightarrow 0$ K, manifesting themselves by the paramagnetic contribution to the spectra in this temperature range. Consequently, the appearance of the superparamagnetic-type spectra near the Neél point is explained by the spin-wave excitation at lower temperatures and the critical fluctuations in the vicinity of T_N. One can conclude from the intensity ratio of the Mössbauer lines that the magnetic moments relax in the basal plane, i.e., perpendicularly to the *C*-axis.

The critical index $\beta_3 = 0.51(2)$ lies between the bulk value and the value corresponding to the surface of a semi-infinite Heisenberg model, for which $\beta = 0.8$ [7, 22]. The ν_3 and ν_{th} values coincide because an increase in the *D* and ξ parameters with temperature competes with the magnetocrystalline anisotropy. The effective dimensionality of the system likely equals 3. A steeper increase in *D* at $t < 1$ K is indicative of a lower dimensionality.

The Russian authors are grateful to the PROMT company (http://www.promt.ru) for providing them with software. The German authors thank the German Science Foundation for support in the design of the DSCEM spectrometer. This work was supported by the Russian Foundation for Basic Research, project no. 98-02-18279.

REFERENCES

1. M. I. Kaganov and A. M. Omel'yanchuk, Zh. Éksp. Teor. Fiz. **61**, 1679 (1971) [Sov. Phys. JETP **34**, 895 (1972)].
2. D. L. Mills, Phys. Rev. B **3**, 3887 (1971).
3. K. Binder, in *Phase Transitions and Critical Phenomena*, Ed. by C. Domb and J. L. Lebowitz (Academic, New York, 1983), Vol. 8.
4. T. Kaneyoshi, J. Phys. C **3**, 4497 (1991).
5. A. J. Freeman and Ru-qian Wu, J. Magn. Magn. Mater. **100**, 497 (1991).
6. H. Dosch, *Critical Phenomena at Surfaces and Interfaces: Evanescent X-ray and Neutron Scattering* (Springer-Verlag, 1992, Springer Tracts Mod. Phys., 1992), vol. 126.
7. H. W. Diehl, Int. J. Mod. Phys. B **11**, 3503 (1997); H. W. Diehl and S. Dietrich, Z. Phys. B **42**, 65 (1981); Z. Phys. B **43**, 315 (1981).
8. *Studies of Magnetic Properties of Fine Particles and Their Relevance to Materials Science*, Ed. by J. L. Dormann and D. Fiorani (Elsevier, Amsterdam, 1992).
9. T. Shinjo, Surf. Sci. Rep. **12** (2), 49 (1991).
10. R. D. M. Grath, M. R. Mirzababaev, and J. C. Walker, Phys. Lett. A **67**, 149 (1978).
11. P. P. Kovalenko, V. G. Labushkin, É. R. Sarkisov, and I. G. Tolpekin, Fiz. Tverd. Tela (Leningrad) **29**, 593 (1987) [Sov. Phys. Solid State **29**, 340 (1987)].
12. A. S. Kamzin and L. A. Grigor'ev, Fiz. Tverd. Tela (St. Petersburg) **36**, 1271 (1994) [Phys. Solid State **36**, 694 (1994)].
13. B. Stahl, R. Gellert, M.Muller, *et al.*, Hyperfine Interact. (2000) (in press); A. S. Kamzin, B. Stahl, R. Gellert, *et al.*, Pis'ma Zh. Éksp. Teor. Fiz. **71**, 197 (2000) [JETP Lett. **71**, 134 (2000)].
14. T. Yang, A. Krishnan, N. Benczer-Koller, and G. Bayreuther, Phys. Rev. Lett. **48**, 1292 (1982).
15. G. N. Belozersky, *Mössbauer Studies of Surface Layers* (Elsevier, Amsterdam, 1993); K. Nomura, Y. Ujihira, and A. Vertes, J. Radioanal. Nucl. Chem. **202**, 103 (1996).
16. B. Stahl and E. Kankeleit, Nucl. Instrum. Methods Phys. Res. B **122**, 149 (1997).
17. B. Stahl, R. Gellert, A. Kamzin, *et al.*, J. Phys. IV **7**, C1-219 (1997); A. S. Kamzin, B. Stahl, R. Gellert, *et al.*, Fiz. Tverd. Tela (St. Petersburg) **42** (2000) (in press) [Phys. Solid State **42**, 897 (2000)].
18. M. Eibschutz and M. E. Lines, Phys. Rev. B **7**, 4907 (1973).
19. D. M. Wilson and S. Broersma, Phys. Rev. B **14**, 1977 (1976).
20. A. L. Irshinskiĭ, V. P. Ozhogin, V. M. Cherepanov, and S. S. Yakimov, Zh. Éksp. Teor. Fiz. **76**, 1111 (1979) [Sov. Phys. JETP **49**, 563 (1979)].
21. Landold-Bernstein, New Series **III**/**12b**, 44 (1980).
22. J. Zinn-Justin, *Quantum Field Theory and Crytical Phenomena* (Clarendon, Oxford, 1996).

Translated by V. Sakun